SCUOLA DI SCIENZE

Dipartimento di Fisica e Astronomia

Corso di Laurea Magistrale in Astrofisica e Cosmologia

The Solar System dynamical interaction with the Galaxy environment: evolutionary implications for alien Oort clouds and exo-planets

Tesi di Laurea

Presentata da:

Alina Marchetto

Relatore:

Chiar.mo Prof. Alberto Buzzoni

A Saverio,
ai miei nonni.

Abstract

The Sun is located in the Orion Arm of the Milky Way galaxy and its surrounded, along other bodies, by stars. This thesis work aims at understand whether these stars can dynamically interact with the Sun and its Solar System and to investigate the possible features of this kind of interactions. We will begin from an observable quantity, the Oort surface density for stars that we will assume $\Sigma_* = 38\,\mathrm{M}_\odot \mathrm{pc}^{-2}$ (Kubryk, Prantzos, and Athanassoula 2015), and we will build a stellar density profile for the Milky Way galaxy using the model suggested by Jurić et al. 2008. Then, making use of the Initial Mass Function and the Star Formation Rate function, we will calculate the Present Day Mass Function to have the correct distribution of mass along stellar classes. From kinematic concepts such as the rotation curve, the Oort constants and the Local Standard of Rest we will characterize the motion of the Sun in the Galaxy, assuming for our calculations a value $v = 14$ km s^{-1} for the Sun velocity with respect to the Local Standard of Rest. We will then define the Hill radius and Sphere Of Influence radius by making use of the restricted three body theorem. We will thus have a complete model in terms of star density and distribution, kinematics, and dynamics which will lead us to quantify different mass ranges which will show the possibility of a close SNII explosion, and will highlight the perturbing effect of near low mass stars onto the Solar System Oort cloud and the action of the Sun onto alien Oort clouds. Lastly, in this thesis we will compare our models to the latest Gaia EDR3 data from the paper of Reylé, C. et al. 2021 which will allow us to analyze the current situation in the Solar neighbourhood and will highlight the presence of stars currently perturbing the Oort cloud and five possible Solar System Oort cloud-alien Oort cloud merging.

Sommario

Il Sole è posizionato in corrispondenza del Braccio di Orione all'interno della Via Lattea ed è circondato da stelle e da altri oggetti. Lo scopo di questa tesi è di capire se queste stelle possono interagire dinamicamente con il Sole ed il suo Sistema Solare e, in tal caso, di esaminare gli effetti di questo tipo di interazioni. Cominceremo la nostra trattazione da un osservabile, la densità superficiale di Oort per le stelle che assumeremo pari a $\Sigma_* = 38\,\mathrm{M_\odot pc^{-2}}$ (Kubryk, Prantzos, and Athanassoula 2015), e costruiremo un profilo di densità stellare per la Via Lattea utilizzando il modello suggerito da Jurić et al. 2008. Facendo quindi uso dei concetti di Initial Mass Function e di funzioni di Star Formation Rate potremo calcolare la Present Day Mass Function in modo da distribuire correttamente la massa a seconda della classe stellare. Dal nozioni di cinematica quali la curva di rotazione, le costanti di Oort e il Sistema di Riposo Locale potremo caratterizzare il movimento del Sole all'interno della Galassia e assumeremo il valore $v = 14\,\mathrm{km\,s^{-1}}$ per la velocità del Sole rispetto al Sistema di Riposo Locale. Definiremo, quindi, il raggio di Hill e il raggio della Sfera di Influenza attraverso il problema dei tre corpi ridotto. A questo punto avremo un modello completo in termini di densità e distribuzione stellare, cinematica e dinaimca che ci porterà a definire intervalli in massa in cui si potrenno verificare esplosioni di SNII e che ci permetterà di sottolineare l'effetto perturbativo delle stelle di piccola massa poste nelle vicinanze sulla nube di Oort del Sistema Solare e l'effetto che produce Sistema Solare sulle nubi di Oort aliene. Infine in questa tesi confronteremo i nostri modelli con i dati aggiornati della EDR3 di Gaia dal paper di Reylé, C. et al. 2021 che ci permetteranno di osservare l'attuale situazione nei dintorni Solari e metteranno in luce la presenza di stelle che stanno perturbando la nube di Oort e di cinque possibili merging tra la nube di Oort del Sistema Solare e nubi di Oort aliene.

Contents

Chapter 1

Introduction: aim of the project

The current vision of the Sun inside the Milky Way Galaxy places it in an almost planar position 8.2 kpc far from the Galaxy centre (McMillan 2016). The Sun belongs to the thin disk which is one of the components of the Galaxy structure. We can say that the thin disk is one of the densest zones in terms of stellar distribution, along with bulge and spiral arms, of the Galaxy, this feature could possibly cause interactions between the Sun and other stars that could have as consequences on the Solar System comet showers or object stripping. Recent work on this topic were made by Bailer-Jones 2018 and Bailer-Jones et al. 2018 in which the author used Gaia DR2 data to estimate close encounters from radial velocities of near stars.

This thesis work aims to take a step further and evaluate the consequences of close encounters and in general the effect of the presence of near stars by studying how they would dynamically interact with the Solar System.

Since we will have a theoretical approach to the problem, in Chapter 2 we will model the local Galaxy structure starting from the Oort density given by Kubryk, Prantzos, and Athanassoula 2015 and we will assume a Galaxy density profile from Jurić et al. 2008. We will also want to establish how the mass is distributed between the different star classes thus we will calculate the Present Day Mass Function by assuming functional forms both for the Initial Mass Function and the Star Formation Rate. We will choose three Initial Mass Function models from Salpeter 1955, Miller and Scalo 1979, and Chabrier 2003 and four Star Formation Rate models from Schmidt 1959 and Buzzoni 2005. The Present Day Mass Function will be computed then in Chapter 3 by making use of the stellar lifetime law given by Buzzoni 2002.

In Chapter 4 we will then compare our results with up to date Gaia EDR3 data from Reylé, C. et al. 2021 and then in Chapter 5 we will check our Galaxy radial density model by computing

the rotation curve and calculate the Sun rotational velocity to be compared with the one given by the Oort constants calculation of Bobylev and Bajkova 2020. Finally, we will make use of the LSR definition to assume a mean stellar velocity to apply to all the stars in our model. We will mean the LSR value between the values given by the works of Dehnen and Binney 1998, Aumer and Binney 2009, Schönrich, Binney, and Dehnen 2010, Golubov et al. 2013, Bobylev and Bajkova 2018, and Ding, Zhu, and Liu 2019.

In Chapter 6 our last step will be to formalize the restricted three body problem and to give the definitions and values for the Hill sphere and SOI sphere and some observations upon the limits of the Solar System.

The results we will present in Chapter 7 will show that the possibility of a comet shower or object stripping is bounded to the mass of the interacting star and its relative distance to the Sun, and we will highlight some other aspects such the probability for the Solar System to be hit by high energy radiation from SNII and the possibility of a sort of merging zone in the outer Oort cloud with alien Oort clouds of stars of low mass. We will thus investigate and show that a perturbation of the planet orbits is possible and will show the frequency of this feature for the Solar System. Finally we will compare our results with near stars included in the catalogue of Reylé, C. et al. 2021.

Chapter 8 will summarize the work discussing also how all the previous results would change if the Sun would enter a denser environment such as the spiral arms of the Galaxy and giving some possible future use of this work.

Chapter 2

Milky Way Structure

2.1 Introduction

In this Chapter we will describe the Milky Way, MW, structure in terms of star density and star density profiles. Since this thesis purpose is to study the interactions between stars in the Solar neighbourhood it is fundamental to know how the stars are positioned with respect to the Sun in order to have results as realistic as possible. Firstly, in Section 2.2 we will give an historical introduction on the studies of MW structure starting from the 1920 Great Debate and subsequently we will introduce and comment useful quantities that will be used in our calculations.

In Section 2.3 we will discuss about the Oort surface density comparing the results of different authors and making a choice on the Oort density value ($\Sigma_* = 38\,\mathrm{M_\odot pc^{-2}}$) we will use for subsequent calculations.

In Section 2.4 we will choose and compute the density profile for the MW from the work of Jurić et al. 2008. This profile density, along with the Oort density, will be used to get a representative mean density for the Sun surroundings which will then be employed in Chapter 3 to normalize the calculated Present Day Mass Function to realistic values.

In Section 2.5 after a brief historical introduction we will show the three Initial Mass Functions adopted which will be utilized in the Present Day Mass Function calculation.

Finally, in Section 2.6 we will introduce four possible Star Formation Rates that will be used in combination with the Initial Mass Functions to calculate the Present Day Mass Function.

2.2 Setting the context

The Milky Way galaxy has been a matter of interest for a very long time. During human history, our Galaxy has been described variously: from the whole Universe to a small part of it and from considering it at the centre of the Universe to understand that there is no privileged spot.

In recent times, a big step forward in the characterization of our Galaxy has been the 1920 Great Debate where Harlow Shapley and Herbert Curtis presented their studies and summed up the recent-to date astronomical discoveries. The debate goal was to characterize the Galaxy's environment. For astronomers back then, outer galaxies didn't exist but spiral nebulae or island universes were observed. Shapley claimed that spiral nebulae should be inside the Galaxy which had a dimension of about *100* kpc with the Sun placing about *20* kpc far from the centre. Curtis' idea was instead that the nebulae should be out of our Galaxy. Furthermore, Curtis believed that the Sun's location was in the Galaxy's centre and that the Milky way would have dimensions of about *10* kpc. Both astronomers were right for some aspects: now, we know that the Sun isn't at the centre of the Milky Way (least of all at the centre of the Universe) and that spiral nebulae are outer galaxies.

Later on, new theories and observations allowed researchers to make progress in the definition of the Galactic environment. Oort 1927a confirmed Lindblad's theory Lindblad 1926 of the rotation of the Galaxy around its centre and in his 1958 paper Oort, Kerr, and Westerhout 1958 gives a detailed view of the Milky Way, more similar to the actual one, with new details as the observations of hydrogen gas clouds and a defined spiral structure. Subsequently, new theories went on such as the density wave theory Lin and Shu 1964, the hypothesis of a black hole at the centre of the galaxy, the dark matter halo and a partition in substructures basing on dynamics and chemical features.

Today, the topic is still open as (Hou 2021) emphasizes showing in great detail the various substructures of the Local arm, and questioning the previous theories about the formation and the working mechanism of spiral arms such as the density wave theory. In Figure 2.1 is shown a representation of the Galaxy as would be seen from the top.

For this work we'll use some of the most recent studies of the Milky Way. The actual shared view of the Galaxy structure is of different components (e.g. as in Robin et al. 2003) such as the dark matter halo, the halo, the bulge, the bar, and the disk which is split itself into two subcomponents: thin and thick disk. All these parts are an object of study to determine the Galaxy's structure, dimensions, mass, kinematics, and composition and to obtain information about how the galaxy works and its formation history. One of the recent studies for the Milky Way structure is of McMillan 2016 that estimates various parameters as the MW total stellar mass and Sun's distance

from the Galactic centre:

$$M_{gal} = 54.3 \cdot 10^9 \, \mathrm{M_\odot} \quad ; \tag{2.1}$$

$$R_\odot = 8.20 \pm 0.09 \, \mathrm{kpc} \quad . \tag{2.2}$$

For this thesis work we want to model the Milky Way in the Solar neighbourhood using for our model thick and thin disk components and halo component. Since we want to model the density profile especially in the Solar neighbourhood we will not add the bulge component as for (2.2) the Sun is far enough from the centre of the Galaxy.

In the section 2.3 we'll describe the observed stellar surface density that will be used to normalize our models; in the section 2.4 we'll calculate the stellar density vertical profile for the Solar neighbourhood; in the section 2.5 we'll discuss the IMFs used and in the section 2.6 we'll show the star formation rates adopted.

2.3   Oort density

The Oort density is a local parameter for the surface density of stars in the Solar neighbourhood, it's calculated as the density of stars (in solar masses, $\mathrm{M_\odot}$) by area unit (in $\mathrm{pc^2}$) and the density of remnants, gas or dark matter can also be included, depending on the work.

Oort first calculated this parameter in his study of 1932 (Oort 1932). He observed the motion of the stars and resolved the Poisson equation for the gravitational potential:

$$\frac{\partial}{\partial z}\left(\frac{1}{\nu(z)} \frac{\partial(\nu(z) <\sigma_z>^2)}{\partial z} \right) = -4\pi G \rho \quad , \tag{2.3}$$

this equation is the equivalent of the classic Poisson equation but described with observable variables. In (2.3), $\nu(z)$ is the vertical velocity distribution, σ_z is the vertical velocity dispersion and ρ is the star density, using this equation Oort calculated the volumetric density, $\rho_* = 0.15$ $\mathrm{M_\odot pc^{-3}}$. Bahcall 1984 continued Oort's studies and adapted to more recent data. He solved the equation (2.3) to describe realistically the gravitational potential. Bahcall used several models to fit Oort data and found a surface density that ranges from $\Sigma_* = 49 \, \mathrm{M_\odot pc^{-2}}$ to $\Sigma_* = 120$ $\mathrm{M_\odot pc^{-2}}$. More recently, McMillan 2011 shows a method to fit mass models to observables. He decomposes the Milky Way into subcomponents and uses values from literature to create the best fit model that gives $\Sigma_* = 63.9(60.3) \, \mathrm{M_\odot pc^{-2}}$ for best fit(convenient). In the work of Bovy and Rix 2013, the authors use SDSS/SEGUE[1] data to calculate the distribution of mass, the rotation

---

1. Sloan Digital Sky Survey/Sloan Extension for Galactic Understanding and Exploration.
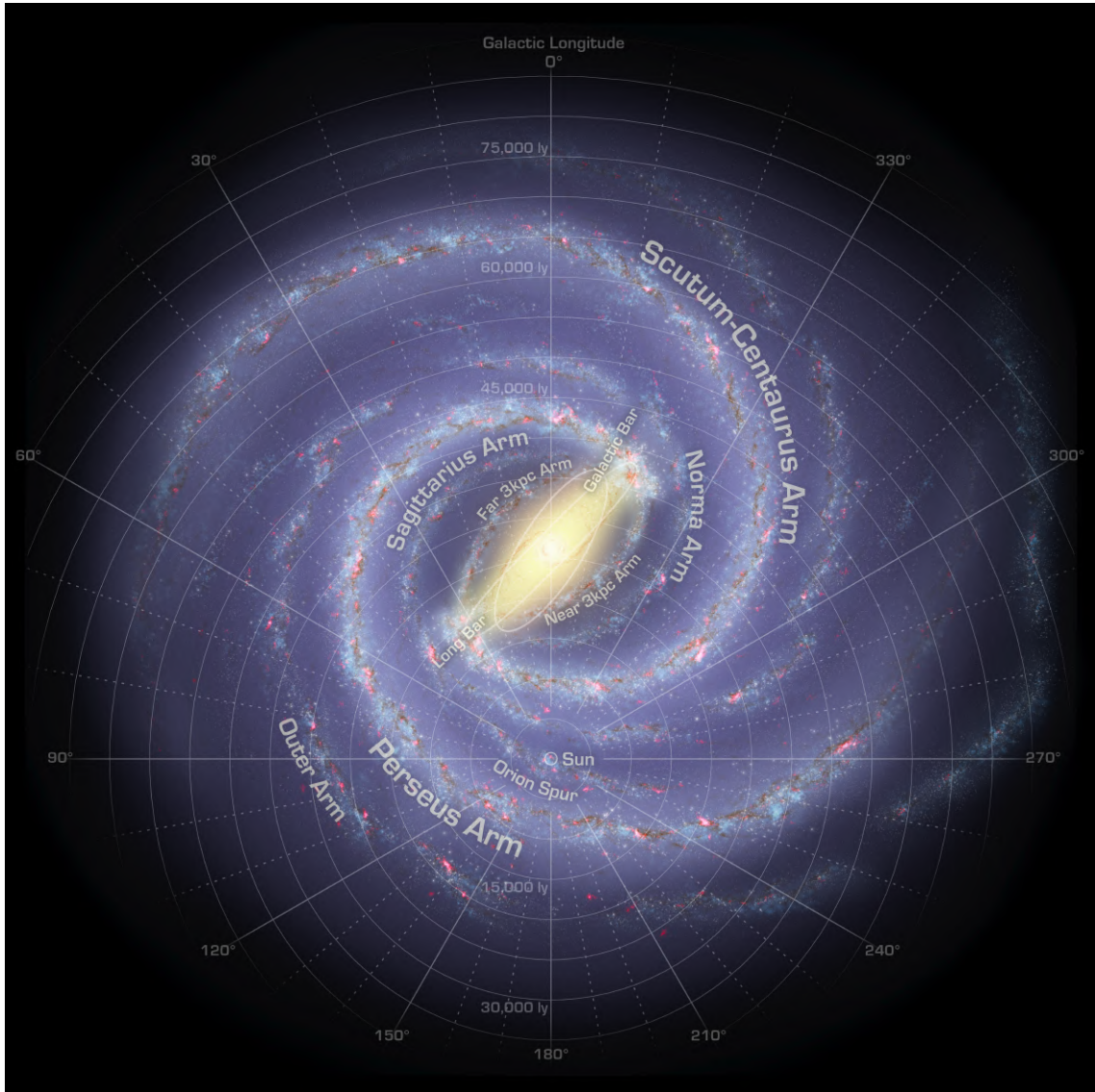
Figure 2.1: Artistic representation of the top view of the Milky way based on the last studies of the Galaxy structure. Superposed to the picture the is the galactic longitude grid that helps to understand the Sun's position in the galaxy disk. Credits: NASA/Adler/U.Chicago/Wesleyan/JPL-Caltech.

curve, and parameters of the Galaxy using data and analytic models. They find a stellar and remnants surface density of $\Sigma_* = 38 \pm 4 \, \mathrm{M_\odot pc^{-2}}$. Kubryk, Prantzos, and Athanassoula 2015 in their paper model the Galaxy adding radial migration and obtain a stellar and remnant surface density of $\Sigma_* = 38 \, \mathrm{M_\odot pc^{-2}}$. Finally the last paper we considered is McKee, Parravano, and Hollenbach 2015 where the authors fitted their model basing upon previous work of Flynn et al. 2006 and found $\Sigma_* = 31.2 \, \mathrm{M_\odot pc^{-2}}$ in the z-range that goes from $z_{min} = -1100$ pc to $z_{max} = 1100$ pc. For this work the Oort density has been taken from the work of Kubryk, Prantzos, and Athanassoula 2015 as:

$$\Sigma_* = 38 \, \mathrm{M_\odot pc^{-2}}. \tag{2.4}$$

The surface density still hasn't a fixed value, it can easily change for different data or model used for the calculations, so we choose to use this as a free parameter in our forthcoming discussion. In Table 2.1 the surface densities discussed are shown.

Author(s)	$\Sigma_* \, [\mathrm{M_\odot pc^{-2}}]$
Bahcall 1984	49-120
Flynn et al. 2006	35.5
McMillan 2011	63.9(60.3)
Bovy and Rix 2013	38±4
Kubryk, Prantzos, and Athanassoula 2015	38
McKee, Parravano, and Hollenbach 2015	31.2
McKee, Parravano, and Hollenbach 2015	33.4

Table 2.1: Summary of the surface densities taken in account.

2.4 Disk structure

As mentioned before, Milky Way's disk can be decomposed into two substructures: thick disk and thin disk. These structures are different either by dimensions and composition. An example of the different structures of the Galaxy can be see in Figure 2.2. There have been many studies of the Galactic structure in the Solar neighbourhood within the years. Sandage 1987 derived a density distribution perpendicular to the galactic plane for the stars and compared them to the known data from other authors. Sandage found that a good fit of the data is with two power laws representing the thin and thick disk and another one representing the halo. The latter can be well represented using a power law as $\rho(r) \sim (1 + r)^{-n}$ but the author finds that an exponential form for the vertical distribution of the halo is a good approximation for the Solar neighbourhood. Sandage also found that the thick-to-thin disk normalization should be $\sim 11\%$ and the halo-to-
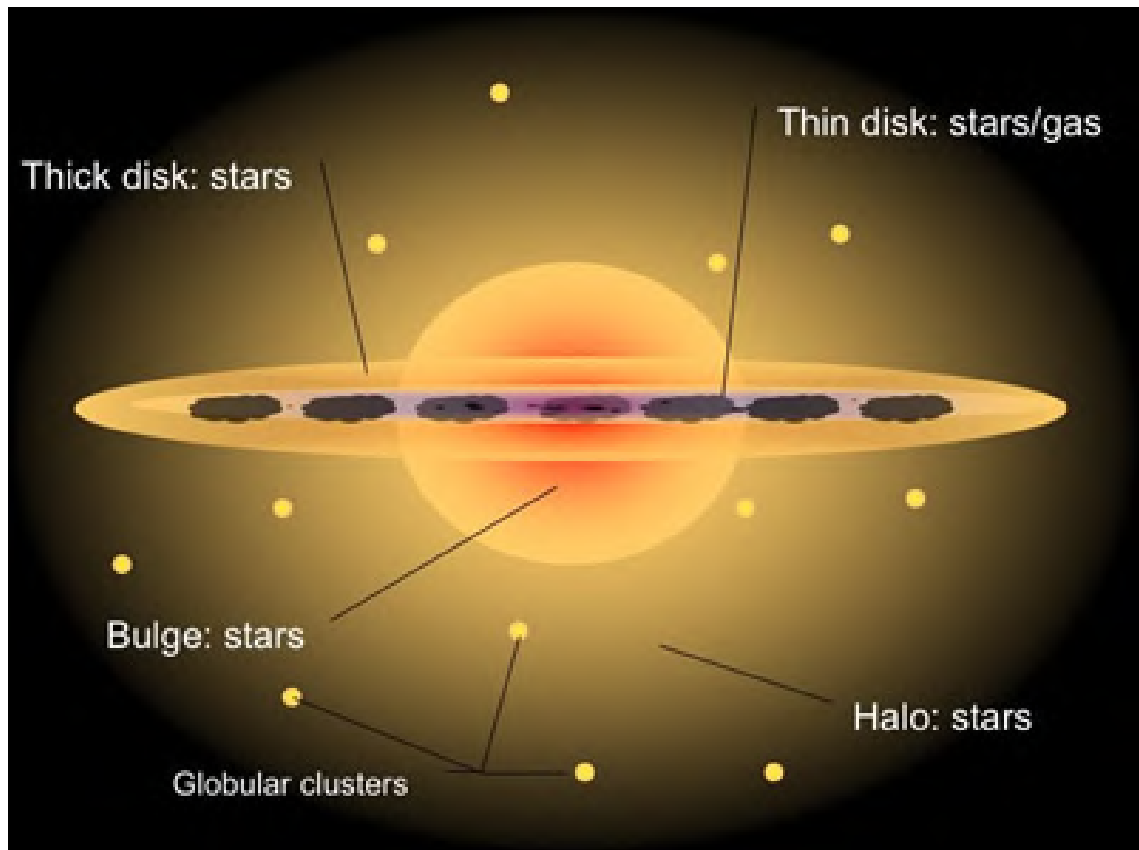
Figure 2.2: Artistic representation of the structures of the Milky Way. In this picture is shown also the main composition of the structures. The Sun lies near the Galactic plane at $z \sim 27$ pc as in Chen et al. 2001 and belongs to the thin disk.

thin normalization is $\sim 0.5\%$. We chose to model the perpendicular density profile following the more recent work of Jurić et al. 2008 because is still used as a reference for current works. In this paper, the authors fit data using a double exponential model for thin and thick disk and a two-axial power-law ellipsoid model for the halo:

$$\rho(R, z) = \rho_{thin}(R, z) + \rho_{thick}(R, z) + \rho_{halo}(R, z) \tag{2.5}$$

The three density profiles are the following:

$$\rho_{thin}(R, z) = \rho_{thin}(R_\odot, 0)e^{\frac{R_\odot}{L_{thin}}} \, exp\left(-\frac{R}{L_{thin}} - \frac{z}{h_{thin}}\right) \tag{2.6}$$

$$\rho_{thick}(R, z) = f_D\rho_{thin}(R_\odot, 0)e^{\frac{R_\odot}{L_{thick}}} \, exp\left(-\frac{R}{L_{thick}} - \frac{z}{h_{thick}}\right) \tag{2.7}$$

$$\rho_{halo}(R, z) = f_H\rho_{thin}(R_\odot, 0)\left[\frac{R_\odot}{\sqrt{R^2 + (z/q)^2}}\right]^n \tag{2.8}$$

where $\rho_{thin}(R_\odot, 0)$ is the thin disk normalization, and $R_\odot$ is the Sun's radial position in galactocentric coordinates. L_{thin} and L_{thick} are the scale lengths respectively for the thin and thick disks, h_{thin} and h_{thick} are the scale heights for the disks, and f_D, f_H are the thick-to-thin disk normalization and the halo-to-thin disk normalization. The halo density profile is then defined also by the parameters q which sets the halo ellipticity and n which is the power-law index. The values for all the parameters described are shown in Table 2.2. The thin disk normalization is not included in the Table as we will calculate it basing on the observed surface density values given by the Oort density. The Sun vertical position is essentially on the Galactic plane, namely $z_\odot \sim 27\,pc$ (Chen

Parameter	Value
$R_\odot$	8200 pc
L_{thin}	2600 pc
L_{thick}	3600 pc
h_{thin}	300 pc
h_{thick}	900 pc
f_D	0.12
f_H	0.0051
q	0.64
n	2.77

Table 2.2: In this Table are shown the parameters adopted for the computation of the density profile. All the parameters except $R_\odot$, taken as eq. (2.2), are the best fit found by Jurić et al. 2008.

et al. 2001). The profile (2.5), for our purpose of studying the solar neighbourhood, has been calculated at the Sun's position from the Galaxy centre, $R_\odot = 8.20$ kpc. We can thus neglect for this specific case the dependence from the radial coordinate R for the thin and thick disk profiles,

obtaining:

$$\rho_{thin}(z) = \rho_{thin}(R_\odot, 0)\, exp\left(-\frac{z}{h_{thin}}\right) \tag{2.9}$$

$$\rho_{thick}(z) = f_D \rho_{thin}(R_\odot, 0)\, exp\left(-\frac{z}{h_{thick}}\right) \tag{2.10}$$

The total vertical density distribution is therefore the linear combination of (2.9), (2.10) and (2.8):

$$\rho(z) = \rho_{thin}(z) + \rho_{thick}(z) + \rho_{halo}(R_\odot, z) \quad . \tag{2.11}$$

This profile is normalized for the Oort density (2.4) as follows:

$$2\int_0^{z_{max}} \rho(z)dz = 2\int_0^{z_{max}} (\rho_{thick}(z) + \rho_{thin}(z) + \rho_{halo}(R_\odot, z))dz = \Sigma_* \quad , \tag{2.12}$$

where $z_{min} = -1100$ pc and $z_{max} = 1100$ pc as the used Oort density is calculated in this z-range. From the results of this calculation we can get the value for the thin disk normalization $\rho_{thin}(R_\odot, 0) = 4.3 \cdot 10^{-2}\,\mathrm{M_\odot pc^{-3}}$, then adopting the thick-to-thin disk normalization ratio of Table 2.2 we calculated the thick disk normalization as $f_D \rho_{thin}(R_\odot, 0) = 5.2 \cdot 10^{-3}\,\mathrm{M_\odot pc^{-3}}$, and using the halo-to-thin disk normalization we get $f_H \rho_{thin}(R_\odot, 0) = 2.2 \cdot 10^{-4}\,\mathrm{M_\odot pc^{-3}}$. The density profiles obtained are shown in Figure 2.3 where the total density and its components are superposed. The thin disk prevails within $z \sim 1000$ pc, the thick disk becomes important from $z \sim 1000$ pc to $z \sim 4000$ pc and then the halo is prevailing at higher z as can be see in Figure 2.4.

We calculated the mean density $< \rho >$ for the thin disk using the density profile $\rho(z)$ (2.11) as follows:

$$< \rho > = \frac{1}{h_{thin}} \int_0^{h_{thin}} (\rho_{thin}(z) + \rho_{thick}(z) + \rho_{halo}(R_\odot, z))dz \quad , \tag{2.13}$$

where $h_{thin} = 300$ pc as in Table 2.2. The local mean density is therefore $< \rho > = 3.2 \cdot 10^{-2}\,\mathrm{M_\odot pc^{-3}}$. We will use this value to normalize our models of Star Formation Rate and Present Day Mass Function to the local stellar density to get a representative model for the Sun's neighbourhood.

2.5 Initial Mass Function

Stellar formation takes place when a cold interstellar gas cloud reaches the Jeans' critical mass so the effect of gravity begins to overcome the expansion of the gas, allowing the cloud to collapse. The outcomes of this process are the classic stars we observe and study.

The idea is, a gas cloud doesn't generate a single star but a Simple Stellar Population, SSP, that is, a
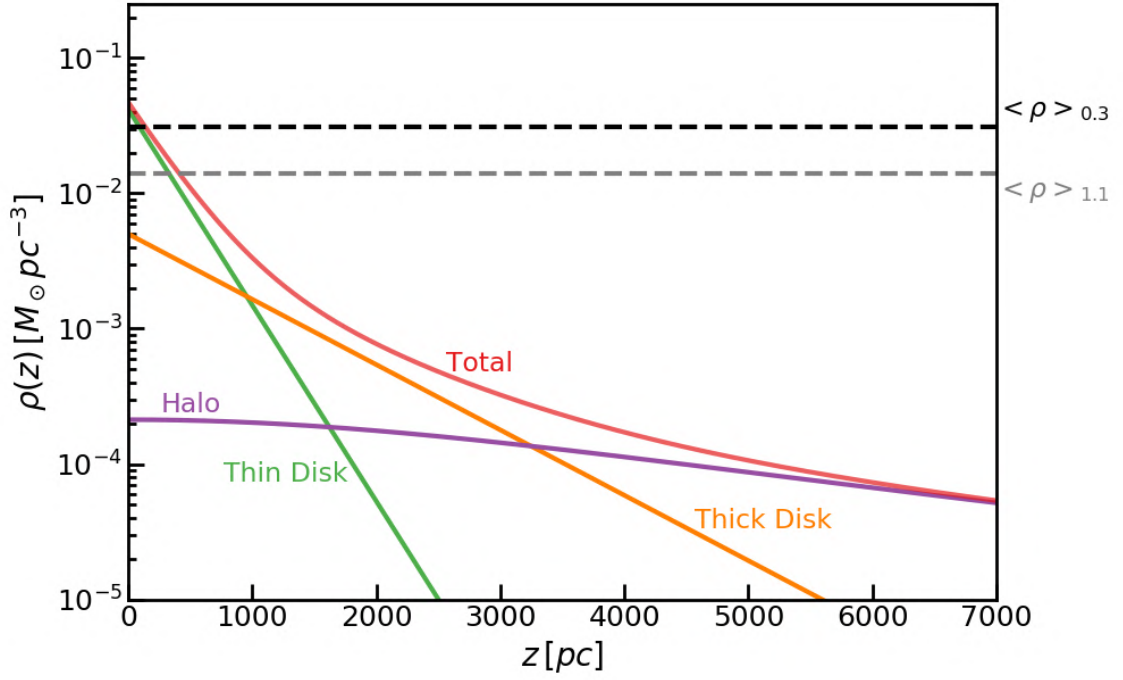
Figure 2.3: Disk density profile (red) with the three components, thin disk (green), thick disk (orange), and halo(purple), normalized as (2.12).

certain number of stars distributed along with different masses. The Initial Mass Function, IMF, is the function that allows us to study this distribution by telling us the star fraction between the mass M and $M+dM$. The IMF is a useful tool in astrophysics to study the Galaxy's mass budget and its star formation mechanism. This function was introduced by Salpeter 1955, successive studies were carried on by other astronomers during the years and still the IMF is an open issue. Our knowledge (its functional form and properties, its applications...) should improve with new and more deep observations of stars in the Milky Way as the ones given by the Gaia mission, the latest and most accurate observing mission. For this thesis work we should model the mass budget in the Solar neighbourhood with the Present Day Mass Function (Sec. 3.4). To do this, there's the need to use an IMF model that is representative of the Solar neighbourhood. Our expectation is that there should be an high density of low-mass objects such as planets and dwarf stars and low density of high mass stars. For historical reasons we choose to use the Salpeter IMF (Subs. 2.5.1) even if there will be the need to modify its behaviour in the low-mass regime due to diverging problems as will be explained in Subs. 2.5.4. Taking into account the low-mass issue we choose two other IMFs for our calculations: one is the Miller and Scalo (Sect. 2.5.2) and the other is given by Chabrier (Subs. 2.5.3).

The IMF can be defined as a probability function to describe the probability of a star to have a
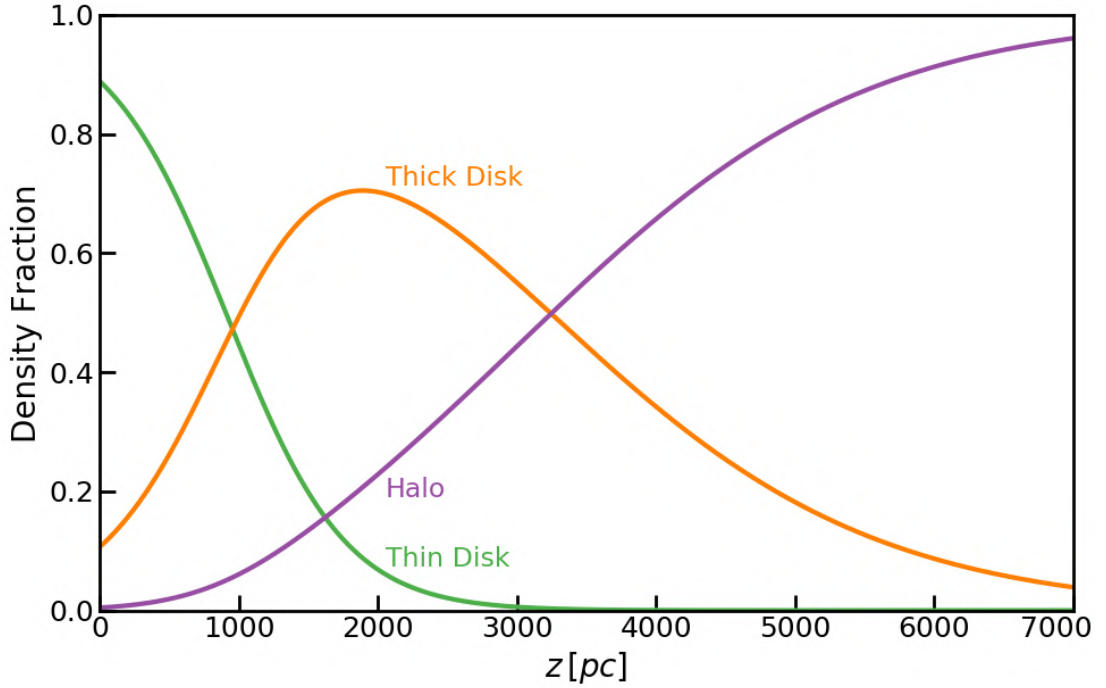
Figure 2.4: Ratios of the subcomponents to the total density distribution.

mass in the range $[M; M + dM]$ thus the normalization is the following:

$$\int_{0.1M_\odot}^{100M_\odot} \xi(M)M dM = 1\,M_\odot \quad , \tag{2.14}$$

we want to model a SSP so the integration range spans from the minimum mass necessary to trigger hydrogen burning in the nucleus ($0.1\,M_\odot$) to the maximum mass given by hydrostatic equilibrium ($100\,M_\odot$). All the IMFs computed are shown in Figure 2.6 where light green represents the mass range studied in each reference paper and dark green represents our extrapolation of the function. In Figure 2.7 superposed IMFs are plotted with annotated mass related objects as defined in Table 4.3. In order to do this, we changed $\xi(log(M))$ function to the $\xi(M)$ form as:

$$\xi(M) = \frac{1}{M\,ln(10)}\xi(log(M)). \tag{2.15}$$

Usually most of the IMFs used or created are power laws and by convention if the IMF is in the form $\xi(M)$ the exponent is represented by the letter s while if the IMF is in the $\xi(log(M))$ form the exponent is represented as x with the relation $x = s - 1$. For the Present Day Mass function in Section 3.4 the $\xi(M)$ form is used.

2.5.1   Salpeter IMF

In his paper, Salpeter 1955, Salpeter started remarking the difference between stars in globular clusters and stars of the Solar neighbourhood. The former ones are all almost of the same age and mass and can be helpful to study stars of a very narrow mass range while the latter have vaster age and mass ranges and can be used to construct a luminosity function. In his work Salpeter took the data from previous studies. The dataset used included stars with magnitude M_v in the range $[-4.5; +13.5]$ and some corrections have been made in order to use only main sequence stars. We can translate the magnitude range in a mass range that helps us identify what masses were involved in this calculation. The mass range was from $M = 0.32 \, \mathrm{M_\odot}$ to $M = 17 \, \mathrm{M_\odot}$. In this way, Salpeter firstly calculated the luminosity function. He then calculated the 'original luminosity function' and from this one the 'original mass function', namely the Initial Mass Function, finding a power law relation:

$$\xi(M) = AM^{-s} \quad ; \tag{2.16}$$

$$\xi(log(M)) = BM^{-x} \quad , \tag{2.17}$$

where $s = 2.35, A = 0.17 \, \mathrm{M_\odot^{-1}}, x = 1.35$, and $B = 0.39 \, (\log \mathrm{M_\odot})^{-1}$ is the normalization as (2.14).

2.5.2   Miller & Scalo IMF.

The second IMF is from Miller and Scalo 1979. In their work the authors start from the luminosity function to calculate the Present Day Mass function, that shows how the mass is distributed at the present time. They use a more complex law than the Salpeter one that takes into account also the slope of the mass-luminosity relation, the vertical distribution of stars, and the fraction of stars still on the main sequence. The authors make a very detailed study considering also the various stellar evolution features and calculated the Present Day Mass Function in the mass range $[0.11-61]$ $\mathrm{M_\odot}$. Starting from this, the Miller and Scalo find the IMF trying different birthrates in order to

fit the observations. Their approach returned a segmented form for the IMF:

$$\xi(M) = \begin{cases} A_1 M^{-s_1} & 0.1 < M/\mathrm{M_\odot} < 1.0 \\ A_2 M^{-s_2} & 1.0 < M/\mathrm{M_\odot} < 10 \\ A_3 M^{-s_3} & 10 < M/\mathrm{M_\odot} \end{cases} , \qquad (2.18)$$

$$\xi(\log M) = \begin{cases} B_1 M^{-x_1} & 0.1 < M/\mathrm{M_\odot} < 1.0 \\ B_2 M^{-x_2} & 1.0 < M/\mathrm{M_\odot} < 10 \\ B_3 M^{-x_3} & 10 < M/\mathrm{M_\odot} \end{cases} . \qquad (2.19)$$

In 2.3 are tabulated the coefficients and exponents values.

$\xi(M)\ [\mathrm{M_\odot^{-1}}]$		$\xi(\log M)\ [(\log \mathrm{M_\odot})^{-1}]$	
A_1	0.31	B_1	0.72
A_2	0.31	B_2	0.72
A_3	1.73	B_3	4.00
s_1	1.4	x_1	0.4
s_2	2.5	x_2	1.5
s_3	3.3	x_3	2.3

Table 2.3: Coefficients and exponents of the laws (2.18) and (2.19) calculated using the normalization (2.14) and the relation (2.15).

2.5.3 Chabrier IMF.

Chabrier studied for a long time the IMF issue and produced many papers in which he modelled various functions and confronted them with data and other authors' work. For our work we focused on the studies in the years [2001-2003] during which Chabrier published three papers and studied especially the low-mass domain of the IMF. In Chabrier 2001 the author models the M-dwarf mass range [0.1 − 0.794] $\mathrm{M_\odot}$. In this paper Chabrier proposes 3 different IMFs aiming to find a good function to fit the stellar mass distribution. One of them is an exponential IMF, another one is a two-leg IMF and the last one is lognormal. The author concludes that all the three IMFs reproduce well the low mass domain and the Exponential one seems to be best compromise between the high-mass tail and the low-mass end of the stellar distribution:

$$\xi(M) = A M^{-s} \exp\left[-\left(\frac{m_o}{M}\right)^\beta \right] \qquad (2.20)$$

$$\xi(\log M) = B M^{-x} \exp\left[-\left(\frac{m_o}{M}\right)^\beta \right] \qquad (2.21)$$

where $m_0 = 716.4\,\text{M}\odot$, $\beta = 0.25$, and the other parameters are shown in Table 2.4. The use of this function shows a similar approach to the Schechter luminosity function (Schechter 1976) for the galaxies. In Chabrier 2002 the author uses a broken IMF which finds to describe well the L-dwarfs domain in the mass range $[0.001 - 0.072]\,\text{M}\odot$:

$$\xi(M) = \begin{cases} A_1 \left(\frac{M}{m_0}\right)^{-s_1} & M < 0.1\,\text{M}\odot \\ A_2 \left(\frac{M}{m_0}\right)^{-s_2} & M > 0.1\,\text{M}\odot \end{cases} \qquad (2.22)$$

$$\xi(\log M) = \begin{cases} B_1 \left(\frac{M}{m_0}\right)^{-x_1} & M < 0.1\,\text{M}\odot \\ B_2 \left(\frac{M}{m_0}\right)^{-x_2} & M > 0.1\,\text{M}\odot \end{cases} \qquad (2.23)$$

where the stellar massi is expressed as $m_0 = 0.1\,\text{M}\odot$ units, and the parameters can be found in Table 2.4. Finally in Chabrier 2003 the author sums up the recent determinations for IMFs and PDMFs and concludes that the functional form that best fits the observations is a gaussian form for masses below $1\,\text{M}\odot$ and an exponential one over $1\,\text{M}\odot$ for the mass range $[0.1 - 100]\,\text{M}\odot$. As suggested by Chabrier in this paper and proposed also by other authors, e.g. Lucas and Roche 2000, Bate, Bonnell, and Bromm 2003, and Luhman 2012, we added a constant part below 0.01 $\text{M}\odot$:

$$\xi(M) = \begin{cases} A_1 M^{-1} & M < 10^{-2}\,\text{M}\odot \\ A_2 M^{-1} \exp\left[-\frac{(\log M - \log m_c)^2}{2\sigma^2} \right] & 10^{-2} < M/\text{M}\odot < 1.0 \\ A_3 M^{-s} & M > 1.0\,\text{M}\odot \end{cases} \qquad (2.24)$$

$$\xi(\log M) = \begin{cases} B_1 & M < 10^{-2}\,\text{M}\odot \\ B_2 \exp\left[-\frac{(\log M - \log m_c)^2}{2\sigma^2} \right] & 10^{-2} < M/\text{M}\odot < 1.0 \\ B_3 M^{-x} & M > 1.0\,\text{M}\odot \end{cases} \qquad (2.25)$$

where also in this case the mass is expressed in $m_c = 0.079\,\text{M}\odot$ units, $\sigma = 0.69$, and the coefficients and exponents are shown in Table 2.4.

For the next calculations of the PDMF we will use this last lognormal IMF and the Salpeter (2.16) and Miller and Scalo (2.18) ones.

2.5.4 Investigating the low-IMF: planets.

For this work we want to study the sub-stellar and planet population. We therefore extrapolated the IMFs described in the previous section down to $1\,\text{M}_{Jup} = 10^{-3}\,\text{M}\odot$ and calculated the numer-

Exponential			
$\xi(M)\,[\mathrm{M}_\odot^{-1}]$ (2.20)		$\xi(\log M)\,[(\log\mathrm{M}_\odot)^{-1}]$ (2.21)	
A	42.8	B	98.57
s	3.3	x	2.3
Two-leg			
$\xi(M)\,[\mathrm{M}_\odot^{-1}]$ (2.22)		$\xi(\log M)\,[\log(\mathrm{M}_\odot)^{-1}]$ (2.23)	
A_1	0.10	B_1	0.23
A_2	0.10	B_2	0.23
s_1	1.55	x_1	0.55
s_2	1.0	x_2	0
Lognormal			
$\xi(M)\,[\mathrm{M}_\odot^{-1}]$ (2.24)		$\xi(\log M)\,[\log(\mathrm{M}_\odot)^{-1}]$ (2.25)	
A_1	0.83	B_1	1.93
A_2	0.85	B_2	1.95
A_3	0.24	B_3	0.55
s	2.3	x	1.3

Table 2.4: Coefficients and exponents of the illustrated Chabrier laws (reference to the equations are in the table) calculated using the normalization (2.14) and the relation (2.15).

ical and mass fraction given by the IMFs previously described.

Before showing the results, is convenient to describe briefly the relations between the s exponents that characterize the IMFs. In Table 2.6 are calculated the exponents of the following analytical expressions:

$$A \int M^{-s} dM = \frac{A}{1-s} M^{1-s} \tag{2.26}$$

$$A \int M \cdot M^{-s} dM = \frac{A}{2-s} M^{2-s} \tag{2.27}$$

where the first (2.26) if integrated in a mass range represents the number of stars while the second one (2.27) represents their mass for mass range of integration. If we follow Table 2.6 and focus on the last column $2-s$, we can see that the Salpeter one is the only IMF function that has a negative exponent thus if we integrate in the low mass range this function will diverge.

The solution to this problem is to modify the behaviour of the Salpeter IMF. In order to do this, we can make an analogy with the mass distribution of the Solar System. Since both our SSP and the Solar System have a total mass of roughly $1\,\mathrm{M}_\odot$ we can compare our SSP to the distribution in mass and number of planets in the Solar System with respect to the Sun. Figure 2.5 shows the mass and number proportion for planets with respect to the Sun. The first chart in the first row explains that the mass of Solar System bodies is only a few percents ($\sim 0.1\%$) of the total Solar System mass while the other charts shows us that the number of sub-stellar bodies is very high, thus we have a big populations of low mass objects that doesn't contribute much to the total mass
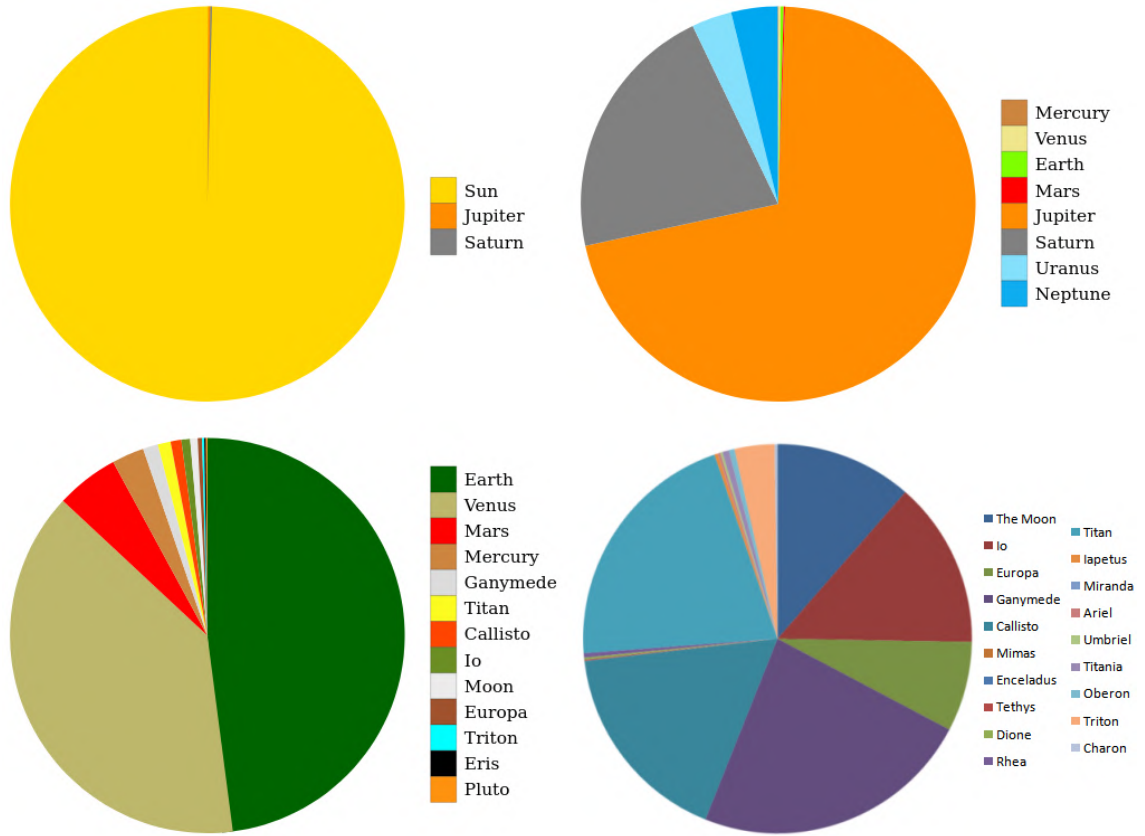
Figure 2.5: Pie charts to show the proportions between objects in the Solar System.

budget.

We can also establish an upper limit for a functional model of a mass closed system as the Solar System (or an SSP). If the Solar System has a total mass M_{SS}, most of its mass as said before is composed by the Sun's mass and the remaining is given by the less massive objects. We can thus set an upper limit to the number of object of the same mass that can possibly compose this remaining mass of the Solar System. For example, we can calculate the maximum number of Jupiter-like planets that can compose the Solar System as follows:

$$N_{Jup} = \frac{M_{SS} - M_{\odot}}{M_{Jup}} \qquad (2.28)$$

this relation is true for every object of mass M thus we can generalize this relation obtaining an upper limit for the number of objects that trend as $N(M) \propto M^{-1}$:

$$N(M) = \frac{M_{SS} - M_{\odot}}{M} \qquad . \qquad (2.29)$$

In Table 2.5 are shown values for the main Solar System objects.

Object	Mass $[\mathrm{M}_{Jup}]$	Number
Jupiter	1	1.5
Saturn	0.30	4.9
Neptune	0.053	27
Uranus	0.045	32
Earth	0.0031	466
Venus	0.0025	572
Mars	0.00034	4339

Table 2.5: In this table are calculated the number of objects of the same mass as the seven main Solar System objects as if they would compose the totality of the remaining Solar System mass as (2.29).

Keeping in mind this analogy, we want to re-model the Salpeter IMF in the low mass domain to avoid diverging behaviours and to resemble the Solar System scenario. To do this, we choose to maintain constant the IMF below $0.1\,\mathrm{M}_\odot$:

$$\xi(M) = \begin{cases} A_1 & M < 0.1\,\mathrm{M}_\odot \\ A_2 M^{-s} & M < 0.1\,\mathrm{M}_\odot \end{cases} \tag{2.30}$$

As we will see especially in Table 2.8 this alteration doesn't resembles perfectly the Solar System scenario as the low mass domain still composes the $\sim 16\%$ of the total mass. The choice of a constant trend is due to the fact that for avoiding diverging behaviours the trend should be $s < 2$, in this way in the last column of 2.6 the exponent will be $2 - s \geq 0$. The choice of $s = 0$ is mainly due to simplify the computation and to the known errors in the determination of a good mass luminosity relation for the sub-stellar regime since in this mass range the sub-stellar objects are fully convective and if still there isn't a consolidate theory there can be over- or underestimates of the numerical and mass budget. Also in literature we can find confirm of the unsuitability of the Salpeter IMF in the low mass range as in Pardi and Ferrini 1994 that remark that there is no theoretical reason for the Salpeter function behaviour for low masses. From now on, we will use this modified Salpeter IMF in our calculations.

We can now calculate the numerical fraction of planets over the total which is calculated as fol-

$\xi(M)$	s	$1 - s$	$2 - s$
Salpeter, eq. (2.16)	2.35	-1.35	-0.35
Miller & Scalo, eq (2.18)	1.4 $(M < 1\,\mathrm{M}_\odot)$	-0.4	0.6
Lognormal, eq. (2.24)	1 $(M < 1\,\mathrm{M}_\odot)$	0	1

Table 2.6: Values for the exponents used in the three IMFs and for their integrations.

lows:

$$\frac{N_{planets}}{N_{tot}} = \frac{\int_{0.001 M_\odot}^{0.1 M_\odot} \xi(M) dM}{\int_{0.001 M_\odot}^{100 M_\odot} \xi(M) dM} \quad . \tag{2.31}$$

The results of this calculations are shown in Table 2.7 and show that the situation can be considered similar for the three IMFs because all of them show a prevalence of planets over the total. This is only a numerical prevalence because if we look at Table 2.8 we can see that the mass ratio of planets over the total is for all the IMF roughly less than the 15%. The mass fraction is thus cal-

$\xi(M)$	Number of planets	Total Number	$N_{planets}/N_{tot}$
Salpeter, eq. (2.30)	3.81	6.65	0.57
Miller & Scalo, eq (2.18)	11.8	13.4	0.883
Lognormal, eq. (2.24)	3.87	5.36	0.722

Table 2.7: For each IMF used the number of planets and the total number of planets are calculated and the fraction over the total as (2.31).

culated re-normalizing the IMF over the sub-stellar range $[0.001 - 0.1]$ $M_\odot$ in order to quantify the mass for the sub-stellar range as follows:

$$\frac{M_{planets}}{M_{tot}} = \frac{\int_{0.001 M_\odot}^{0.1 M_\odot} \xi(M) M dM}{\int_{0.001 M_\odot}^{100 M_\odot} \xi(M) M dM} \quad . \tag{2.32}$$

Table 2.8 shows the results of the calculations. As we said these results show that even if the numerical fraction can be high, planets make only a little fraction of the total mass of the system.

$\xi(M)$	M_{pl} $[M_\odot]$	M_{tot} $[M_\odot]$	$M_{planets}/M_{tot}$	$< M_{pl} > [M_{Jup}]$
Salpeter, eq. (2.16)	$1.9 \cdot 10^{-1}$	1.19	$1.6 \cdot 10^{-1}$	50
Miller & Scalo, eq. (2.18)	$1.4 \cdot 10^{-1}$	1.14	$1.2 \cdot 10^{-1}$	11
Lognormal, eq. (2.24)	$8.3 \cdot 10^{-2}$	1.10	$7.7 \cdot 10^{-2}$	21

Table 2.8: This table shows the mass fraction of planets over the total mass of the stellar population used calculated as in (2.32).

2.6 Star Formation Rate

The ability to create new stars for a galaxy is measured by the Star Formation Rate (SFR) that shows how many solar masses of interstellar gas become stars each year. This quantity is useful to
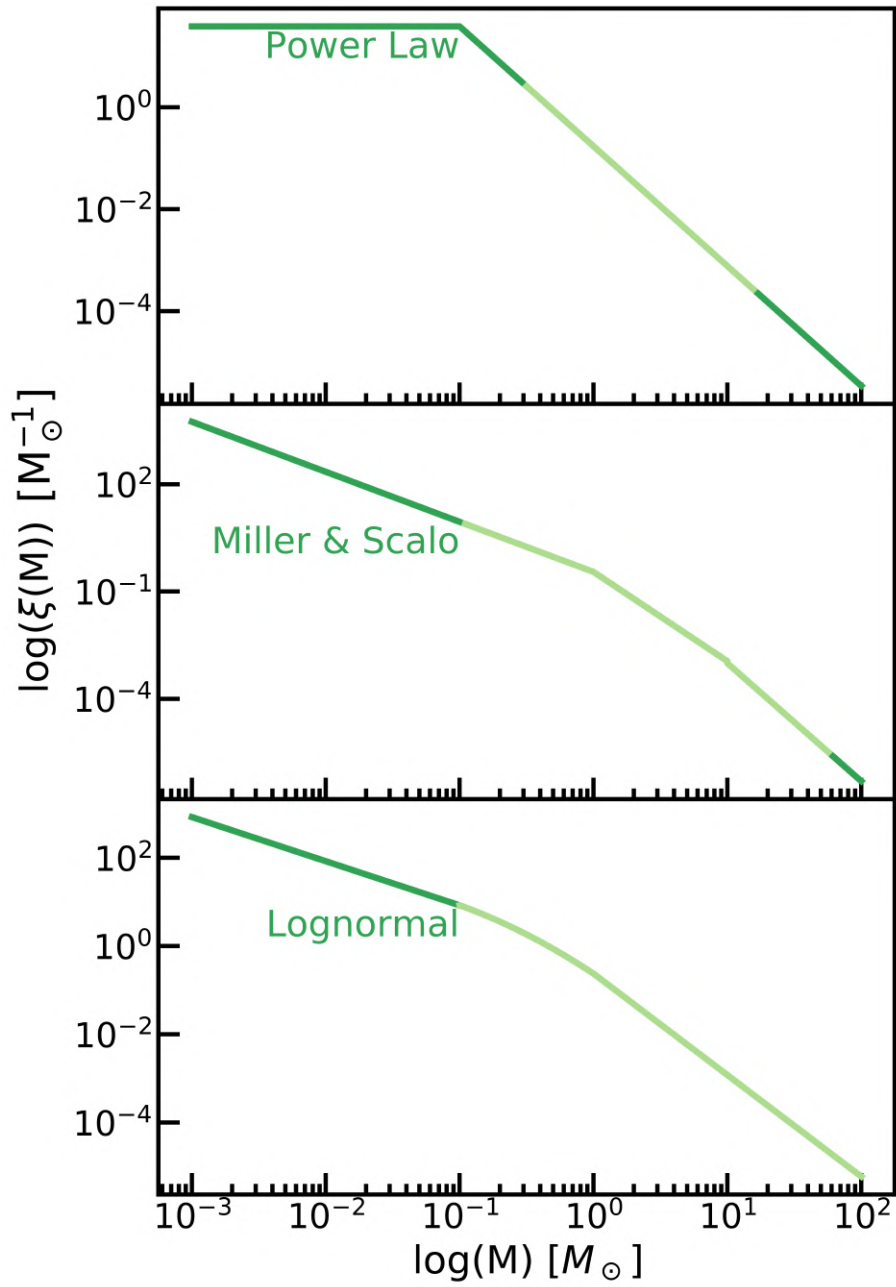
Figure 2.6: In this Figure, used IMFs are plotted. Dark green represents the extrapolated values while light green represents the mass range studied by reference authors.
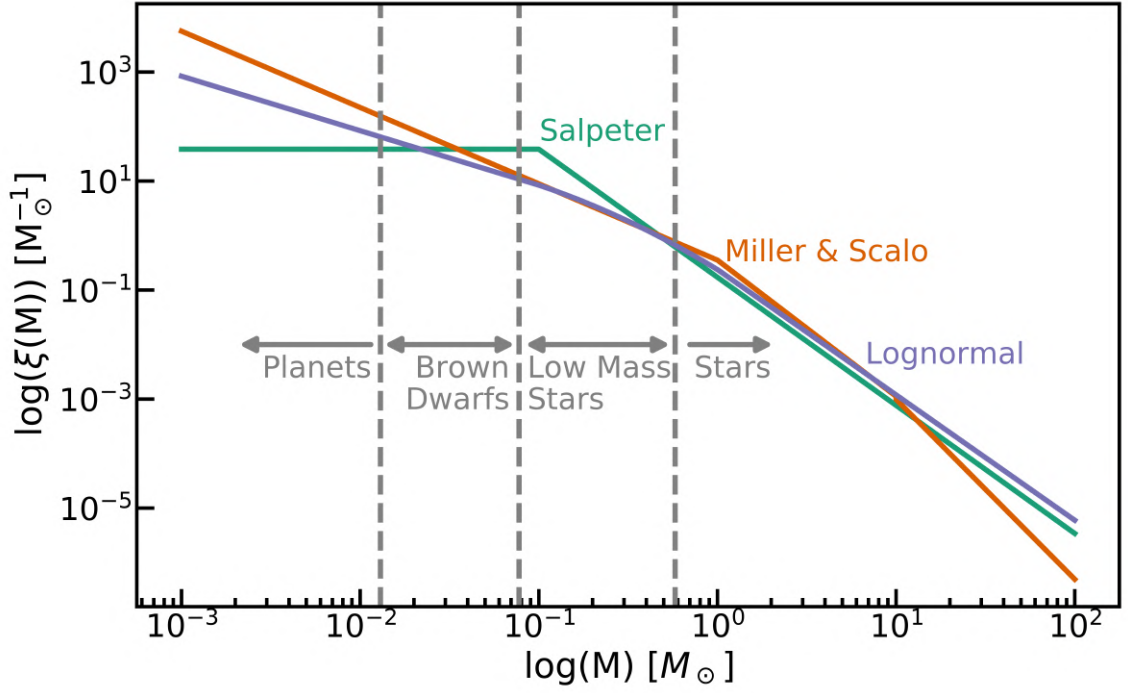
Figure 2.7: Superposition of the calculated IMFs with highlighted planets, brown dwarfs, and stars mass domain.

understanding the degree of galaxy's activity (e.g. a starburst galaxy will have a SFR way higher than an elliptical one). The first studies for an analytical model for the SFR begin with Schmidt 1959 that thought that the SFR should be linked to the total amount of gas in the galaxy. Basing upon data of previous work and upon the studies of the luminosity function (Salpeter 1955) and the distribution of the stars in the Galaxy, Schmidt proposed a general model in which the SFR can be a function of time that depends on the gas density by a power n. Schmidt proposes the following model, for $n = 1$:

$$f(t) = f(0)e^{-\frac{t}{\tau}} \tag{2.33}$$

where $e^{-\frac{1}{\tau}} = P$, P is the gas fraction (usually, $P = 0.20$) and $(1 - P)\tau f(0) = 1$. For $n > 1$:

$$f(t) = f(0)\left[1 + (n-1)\frac{t}{\tau}\right]^{-\frac{n}{n-1}} \tag{2.34}$$

where $\tau = \frac{n-1}{P^{1-n}-1}$ and $(1 - P)\tau f(0) = 1$.

In this thesis we used four different SFR, three of which are Schmidt type $n = 0, n = 1, n = 2$ and the last one is a Levy type SFR.

Our SFRs have dimensions of $[M_\odot yr^{-1}pc^{-3}]$ because is normalized to the local mean stellar den-

sity using 2.13:

$$\int_{T_o}^{T_{gal}} \varphi(t)dt = < \rho > \quad , \tag{2.35}$$

In equation (2.35) the SFR is integrated from the lifetime of the most massive star T_o to Galaxy's age T_{gal}.

The first SFR considered is the constant one:

$$\varphi(t) = A_o \tag{2.36}$$

with $A_o = 3.1 \cdot 10^{-12}$ $M_\odot yr^{-1} pc^{-3}$ as (2.35). The second one is the exponential form ($n = 1$) as said before:

$$\varphi(t) = A_1 e^{-\frac{t}{\tau}}, \tag{2.37}$$

where $\tau = \frac{T_{gal}}{2}$ as in Miller and Scalo 1979, and $A_1 = 7.2 \cdot 10^{-12}$ $M_\odot yr^{-1} pc^{-3}$. We chose also the quadratic case ($n = 2$):

$$\varphi(t) = A_2 \frac{1}{\left(1 + \frac{t}{T_{gal}\tau}\right)^2}. \tag{2.38}$$

where $\tau = \frac{P}{1-P}$, taken as $P = 0.20$ as in Schmidt 1959 and Miller and Scalo 1979, and $A_2 = 3.1 \cdot 10^{-11}$ $M_\odot yr^{-1} pc^{-3}$. Another hypothesis is the one that connects the activity of the galaxy to his morphological type:

$$\varphi(t) = A_3 t^{-\eta}, \tag{2.39}$$

where $A_3 = 1.6 \cdot 10^{-7}$ $M_\odot yr^{-1} pc^{-3}$, and η depends on the morphology of the galaxy. For the Milky Way (Sb), $\eta = 0.5$ as in Buzzoni 2005.

The values for the SFR calculated today, $\varphi(T_{gal})$ are shown in Table 2.9. The values for SFR today range from $0.31 \cdot 10^{-12}$ $\left[M_\odot yr^{-1} pc^{-3}\right]$ to $3.1 \cdot 10^{-12}$ $\left[M_\odot yr^{-1} pc^{-3}\right]$, due to the different behaviour of the functions taken into account, as remarked also by plot in Figure 2.8. In Figure 2.9 is plotted the cumulative function for the SFRs used that shows how in T_{gal} time the total mass formed by different SFRs equals the mass of disk stars.

$\varphi(t)$	$\varphi(T_{Gal})$ $\left[10^{-12}\ M_\odot yr^{-1} pc^{-3}\right]$
Constant, eq. (2.36)	3.1
Schmidt $n = 1$, eq. (2.37)	0.97
Schmidt $n = 2$, eq. (2.38)	0.31
Levy, eq. (2.39)	1.6

Table 2.9: Values of the local SFRs used calculated today ($\varphi(T_{gal})$).
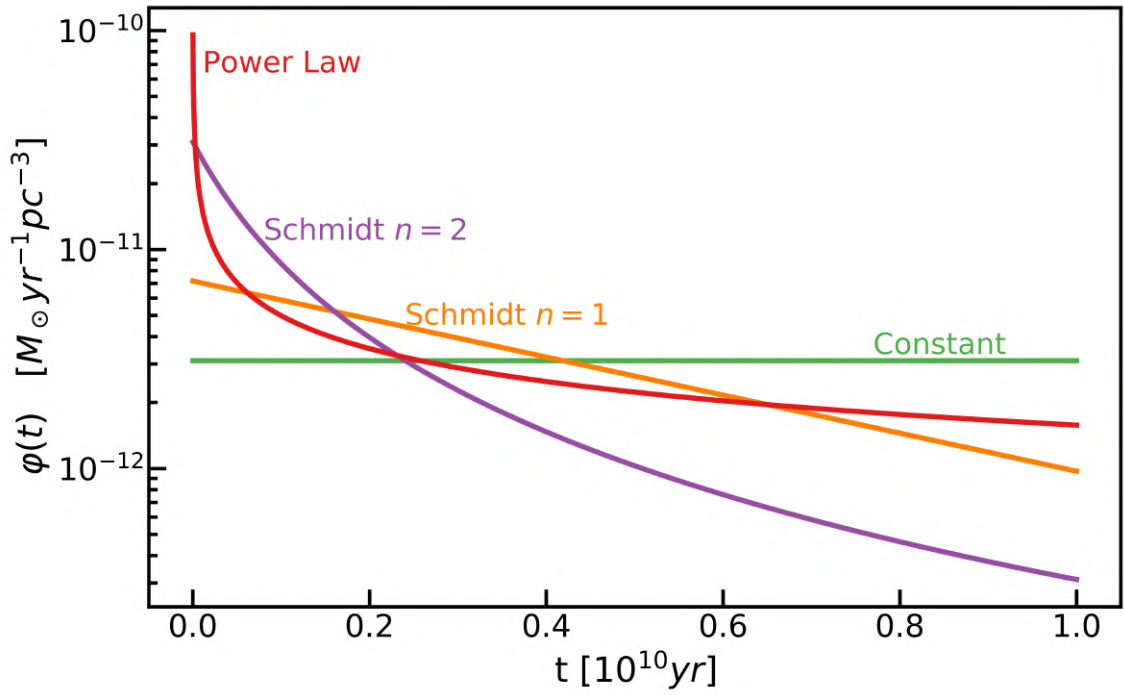
Figure 2.8: Superposition of constant, Schmidt $n = 1$, Schmidt $n = 2$, Levy SFRs.
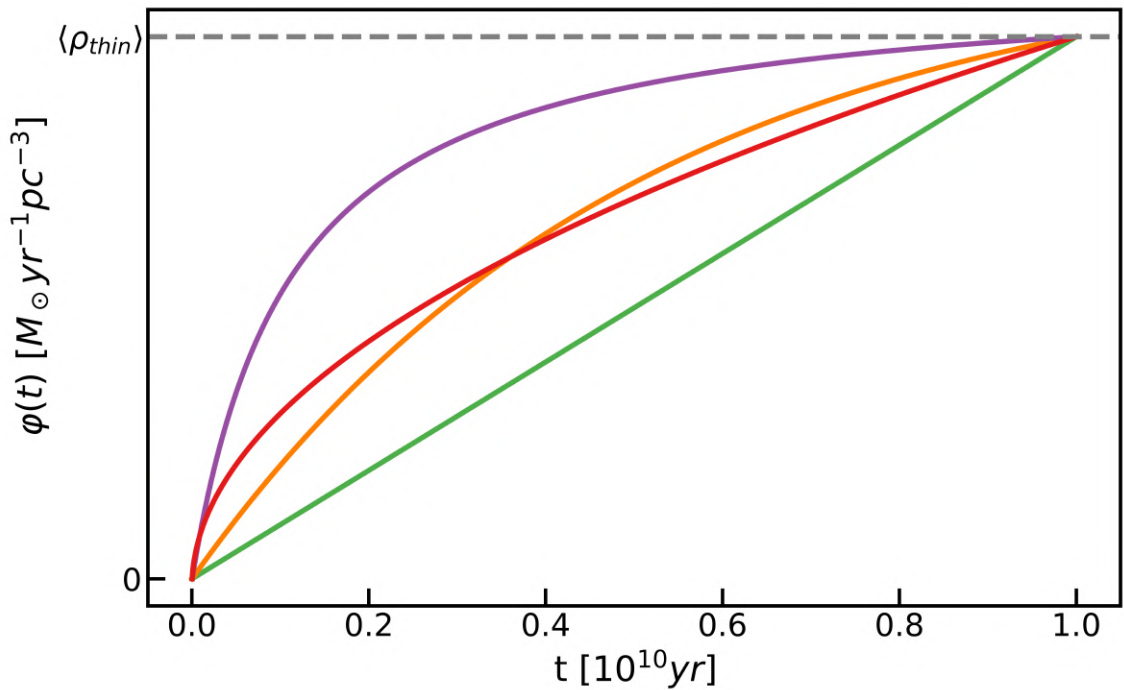
Figure 2.9: Cumulative representation of the SFRs used. After a $T_{gal} = 10$ Gyr the mass of objects formed is equivalent to the Galaxy's mean density.

Chapter 3

The Galaxy properties in the solar neighbor-hood

3.1 Introduction

In this Chapter we will calculate the Present Day Mass Function, PDMF, and give some values for the stellar and remnants density distribution. These values will be compared to data in the next Chapter 4 to see if our calculation could match the latest observations. The PDMF will then be used to give the stellar density around the Sun and, together with the mean velocity of stars and their dynamical limits, will tell us different information on the interactions of stars with the Sun in Chapter 7.

The Chapter will thus start with some fundamentals of stellar evolution given in 3.2 and in Section 3.3 will be proposed a function for the calculation of the Main Sequence lifetime given by Buzzoni 2002.

In Section 3.4 we will discuss the theory of PDMF and show its functional form.

In Section 3.5 we will normalize the PDMF in order to match to the observed stellar density in the Sun neighbourhood and will calculate the amount of stellar remnants.

3.2 Setting the context

To establish the features of the Solar System neighbourhood is important to understand the characteristics of the stellar populations surrounding the Sun and to assess their evolutionary stage.

A star is defined by its ability to burn hydrogen and other elements in its core. The mass of a star sets a limit to the possibility of hydrogen burning ignition in the core that is typically $0.1\,\mathrm{M_\odot}$ while there is a maximum mass of about $100\,\mathrm{M_\odot}$ imposed by hydrostatic equilibrium.

The entire evolution of a star can be studied using the HR diagram which relates the luminosity of a star with its temperature. Once a star completed its formation stage, it's considered a virialized system. Hydrogen burning begins in the core and the star begins its life positioning on the main sequence, MS.

The MS is one of the sequences of the HR diagram and is temporally the longest. Evolution after the MS is very fast for every star and post-MS stages are different depending on the initial mass of the star. We can use as a timescale for the stellar lifetime the time spent on the MS because this represents about 90% of its total lifetime (timescales for evolutionary stages post-MS are almost one magnitude less than the MS ones).

3.3   Stellar Age - Turnoff Mass relation

The MS is the only sequence of the HR diagram that links the luminosity of a star to its mass, from empirical studies we know that $L \propto M^{3.3}$. When the hydrogen burning in the core stops, the star leaves the MS and continues its evolution towards lower temperatures. High mass stars evolve more rapidly than low mass ones, besides higher mass stars will be the first to leave the MS and then gradually lower masses. This generates an important feature in observations called turnoff point (TO) that shows the maximum luminosity (or mass) at which the MS is truncated and is characteristic of the evolutionary stage of a stellar population. In the article of Buzzoni 2002, the TO evolution in function of time is calculated as follows:

$$log\,t = 0.825\,log^2(M_{TO}/120) + 6.43 \tag{3.1}$$

where t is the time expressed in yr and M_{TO} represents the turnoff mass in $\mathrm{M_\odot}$. This relation is shown in Figure 3.1.

3.4   Present Day Mass Function

A disk galaxy like the Milky Way can recycle its gas during its life, based on the galaxy's star formation history. The recycled gas can form new stars at different times, making the galaxy's colours bluer. Star formation in disk galaxies occurs at different times so the galaxy can be modelled ad a
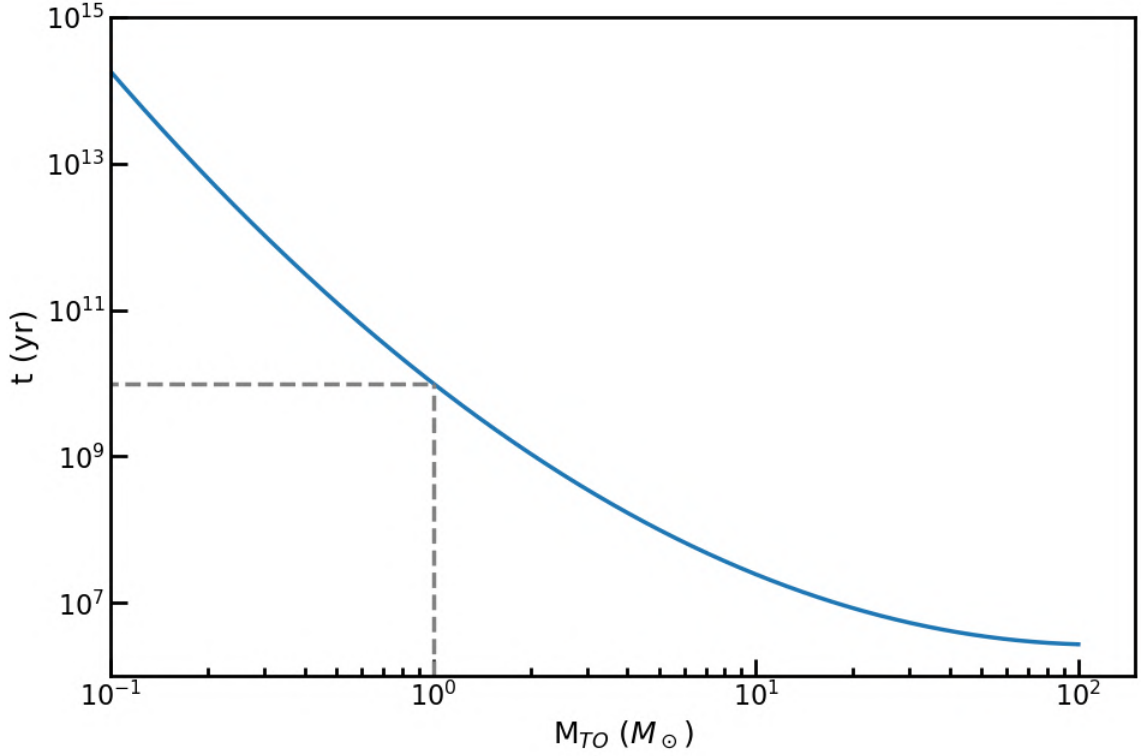
Figure 3.1: Age - Turnoff Mass relation. Grey dashed lines show the Turnoff Mass for a SSP of *10 Gyr*.

Composite Stellar Population, CSP. Globular clusters or elliptical galaxies on the other hand are Simple Stellar Populations: all the stars are generated in a single burst of star formation.

While a SSP is well described using an IMF , to describe a CSP there's the need to know what's the effect of star formation history on the IMF. A CSP can be described using the Present Day Mass Function, PDMF, that at a fixed time t shows the distribution of the stellar mass for volume unit:

$$\Phi(M) = \begin{cases} \xi(M) \int_{T_{gal}-\tau_{MS}}^{T_{gal}} \varphi(t) & \tau_{MS} < T_{gal} \\ \xi(M) \int_{o}^{T_{gal}} \varphi(t)dt & \tau_{MS} \geq T_{gal} \end{cases}, \qquad (3.2)$$

where $\xi(M)$ is one of the IMFs described in Subsection 2.5, $\varphi(t)$ is one of the SFRs in Subsection 2.6, T_{gal} is the age of the galaxy and τ_{MS} represents the main sequence lifetime of a star of mass M and it's calculated using (3.1). This distribution is different based on stellar lifetimes: if a star has a main sequence period greater than the age of the galaxy then the IMF can still be used to describe the stellar population, otherwise, SFR has to be taken in to account.

3.5 Stellar distribution

For this work, we want to describe how the stellar mass is distributed in the solar neighbourhood and, in particular, in the thin disk. The local mean density (2.13) is used to normalize the PDMF $\Phi(M)$ as follows:

$$\int_{0.1M_\odot}^{100M_\odot} \Phi(M)dM = <\rho> \quad . \tag{3.3}$$

This calculation has been done for the IMFs in Subsection 2.5. Each IMF has been multiplied by the SFRs described in Subsection 2.6. The results are shown in Figure 3.2 for a Salpeter IMF, Figure 3.3 for a Scalo IMF, and in Figure 3.4 for a Lognormal IMF. In each figure, the dashed line represents the IMF adopted and the continuous lines are the resulting PDMF having different colours for different SFR.
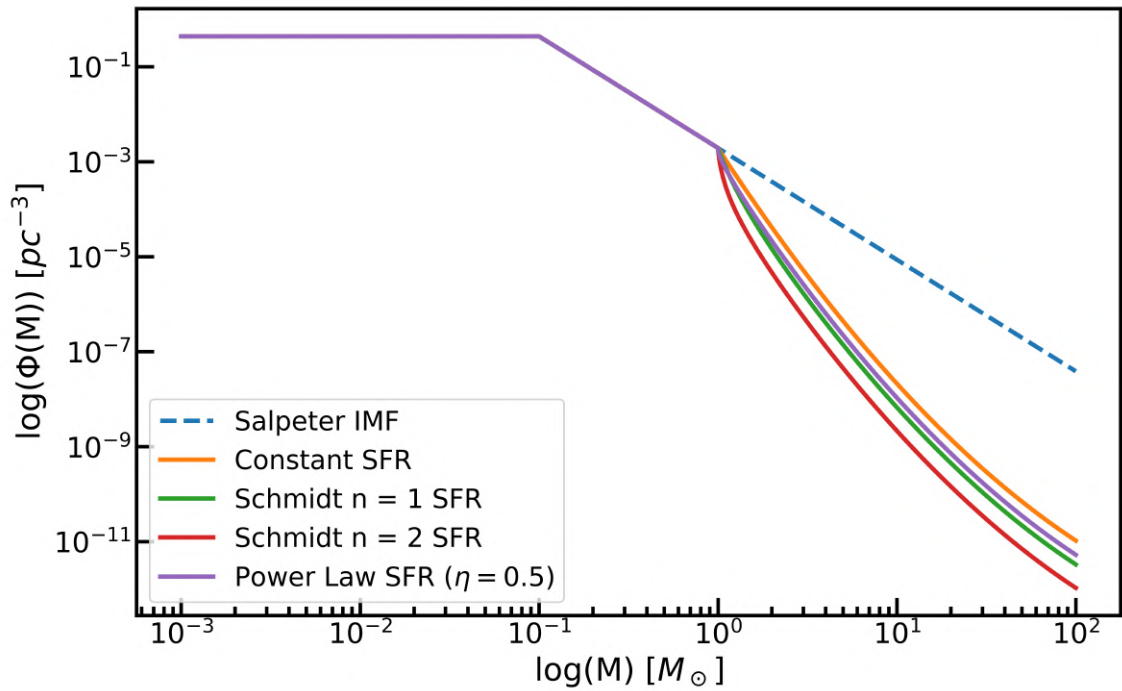
Figure 3.2: PDMF using Salpeter IMF.
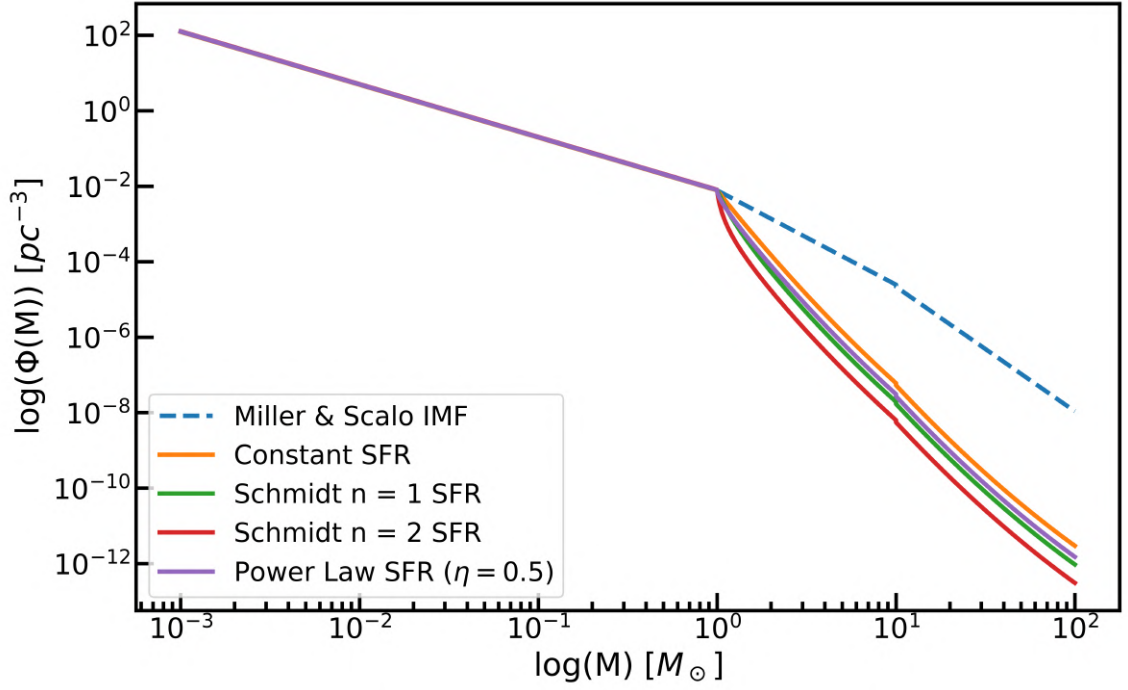
Figure 3.3: PDMF using Miller and Scalo IMF.

3.5.1 Remnants distribution

We also calculated the numerical and mass quantity of stellar remnants such as white dwarfs, neutron stars, and black holes. To do this, the following calculations have been made:

$$N_{rem} = \int_{M(t_o)}^{M_{up}} \xi(M) dM - \int_{M(t_o)}^{M_{up}} \Phi(M) dM \tag{3.4}$$

$$M_{rem} = \int_{M(t_o)}^{M_{up}} \xi(M) M dM - \int_{M(t_o)}^{M_{up}} \Phi(M) M dM \tag{3.5}$$

where $M(t_o)$ is the today turnoff mass and M_{up} is the maximum mass used in our calculations, *100* $M_\odot$. In order to estimate the quantity and the mass of WD remnants we changed M_{up} to *8* $M_\odot$. The results are shown in Table 3.1 in which are tabulated the number and mass of both remnants and white dwarfs, the mean masses, calculated as the ratio between the mass and the number of remnants and WD, and the fraction of WD of the total of remnants.
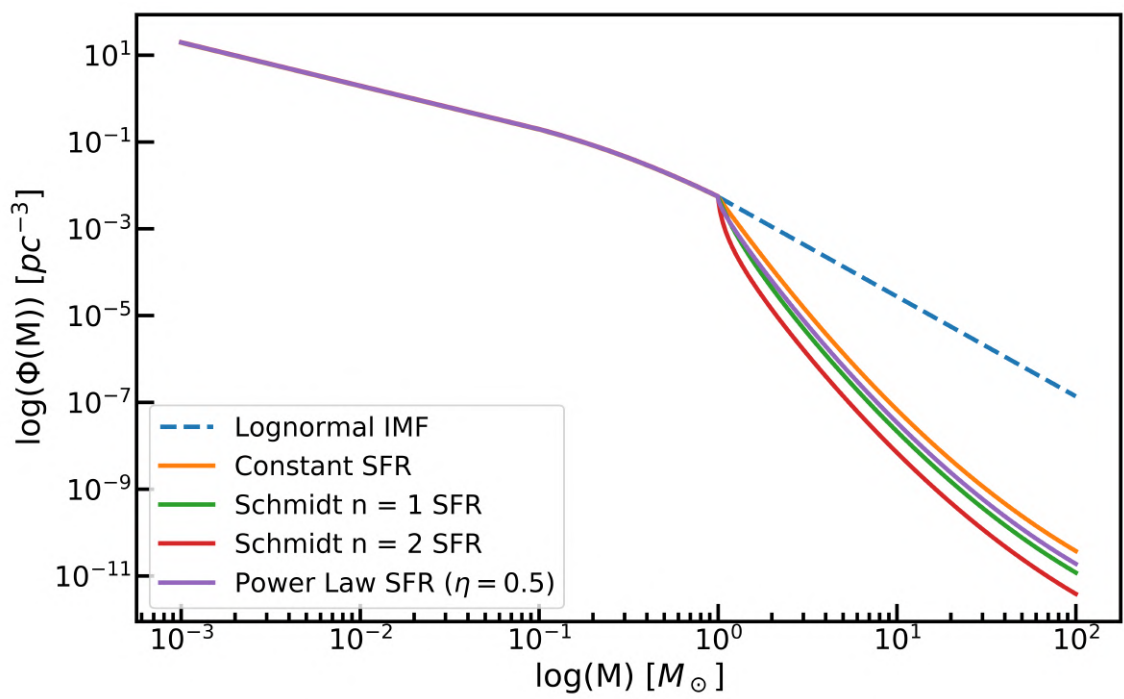
Figure 3.4: PDMF using Lognormal IMF.

$\varphi(t)$	$N_{rem}[pc^{-3}]$	$M_{rem}[M_\odot pc^{-3}]$	$N_{WD}[pc^{-3}]$	$M_{WD}[M_\odot pc^{-3}]$	$\langle M_{rem}\rangle [M_\odot]$	$\langle M_{WD}\rangle [M_\odot]$	N_{WD}/N_{rem}
			Salpeter IMF, eq. (2.30)				
Constant SFR, eq. (2.36)	$1.0\cdot10^{-3}$	$3.9\cdot10^{-3}$	$9.3\cdot10^{-4}$	$2.3\cdot10^{-3}$	3.8	2.5	0.92
Schmidt $n=1$ SFR, eq. (2.37)	$1.2\cdot10^{-3}$	$4.1\cdot10^{-3}$	$1.1\cdot10^{-3}$	$2.6\cdot10^{-3}$	3.5	2.3	0.93
Schmidt $n=2$ SFR, eq. (2.38)	$1.3\cdot10^{-3}$	$4.3\cdot10^{-3}$	$1.2\cdot10^{-3}$	$2.7\cdot10^{-3}$	3.3	2.2	0.94
Levy SFR, eq. (2.39)	$1.2\cdot10^{-3}$	$4.1\cdot10^{-3}$	$1.1\cdot10^{-3}$	$2.5\cdot10^{-3}$	3.5	2.3	0.93
			Miller & Scalo IMF, eq. (2.18)				
Constant SFR, eq. (2.36)	$3.5\cdot10^{-3}$	$1.0\cdot10^{-2}$	$3.3\cdot10^{-3}$	$8.0\cdot10^{-3}$	2.9	2.4	0.95
Schmidt $n=1$ SFR, eq. (2.37)	$4.1\cdot10^{-3}$	$1.1\cdot10^{-2}$	$4.0\cdot10^{-3}$	$9.0\cdot10^{-3}$	2.7	2.2	0.96
Schmidt $n=2$ SFR, eq. (2.38)	$4.8\cdot10^{-3}$	$1.2\cdot10^{-2}$	$4.7\cdot10^{-3}$	$9.9\cdot10^{-3}$	2.5	2.1	0.97
Levy SFR, eq. (2.39)	$4.2\cdot10^{-3}$	$1.1\cdot10^{-2}$	$4.0\cdot10^{-3}$	$9.0\cdot10^{-3}$	2.7	2.2	0.96
			Chabrier IMF, eq. (2.24)				
Constant SFR, eq. (2.36)	$3.0\cdot10^{-3}$	$1.2\cdot10^{-2}$	$2.7\cdot10^{-3}$	$6.9\cdot10^{-3}$	4.0	2.5	0.91
Schmidt $n=1$ SFR, eq. (2.37)	$3.5\cdot10^{-3}$	$1.3\cdot10^{-2}$	$3.2\cdot10^{-3}$	$7.6\cdot10^{-3}$	3.7	2.4	0.92
Schmidt $n=2$ SFR, eq. (2.38)	$4.0\cdot10^{-3}$	$1.4\cdot10^{-2}$	$3.7\cdot10^{-3}$	$8.3\cdot10^{-3}$	3.4	2.2	0.93
Levy SFR, eq. (2.39)	$3.5\cdot10^{-3}$	$1.3\cdot10^{-2}$	$3.2\cdot10^{-3}$	$7.6\cdot10^{-3}$	3.7	2.4	0.92

Table 3.1: Number and mass of remnants and white dwarfs between mass $M(t_0)$ and $8\,M_\odot$. Mean masses are relative to MS progenitors of these evolved object. Last column shows the WD fraction over the total number of remnants.

Chapter 4

Observations - Gaia mission

4.1   Introduction

In this Chapter we will compare our models with latest data from Gaia mission. This step is useful to ensure that our model can be as much representative as possible of the Solar vicinity. Data shown in this Chapter will also be used in Chapter 7 to compare our results to the observations. In Section 4.2 we will give an overview of the Gaia mission, describing the satellite itself and how the data is collected and released.
In Section 4.3 we will compare our work with data from Reylé, C. et al. 2021 which used GAIA data of the first *10* pc from Sun from 3rd Early Data Release.

4.2   The Gaia mission

Gaia is an European Space Agency (ESA) mission based on astrometry techniques. Gaia is an acronym that stood for Global Astrometric Interferometer for Astrophysics but since the working method has changed to astrometry, this acronym is no longer used. The mission goal is to catalogue objects in the solar neighbourhood using astrometry to obtain their spatial and velocity distribution. Gaia is the successor of the Hipparcos[1] mission that lasted from 1989 to 1993 and used astrometry to determine position, proper motions, and photometric data for more than 2,5 million of stars, generating two catalogues, the Hipparcos (of about 110.000 stars) and Tycho-2 (of about 2.5 million stars).

---

1. High Precision Parallax Collecting Satellite
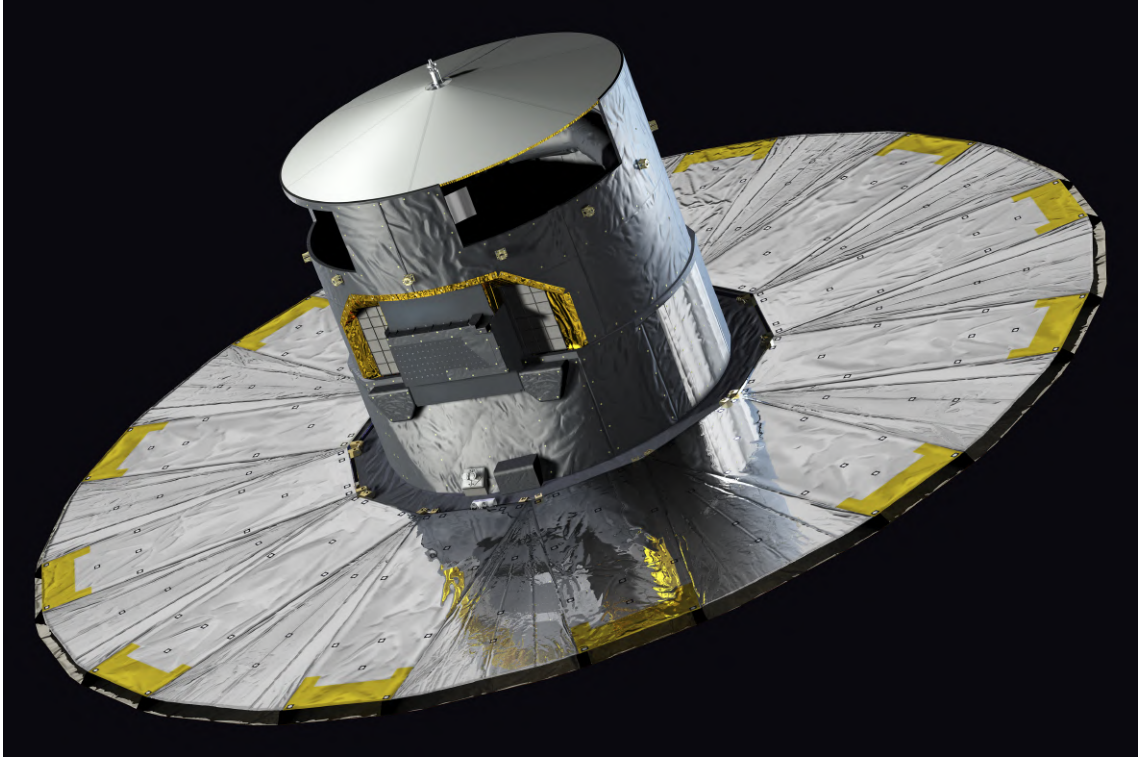
Figure 4.1: Artistic impression of the Gaia satellite. Credits: ESA–D. Ducros, 2013.

Gaia aims with its observations to expand the catalogues given by Hipparcos mission. The Gaia satellite, Figure 4.1, was launched on 19 December 2013 at 09:12:19.6 from French Guiana towards the Lagrange point L_2 of the Sun-Earth-Moon system, reached 26 days after the launch. Lagrangian points are defined by the three body problem as stationary points, five in total, in which the total gravitational force of two massive objects equals the centrifugal force of a small object of negligible mass. If the latter mass is in L_2, it will share its orbit with the second less massive object. For the Sun-Earth-Moon system the second Lagrangian point L_2 is placed in the anti-Sun direction, about $1.5 \cdot 10^6$ km from Earth, and the Gaia satellite shares its orbit with Earth, moving around L_2 point in a Lissajous-type orbit. For the astrometric problem, L_2 point is particularly important to have a known reference system from which to calculate parallaxes. In Figure 4.2 the sky scanning pattern for Data Release 2 (DR2) is shown.

Gaia satellite has a very complex hardware/software composition due to the various tasks that must be accomplished before transmitting data to the ground. Data are detected by different instruments: astrometric, photometric, and spectroscopic ones, in order to obtain different measurements from the light collected by the telescope.

The telescope is composed by two identical mirrors having apertures of 1.45x0.50 m and separated by an angle of 106.5 degrees. Mirrors have 35 m of focal length and the light optical paths are ini-
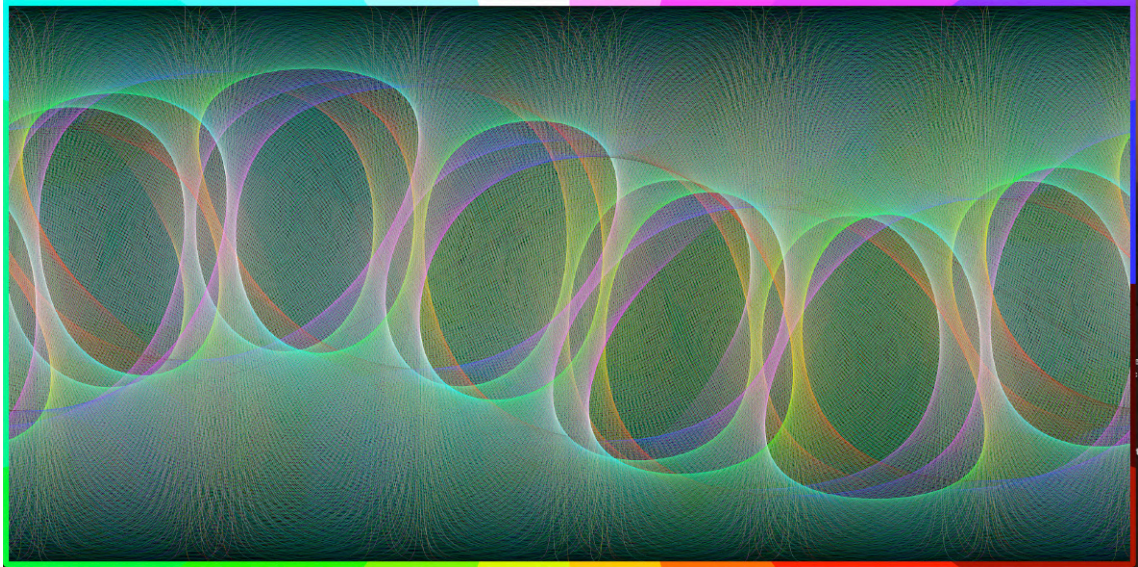
Figure 4.2: This figure shows the scan pattern of Gaia across the sky based on real data. This scan is related to the period between 1 October 2014 and 31 May 2016, that corresponds to DR2 data. The colors show the direction of the scan with legend on the border of the image. Credits: ESA/Gaia.

tially separated and then merged to reach the focal plane. The latter is composed by 106 CCD detectors and has five functions: metrology (to ensure that the wave front is coherent), object detection, astrometry, photometry, and spectrometry.

The astrometric instrument returns distance and parallax for the observed object. The wavelength range of the observations is $330 - 1050$ nm given by the G band photometric Gaia filter. The survey is flux limited thus there isn't a preselection of sources to observe.

The photometric instrument measures the Spectral Energy Distribution, SED, of the source and is composed of two disperser prisms, the first called BP and operating in the wavelength range $330 - 860$ nm and the second one called RP operating in the $640 - 1050$ nm range. These data can be used for photometry, e.g. in Figure 4.3 is shown the HR diagram obtained from the DR2 data.
 The spectroscopic instrument, also called radial-velocity spectrometer, RSV, measures the radial velocities from spectra of the sources. RSV is an integral field spectrograph with a resolution of $R \approx 11700$ that operates in the wavelength range $845 - 872$ nm where is visible the CaII triplet, and the hydrogen Paschen series useful to determine the radial velocity of early-type stars.

Gaia's data can be used for Galactic astrophysics such as to better define the structure and size of the Milky Way, to define the star formation history of our Galaxy, and to study its stellar populations. Gaia's observations are useful also to study stellar astrophysics such as stellar evolution and properties of binary or multiple systems and also can be used to study exoplanets and solar system features. Thanks to Gaia's high resolution, it's possible also to observe brightest stars in galaxies
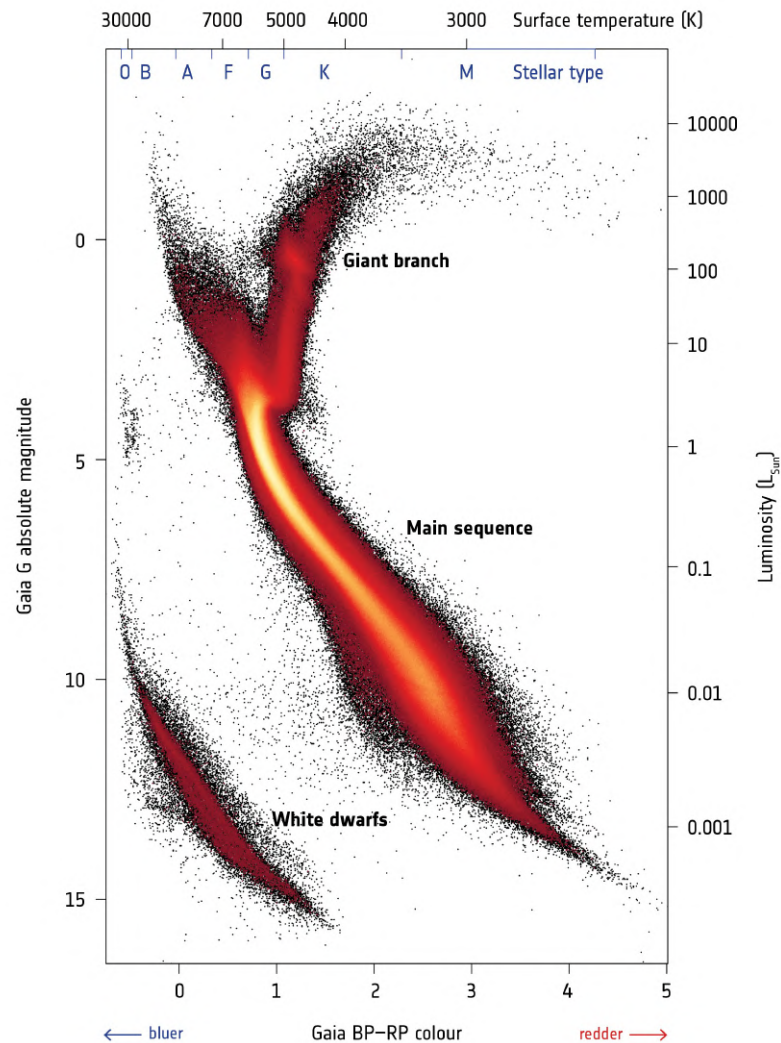
Figure 4.3: Hertzsprung Russel diagram from DR2 Gaia data (> 4 million stars). Credits: ESA/Gaia/DPAC, CC BY-SA 3.0 IGO.

of the Local group, and to observe distant galaxies and quasar as a magnitude limited sample. Gaia's data are collected in a catalogue and published in the so-called data release:

- 1st Data Release, DR1: 14 September 2016;

- 2nd Data Release, DR2: 25 April 2018;

- Early 3rd Data Release, EDR3: 3 December 2020;

- 3rd Data Release, DR3: first half 2022;

with all the data accessible to public. Each data release generates a vaster and more accurate catalogue because Gaia has more time to measure the sources. An example from is in Figure 4.4 in

which the trajectory of 40000 stars are plotted basing on the EDR3 data (twice more accurate than DR2).

Further general references about the Gaia mission can be found in Gaia Collaboration et al. 2016.
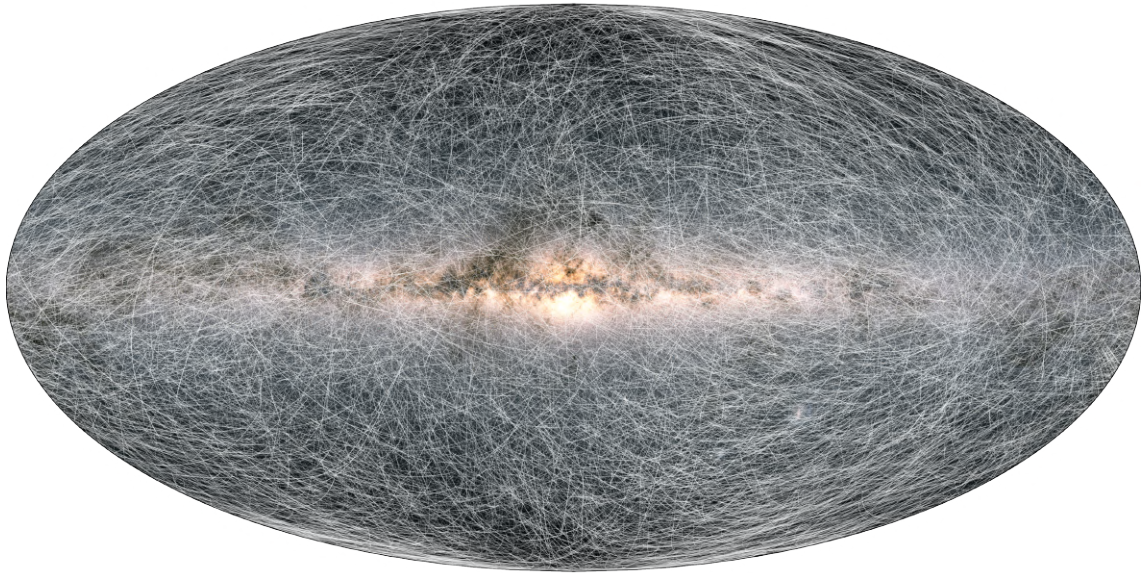
Figure 4.4: Superposed to the image of the Milky Way there are trails that represent the trajectory of 40000 stars within 100 pc. Their proper motions are measured by Gaia satellite and catalogued in the EDR3. Credits: ESA/Gaia/DPAC; CC BY-SA 3.0 IGO. Acknowledgement: A. Brown, S. Jordan, T. Roegiers, X. Luri, E. Masana, T. Prusti and A. Moitinho.

4.3 Comparison of our work with Gaia data.

Our goal is to select among the models given in Section 3.4 the one that better depicts the Solar neighbourhood to have a realistic representation for subsequent dynamical calculations. We searched for the latest studies of the Solar System neighbourhood population and found the article of Reylé, C. et al. 2021 in which the authors make a catalogue of stars enclosed in a 10 pc distance from the Sun.

The stars of this catalogue were selected using SIMBAD[2], an astronomical database for objects that don't belong to the Solar System. The selection criterion for SIMBAD query was that the maximum object parallax should have been of 100 mas that translates in a maximum distance of 10 pc basing on the parallax relation $a[\text{as}] = \frac{1[\text{AU}]}{D_{obj}[\text{pc}]}$.

Data obtained by authors have been checked and updated using the latest EDR3 Gaia values and collected in a 559 objects catalogue that spans from the most luminous A-class stars to exoplanets with highlights on the system type (single star or multiple) and the spectral type distribution.

The full catalogue is available at https://gucds.inaf.it/GCNS/The10pcSample/ in which for each star several information were given as:

- System name;

- Category;

- Position in right ascension and declination coordinates;

- Epoch;

- Parallax;

- Radial velocity;

- Spectral type;

- Photometric data;

- Identifiers.

4.3.1 Spectral type - Mass conversion.

Our models state the number of stars by volume unit for a given mass M while the catalogue only gives information on spectral type of stars. To compare models and catalogue data is thus firstly

---

2. Set of Identifications, Measurements, and Bibliography for Astronomical Data

necessary to convert data from spectral type to mass. To do this we used the table given by Pecaut and Mamajek 2013 last updated on 02/03/2021 and available at the website http://www.pas.rochester.edu/. In Figure 4.5 is shown the conversions from spectral type to mass and specific values for each spectral type are shown in Table 4.1.
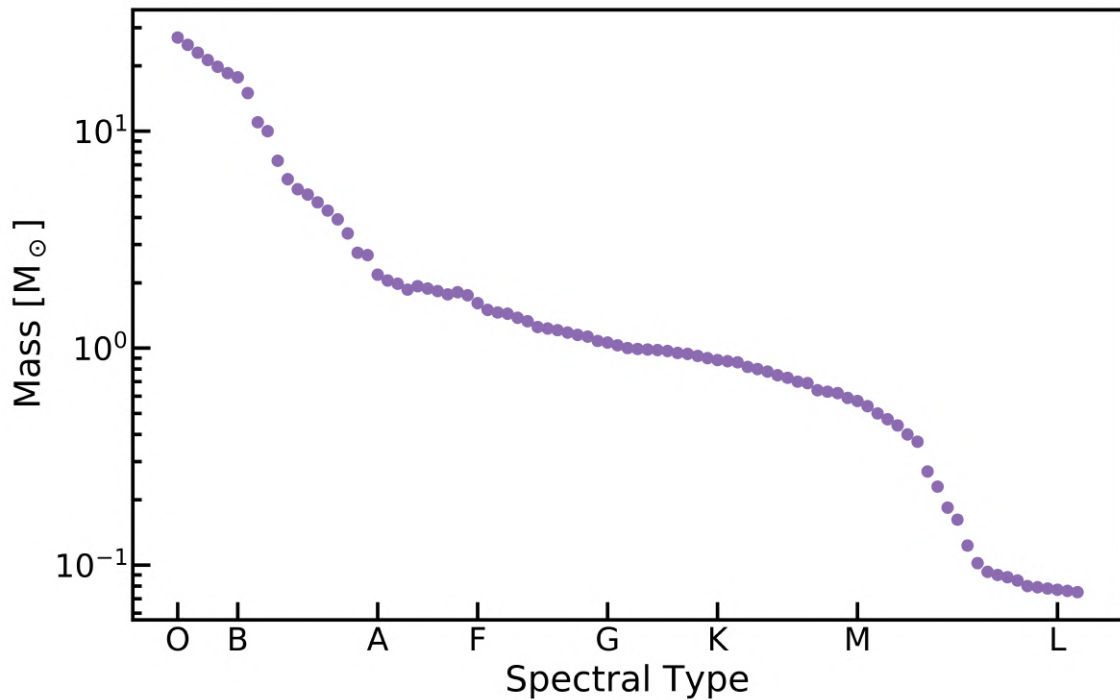
Figure 4.5: Spectral type - Mass conversion. In this plot each point links the spectral type to the mass given in Pecaut and Mamajek 2013. The points between spectral types correspond to sub-spectral classes that usually range from 0 to 9.

This conversion relation is truncated at L2 spectral class because for lower masses the main sequence overlaps the Hayashi track thus the objects are fully convective and is difficult to have a proper mass-luminosity relation. The Hayashi track is an almost vertical curve that splits the HR diagram into an hydrostatic equilibrium zone and a non-hydrostatic equilibrium zone. Active stars belong to the first zone while forming stars belong to the latter zone. Pre-Main Sequence stars stand on the Hayashi track and are characterized by full convection. When the PMS star on the Hayashi track develops a radiative core and increases its mass and temperature it leaves the track towards the hydrostatic equilibrium zone stopping on the Main Sequence in which the star will begin hydrogen burning. The Hayashi track sets a limit in the HR diagram to stellar evolution: all the evolution takes place in the hydrostatic equilibrium zone in which the star structure can be radiative, while the more it's near to Hayashi track, the more its structure becomes convective. An example of the role of the Hayashi track can be taken from data in Reylé, C. et al. 2021 in

Figure 4.6 where a Color-Magnitude Diagram, CMD, is plotted using BP, RP, and G photometric filters from Gaia telescope. In this Figure is clearly visible the main sequence and the white dwarfs sequence while for low G magnitudes (>16) the main sequence presents a tilt corresponding to the presence of the Hayashi track. These low mass objects stand on the Hayashi track, thus are fully convective and the usual set of equation for stellar structures doesn't work. This cause some difficulty in the determination of a mass-luminosity relation and bigger uncertainties in the mass estimate.

Spectral Class	Mass [$M_\odot$]	Spectral Class	Mass [$M_\odot$]	Spectral Class	Mass [$M_\odot$]
O7	27	F1	1.5	K5	0.7
O7.5	25	F2	1.46	K6	0.69
O8	23	F3	1.44	K7	0.64
O8.5	21.3	F4	1.38	K7.5e	0.63
O9	19.8	F5	1.33	K8	0.62
O9.5	18.5	F6	1.25	K9	0.59
B0	17.7	F6.5	1.23	M0	0.57
B0.5	15	F7	1.21	M0.5	0.54
B1	11	F8	1.18	M1	0.5
B1.5	10	F8.5	1.15	M1.5	0.47
B2	7.3	F9	1.13	M2	0.44
B2.5	6	F9.5	1.08	M2.5	0.4
B3	5.4	G0	1.06	M3	0.37
B4	5.1	G1	1.03	M3.5	0.27
B5	4.7	G2	1	M4	0.23
B6	4.3	G3	0.99	M4.5	0.184
B7	3.92	G4	0.985	M5	0.162
B8	3.38	G5	0.98	M5.5	0.123
B9	2.75	G6	0.97	M6	0.102
B9.5	2.68	G7	0.95	M6.5	0.093
A0	2.18	G8	0.94	M7	0.09
A1	2.05	G8.5	0.92	M7.5	0.088
A2	1.98	G9	0.9	M8	0.085
A3	1.86	K0	0.88	M8.5	0.08
A4	1.93	K0.5	0.87	M9	0.079
A5	1.88	K1	0.86	M9.5	0.078
A6	1.83	K2	0.82	L0	0.077
A7	1.77	K2.5	0.8	L1	0.076
A8	1.81	K3	0.78	L2	0.075
A9	1.75	K3.5	0.75		
F0	1.61	K4	0.73		

Table 4.1: Extract of the Pecaut and Mamajek 2013 table available at this link containing only Spectral Class and Mass columns. This Table is represented in Figure 4.5.
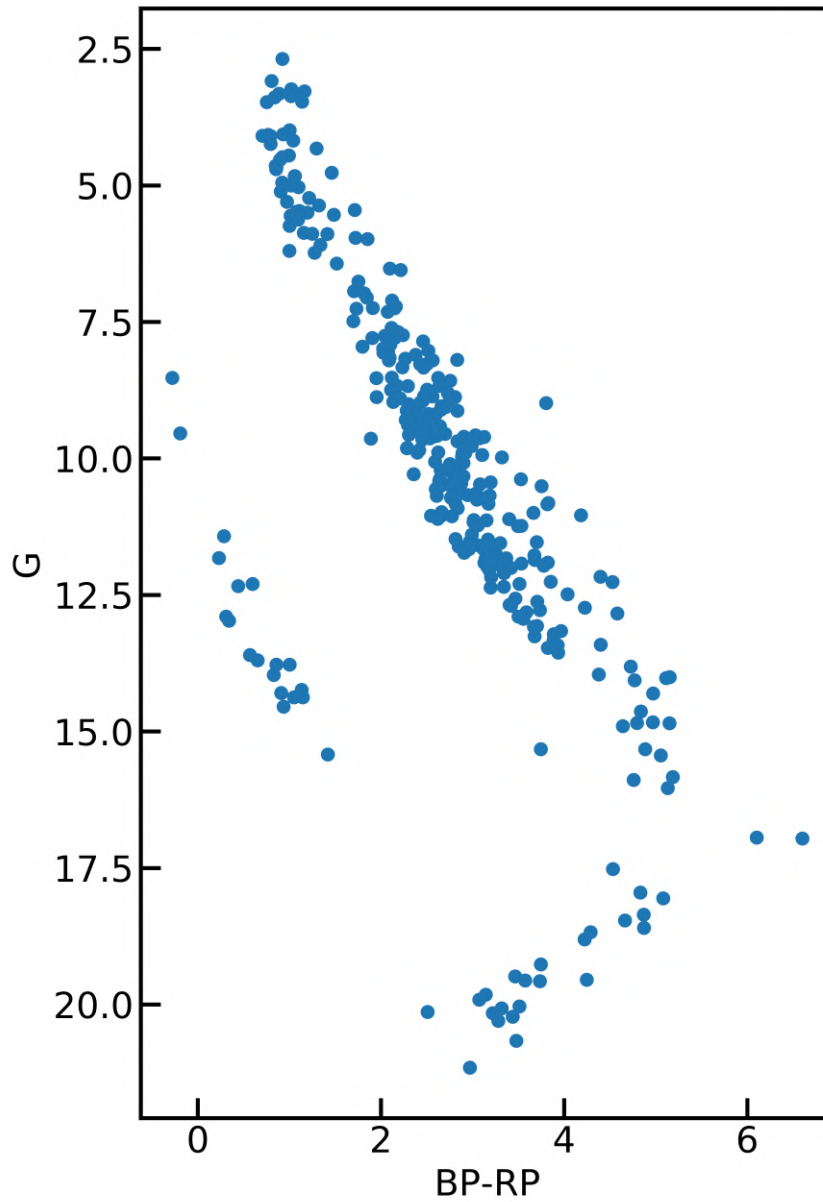
Figure 4.6: Color magnitude diagram for stars in the Reylé, C. et al. 2021 catalogue using Gaia photometric filters G, BP, and RP.

4.3.2   Comparison between data and models.

Since some stars of the catalogue don't have spectral type classification we ignored them for our comparison keeping only the ones with known spectral type. The 'new' catalogue has then *321* stars, *99* brown dwarfs, *77* planets, and *21* white dwarfs for a total of *518* objects and can be represented by the radar chart 4.7. In order to compare our model to data we integrated each PDMF in a spherical volume of *10* pc radius and translated data from spectral type to mass bins as described in the previous subsection. The white dwarfs number is calculated as explained in 3.5.1 for the volume integrated PDMFs.

As a first check on this dataset it is possible to estimate the stellar mass density in this *10* pc radius volume. We can thus compare the Gaia dataset density with the mean density of the disk calculated as shown in Section 2.4. Using as reference Table 4.1 we can sum up all the dataset masses. Since the Table stops at L2 spectral type we assumed a mean mass $\langle M_{BD} \rangle = $ *0.07* $M_\odot$ for brown dwarfs, and a mean mass $\langle M_{pl} \rangle = $ *0.001* $M_\odot$ for planets obtaining the results shown in Table 4.2. The mean density of the chosen model seem to agree well to the mean density calculated from the dataset. If we compare the two values we get that our model's predicted mean density can be considered convincing in an accuracy range of $\frac{|D-M|}{D} = $ *6.1*% thus validating the chosen value for the Oort surface density.

	Total Mass $[M_\odot]$	Mean density $[M_\odot \mathrm{pc}^{-3}]$
Gaia dataset	140	0.033
Our models (2.4)	134	0.032

Table 4.2: Comparison between total mass of Gaia dataset and our model prediction for total mass in a *10* pc radius sphere and density. Model mean density is calculated as (2.13).
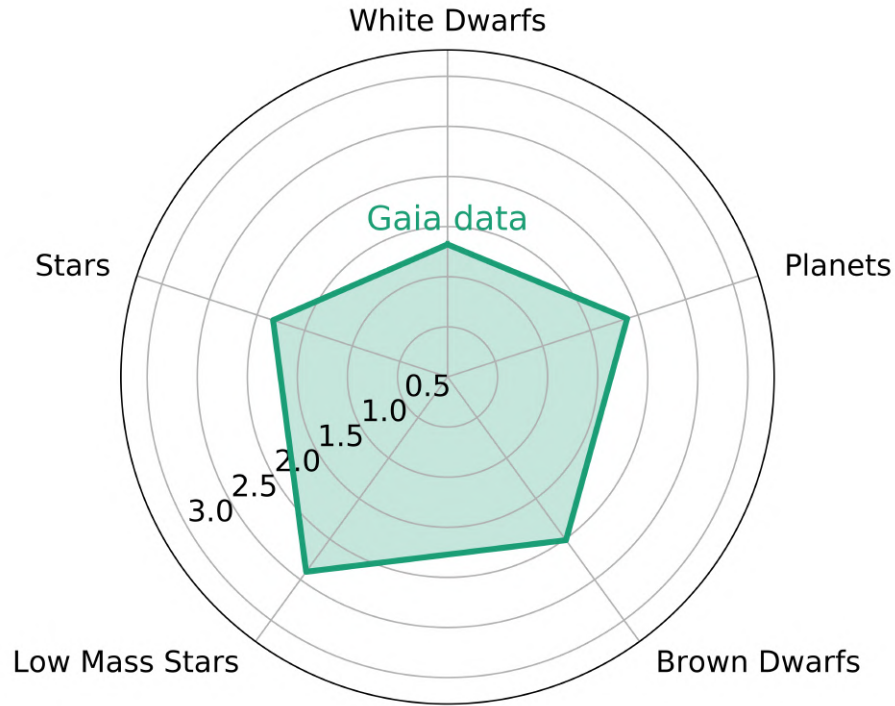
Figure 4.7: Logarithmic radar chart representing Gaia data given by Reylé, C. et al. 2021 listed in Table 4.3.

Comparison by object category. One possible classification given by authors is by object category:

- Stars - from spectral class A to spectral class K;

- Low mass stars - spectral class M;

- Brown dwarfs - spectral classes L,T,Y;

- Planets;

- White dwarfs.

We then firstly compared the amount of objects in each category with our model. We integrated the PDMF distributions in the mass intervals shown in Table 4.3 in order to compare the models to data. The results of this integration are shown in Figures 4.8, 4.9, and 4.10, 4.11 where PDMFs calculated using same SFR and Gaia data are plotted superposed in logarithmic scale.

As can be seen from plots, PDMFs using Salpeter-type IMF seem to overestimate the number of objects in brown dwarfs and low mass category while stars, planets, and white dwarfs are under-estimate. Miller and Scalo IMF based PDMFs instead have a huge overestimate (~ 3 dex) in the

Object category	Mass range [M$_\odot$]	Spectral type	Number of objects in catalogue
Stars	[0.59-2.18]	A to K	68
Low Mass	[0.078-0.57]	M	253
Brown Dwarfs	[0.013-0.077]	L, T, Y	99
Planets	[0.001-0.013]		77
White Dwarfs			21

Table 4.3: This table associates to object category given by Reylé, C. et al. 2021 the spectral type, the mass range calculate as in Subsection 4.3.1, and the relative object count for the catalogue.
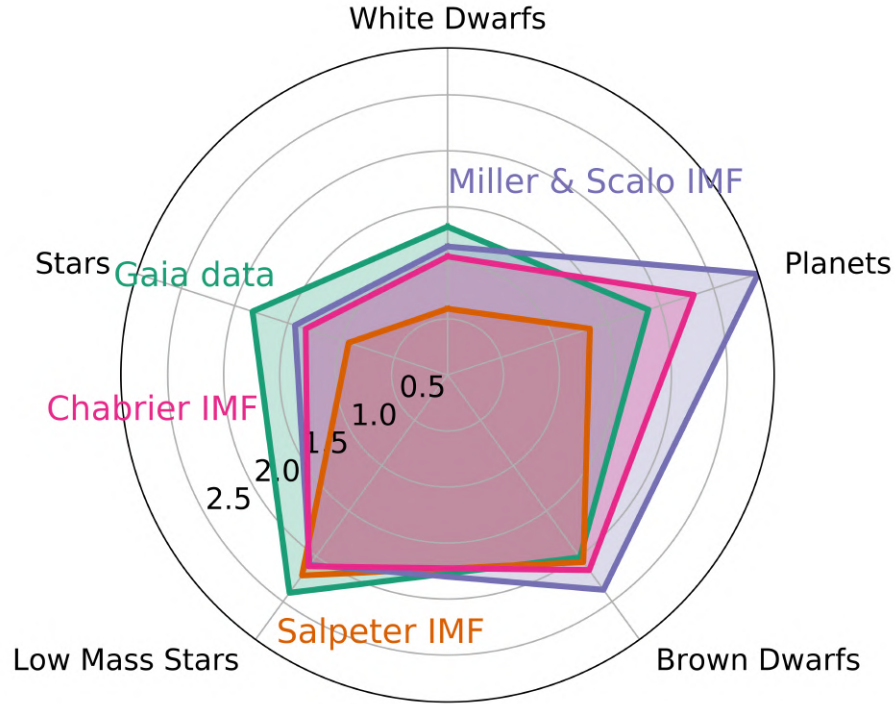
Figure 4.8: Logarithmic radar chart representing PDMFs using constant SFR integration results for different IMFs used superposed to Gaia data.

planet category while there seems to be agreement in low mass and stars category. PDMFs calculated using Chabrier IMF also overestimate the planet and brown dwarfs domain while for low mass, stars, and white dwarfs there seems to be agreement with data. Considering the different SFRs used, there isn't an significant variation on the number of objects calculated but observing the charts, we can see that PDMFs using constant SFR or Levy SFR have counts similar to Gaia data for stars, low mass stars, and white dwarfs. As we disclosed in the previous Section, there is the possibility that the Gaia dataset is incomplete, especially for low mass objects as brown dwarfs, planets, and white dwarf that are more difficult to observe.
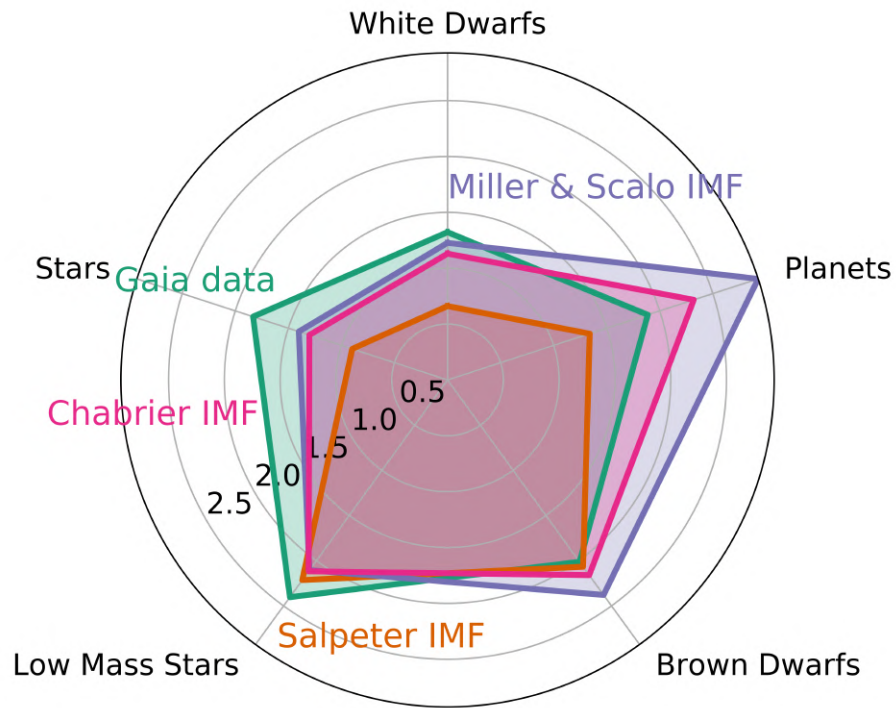
Figure 4.9: Logarithmic radar chart representing the 3 different PDMFs calculated using Schmidt $n = 1$ SFR and integrated in the mass intervals and superposed to Gaia data.
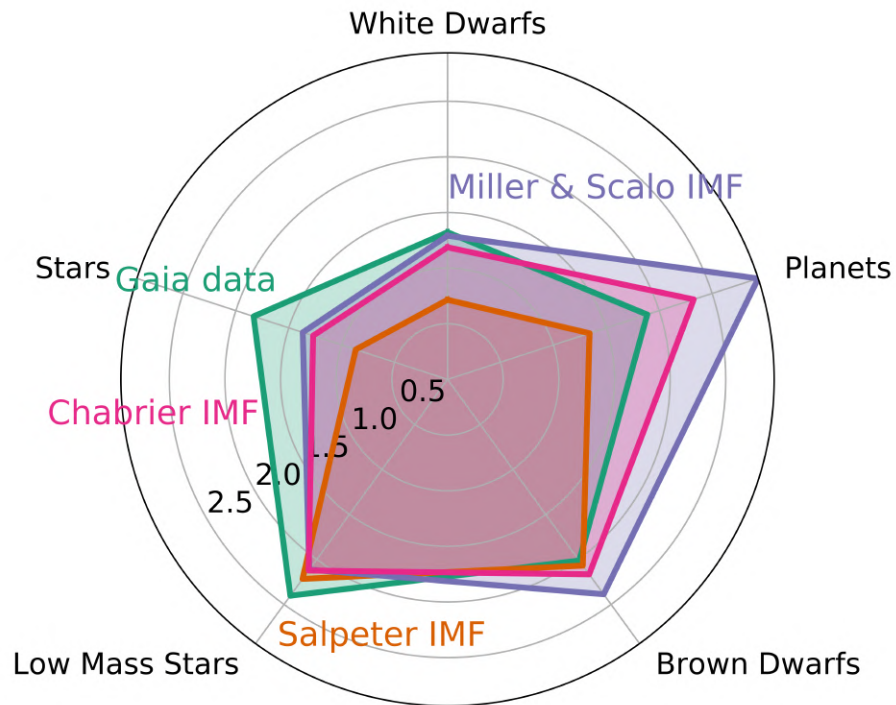
Figure 4.10: Radar chart showing 3 different PDMFs calculated with Schmidt $n = 2$ SFR superposed to Gaia data in logarithmic scale.
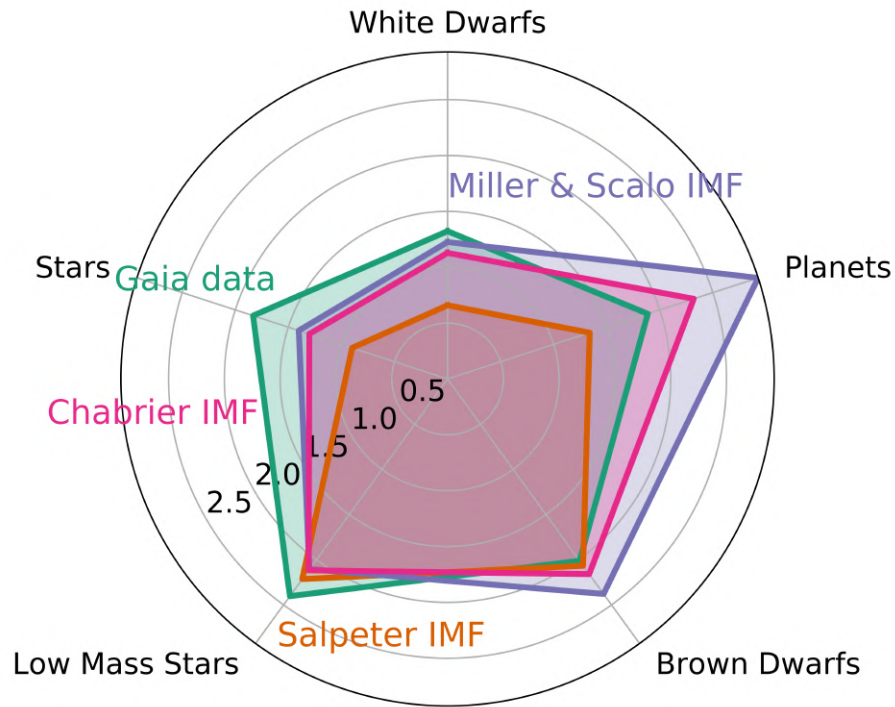
Figure 4.11: Radar chart in logarithmic scale showing the 3 different PDMFs using Levy SFR integrated in the mass interval and superposed to Gaia data.

Comparison by spectral type classification. Another approach we used to compare our models to data is to rebin data every two mass bins in order to have more than one count for bin, obtaining a total of *24* bins. We integrated our model in the same mass bins and plotted the results in Figures 4.12, 4.13, and 4.14. All the PDMF models give an acceptable estimate over the mass range $[0.1-1]$ $M_\odot$ while they all underestimate the stars count at higher masses, constant SFR and Levy SFR gives less underestimate than Schmidt ones. As in already noticed PDMFs using Miller and Scalo IMF are the ones that maximum overestimate the quantity of stars at low masses and also Chabrier IMF causes an overestimate in the low mass range. PDMFs using Salpeter-type IMF 4.12 show instead better agreement in the low mass range.

To establish which model best fitted data we performed the Kolmogorov-Smirnov Test with the results tabulated in 4.4. According to these results and setting the limit for the p-value as *0.05*, we conclude that we can't reject any of the models proposed. In Chapter 7 we will although simplify our calculations by taking the Salpeter type PMDF computed with constant SFR and we will define a lower and upper boundary by taking the minimum and maximum PDMF model.
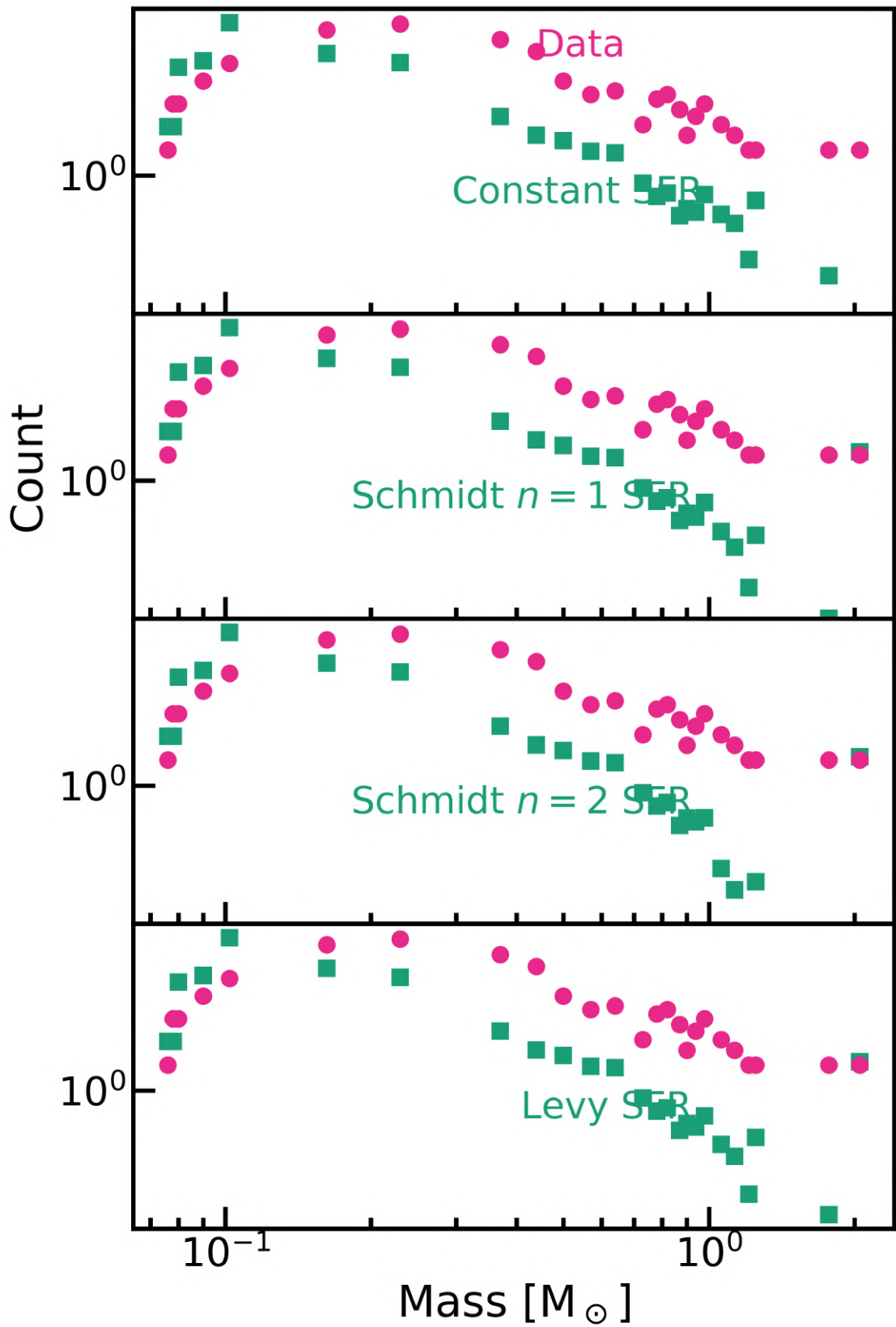
Figure 4.12: In these plots data and model are represented. Data is plotted with pink colours and dot markers while model is plotted with green colours and square markers. The PDMF models shown are the ones using Salpeter-type IMF and a different plot is given for each SFR considered.
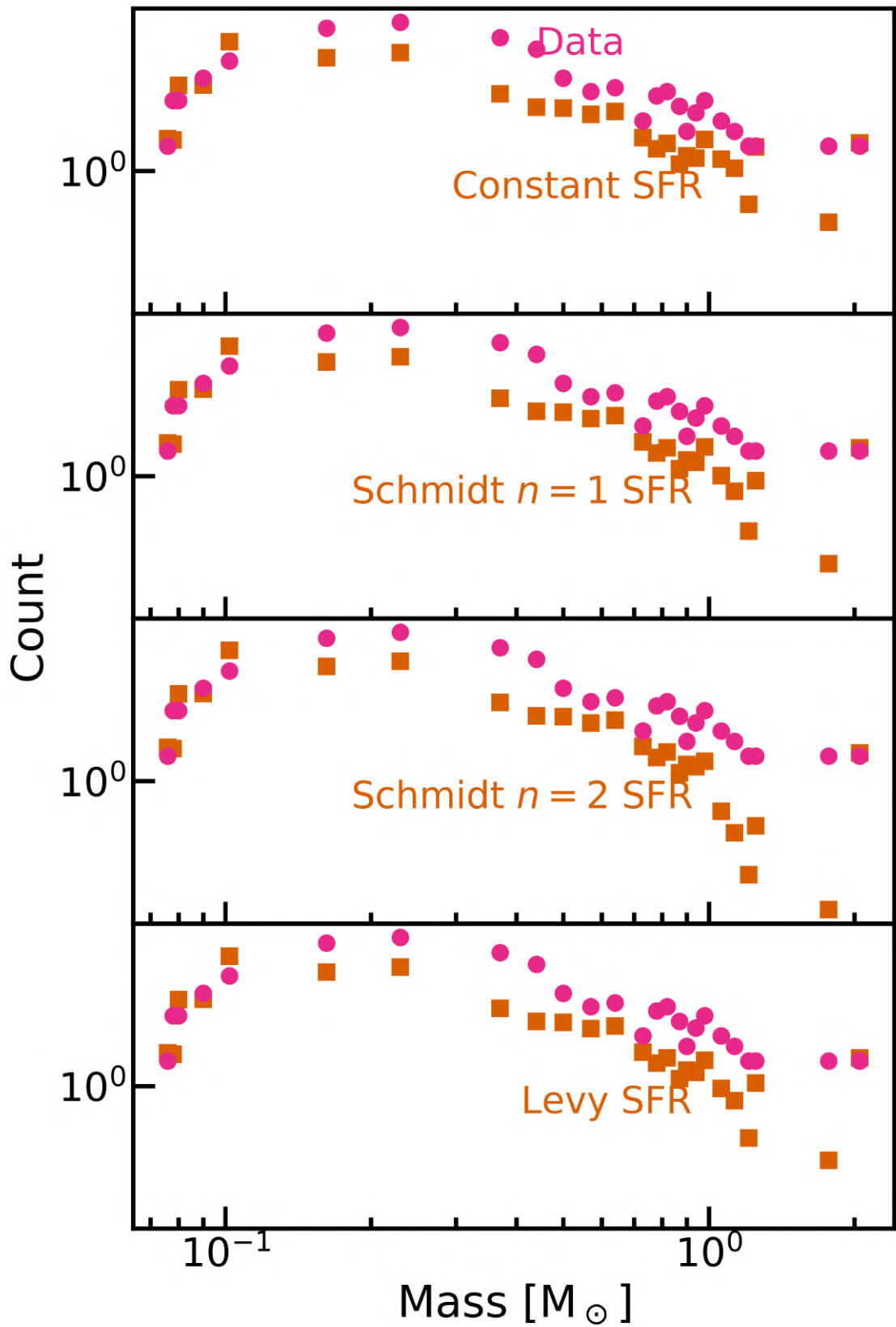
Figure 4.13: Data is plotted using pink colour and dot markers while model is represented with orange colour and square markers. The PDMF models shown are the ones using Miller and Scalo IMF and a different plot is given for each SFR considered.
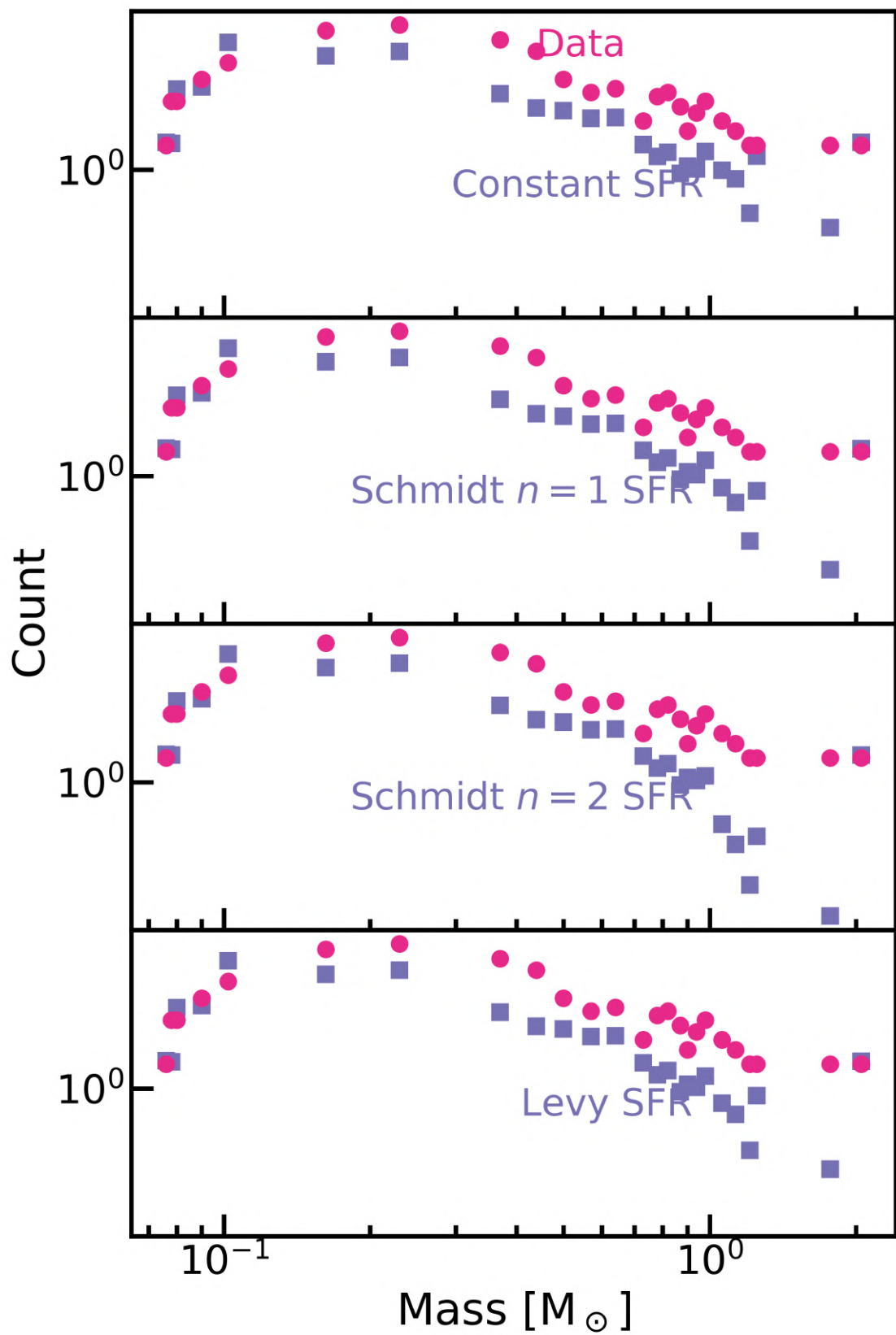
Figure 4.14: Data is plotted with pink colours and dot markers while model is plotted using green colours and square markers. The PDMF models shown use Chabrier IMF and a different plot is given for each SFR considered.

$\xi(M)$	$\varphi(t)$	p-value
Salpeter-type IMF	Constant SFR	0.00010
	Schmidt $n = 1$ SFR	0.00041
	Schmidt $n = 2$ SFR	0.00041
	Levy SFR	0.00041
Miller & Scalo IMF	Constant SFR	0.012
	Schmidt $n = 1$ SFR	0.012
	Schmidt $n = 2$ SFR	0.012
	Levy SFR	0.012
Chabrier IMF	Constant SFR	0.012
	Schmidt $n = 1$ SFR	0.012
	Schmidt $n = 2$ SFR	0.012
	Levy SFR	0.012

Table 4.4: Results of the Kolmogorov-Smirnov test for our PDMFs models. All the models show $p < 0.05$.

Chapter 5

Kinematics

5.1 Introduction

In this Chapter is discussed local kinematics of stars starting from a brief outline on the history of kinematic studies in Section 5.2.

In Section 5.3 we will discuss about the keplerian approach to the calculation of the rotation curve.

In Section 5.4 we will show the Oort constants and the quantities which can be derived by them. We will also show the rotation curve calculated integrating our profile density model and compare its results with up to date Oort constants values. The rotation curve will be used to determine the Galaxy mass at the Sun position and thus determine the Hill radius value for Star-Galaxy interaction in Chapter 6.

In Section 5.5 we will then define the Local Standard of Rest and get the local stellar mean velocity by averaging over the results of some chosen authors. This result will be employed in Chapter 7 along with the results of the PDMF integration to calculate the duration and frequency of stellar interaction with the Sun.

5.2 Setting the context

At the beginning of the 20th century there wasn't a common approved theory about Galaxy rotation but some astronomer were approaching this issue. Lindblad is one of the first that thought our Galaxy doesn't has a solid body rotation but instead that rotation should be different along the radial distance from the Galactic centre (Lindblad 1925). Lindblad suggested also that the

Galactic system should be in dynamical equilibrium and divided into subsystems rotating around the central symmetry axis of the Galaxy.

Dividing the Galaxy into components means that various subsystems could have different velocities thus being an useful description for the observed high stellar velocities that were out of the mean velocity observed at that time (according to Lindblad's hypothesis these high velocity stars should orbit nearer to Galaxy's centre).

5.3 Rotation Curve

The kinematics of stars in Galaxies is studied since the beginning of 1900. The first observations of the rotation of galactic disks were uncertain due to the lack of precision and sensitivity of instruments back then. Methods of rotation velocity calculation included observation of single stars using photographic plates or spectroscopy in the visible wavelength range. In the work of van Maanen 1916 the author infers a rotation for M101 galaxy from the observation of about 20 single stars in 87 different points of the galaxy with a total observation time of almost 24 hours, of course this method was the less accurate because is very difficult to observe resolved stars and their motion in outer galaxies. The spectroscopic method consisted in the observation of optical emission of HII gas. One of the first astronomers that made this kind of observations was Pease that from 1915 started to calculate the rotational velocities for different disk galaxies from absorption lines as in Pease 1916 where the author calculates the rotation curve for NGC4594 galaxy using 80 hours of observation and obtaining a rotation curve decreasing with the distance from the nucleus that fitted with a linear law. Further on another contribution to the calculation of rotation curves for disk galaxies was given by Babcock which in 1939 calculated the rotation curve and mass for Andromeda galaxy (Babcock 1939). Babcock used spectroscopic observations as Pease and from the rotation curve inferred, using newtonian physics, a mass of $1.02 \cdot 10^{11}$ $M_\odot$.

Rotation curves once were made only for inner regions of galaxies because telescopes only worked in the visible wavelength range so the observations could only map the presence of stars. With the beginning of radio observation from 1940 the astronomers have been able to add points for outer zones thanks to the observation of 21 cm emission from HI clouds that extend much more than stars in the galaxy. A big step forward into the characterization of kinematics and mass of disk galaxies was made by Vera Rubin with her work in 1970-1980 (e.g. in Rubin, Ford, and Thonnard 1980) where the presence of dark matter in the outer zones of the galaxies was evidenced by rotation curves as in Figure 5.1. The observed rotation curves were thus showing an almost constant velocity for increasing distance from the galactic centre while from a keplerian point of view ve-
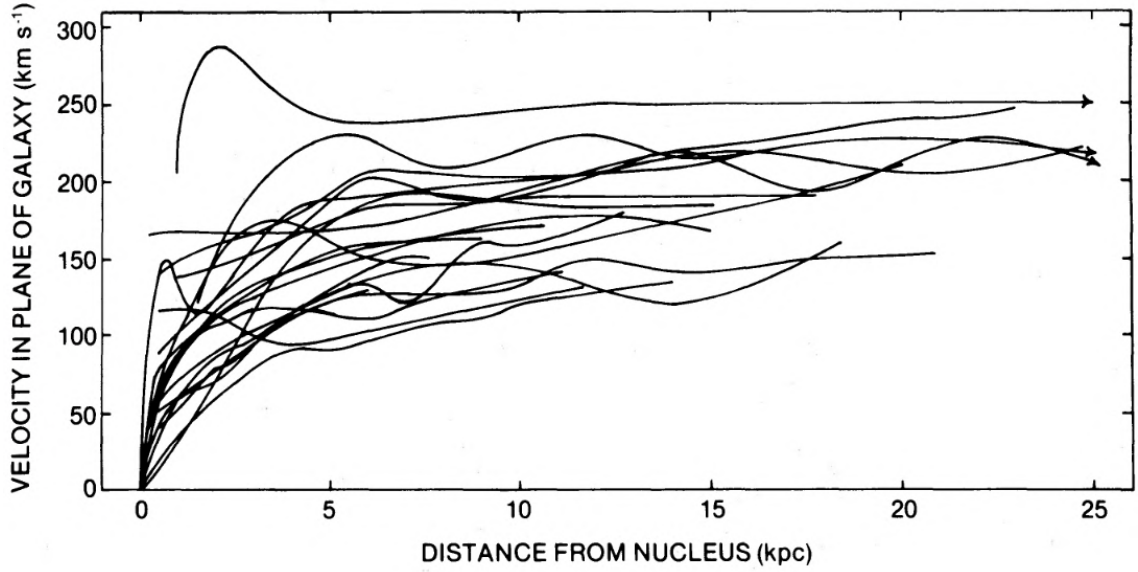
Figure 5.1: This plot represents the rotation curves for 21 disk galaxies taken from the work of Rubin, Ford, and Thonnard 1980.

locity should decrease as $r^{-1/2}$. Actually, the observations made by Rubin and her colleagues were still too near to the centre of galaxies to evidence the presence of dark matter but paved the way to further investigations about this topic.

The rotation curve can thus be well approximated by keplerian theory in the first $20 - 30$ kpc from centre. From Kepler's third law:

$$M = \frac{RV^2}{G} \quad , \tag{5.1}$$

we can extrapolate velocity to get the shape of the rotation curve:

$$V = \sqrt{\frac{GM}{R}} \quad . \tag{5.2}$$

If we assume a density profile we can substitute the mass and calculate the rotation curve:

$$M = 4\pi \int_0^R \int_0^Z \rho(r, z) r dr dz \tag{5.3}$$

where 0 is the galactic centre position, r is the distance from the galactic centre, and z is the height on the Galactic plane. Our goal was to calculate the rotation curve starting from the density profile described in Sect. 2.4 and compare the value of the rotation velocity with the one found by observations (described in the next section). In this way we can check if the calculated Galaxy mass profile is reliable. We used thus integrated the density profile (2.5). We didn't assume a bulge profile since but we simply added the bulge mass value $M_{bulge} = 8.9 \cdot 10^9$ $M_\odot$ taken from
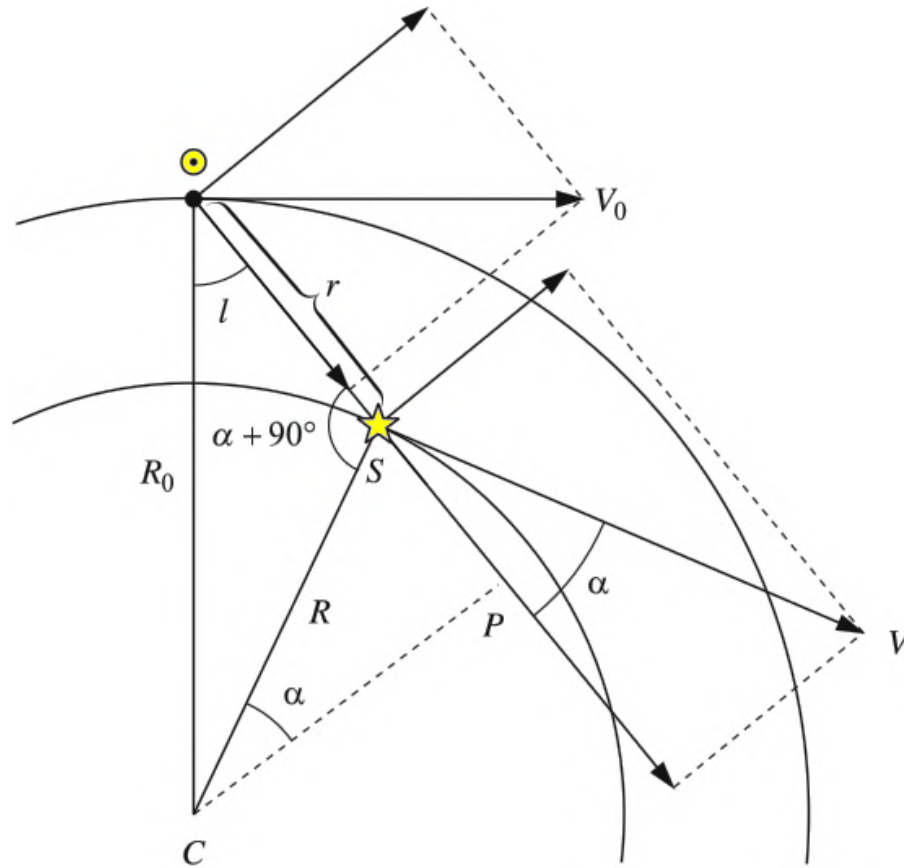
Figure 5.2: Sketch of the objects involved in the calculations for the differential rotation. The subscript o indicate Sun related sizes. Credits: *Fundamental Astronomy* 2007.

McMillan 2016. The results of this integration are shown in the next section, compared to the values given by Oort constants observation.

5.4 Oort Constants

Stars and gas clouds in disk galaxies have a differential rotation, that is, the system doesn't rotate like a rigid body but instead velocity depends on the distance from the galaxy centre. We can model this taking into account the scheme of velocities shown in Figure 5.2 where the motion of a star S from a distance R from Galaxy centre and the motion of the Sun at a distance R_o are pictured. We can split the relative velocity, $v = V_o - V$, into radial, v_r, and tangential, v_t, velocity

and write them as:

$$v_r = V \cos \alpha - V_o \sin l \qquad (5.4)$$

$$v_t = V \sin \alpha - V_o \cos l \qquad (5.5)$$

where V is the velocity of the star S, V_o is the velocity of the Sun (both with respect to the Galaxy centre), α is the angle between the velocity vector of the star S and the line of sight, and l is the galactic longitude. If we take ω as the angular velocity:

$$\omega = \frac{V}{R} \qquad (5.6)$$

ans use trigonometry we can re-write the components of relative velocity as follows:

$$v_r = R_o(\omega - \omega_o) \sin l \qquad (5.7)$$

$$v_t = R_o(\omega - \omega_o) \cos l - \omega r \qquad (5.8)$$

where ω_o is the angular velocity of the Sun and r is the distance between the Sun and the star S. Measuring the two components of the velocity V gives the angular velocity value, the distance r, and the distance R from the centre. The problem in using this method is the presence of gas clouds and dust that cause extinction and make difficult to observe stars at large distances.

For stars in the Solar neighbourhood is possible to introduce the Oort constants, found by Jan Oort in 1927 (Oort 1927b). If we take into account that near the Sun the distance Sun-S is negligible with respect to the distance R_o, thus $r \ll R_o$, we can expand $(\omega - \omega_o)$ in Taylor series to the first term:

$$\omega - \omega_o = \left(\frac{d\omega}{dR}\right)_{R=R_o} + \ldots \qquad (5.9)$$

Substituting this expression into (5.7) and (5.8) and substituting the angular velocity we get:

$$v_r \approx \left[\frac{V_o}{R_o} - \left(\frac{dV}{dR}\right)_{R=R_o}\right] r \cos l \sin l \approx A r \sin(2l) \qquad (5.10)$$

$$v_t \approx \left[\frac{V_o}{R_o} - \left(\frac{dV}{dR}\right)_{R=R_o}\right] r \cos^2 l - \omega_o r \approx A r \cos(2l) + B r \qquad (5.11)$$

where the two Oort constants were introduced:

$$A = \left[\frac{V_o}{R_o} - \left(\frac{dV}{dR}\right)_{R=R_o}\right] \qquad (5.12)$$

$$B = -\frac{1}{2}\left[\frac{V_o}{R_o} + \left(\frac{dV}{dR}\right)_{R=R_o}\right] \qquad (5.13)$$
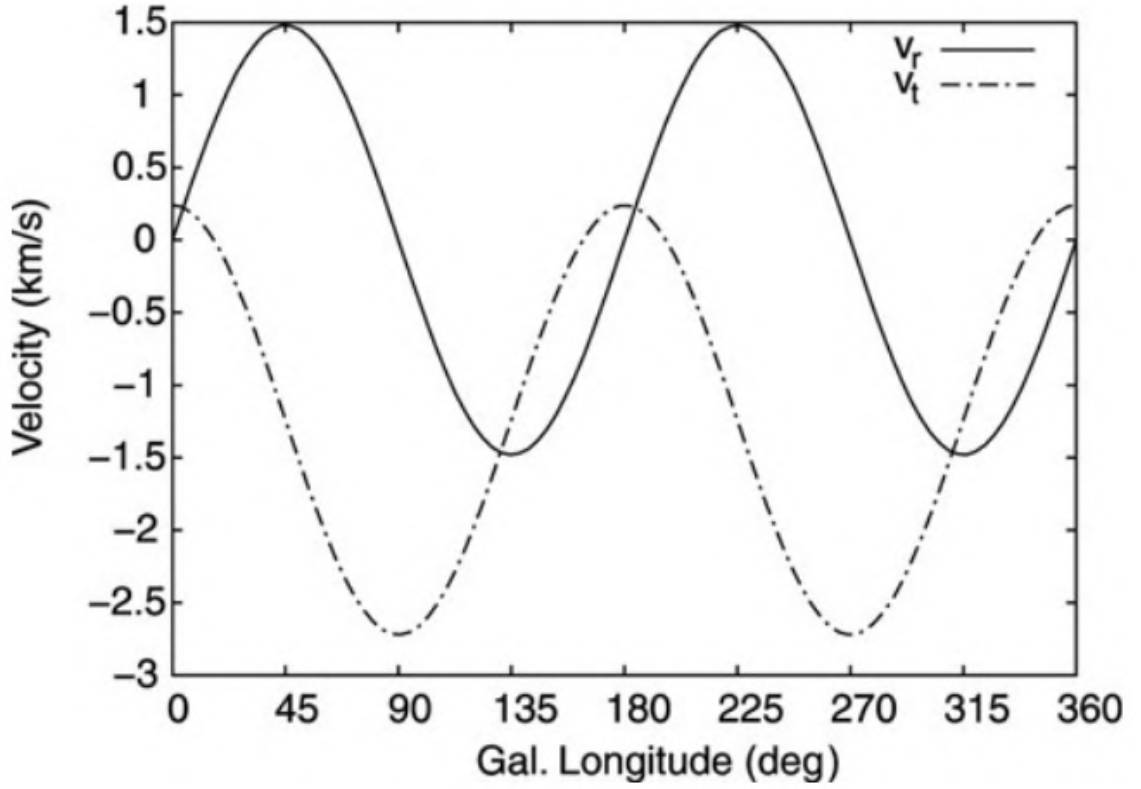
Figure 5.3: In this plot are represented (5.10) and (5.11) functions in which, from the amplitudes, is possible to obtain the Oort constants A and B from observations. Credits: Schneider 2015

The constants A and B have dimensions of $\left[\frac{\mathrm{km\,s}^{-1}}{\mathrm{kpc}}\right]$ and can be used to calculate the Sun's rotational velocity, and local information about kinematics:

$$\omega_o = A - B \tag{5.14}$$

$$\left(\frac{dV}{dR}\right)_{R_o} = -(A + B) \tag{5.15}$$

From observations, we can calculate the Oort constants by interpolating observation with sine and cosine functions (5.10) and (5.11) and looking for the amplitude of these functions as in Figure 5.3. Up to date values for Oort constants can be found in Bobylev and Bajkova 2020 where the authors used Gaia DR2 data for young stars near the Sun (all the stars are at a maximum distance of 500 pc) to calculate and update Oort constants:

$$A = 16.25 \pm 0.33 \text{ km s}^{1} \text{ kpc}^{1} \tag{5.16}$$

$$B = \text{-}12.58 \pm 0.34 \text{ km s}^{1} \text{ kpc}^{1} \tag{5.17}$$

We can now calculate the Sun's rotational velocity (and thus by using (2.2) the circular velocity), and the expected slope for the rotation curve at the Sun's position:

$$\omega_o = A - B = 28.83 \text{ km s}^{-1} \text{ kpc}^{-1} \tag{5.18}$$

$$V(R_\odot) = \frac{\omega}{R} = 263.4 \text{ km s}^{-1} \tag{5.19}$$

$$\left(\frac{dV}{dR}\right)_{R_o} = -(A + B) = -3.67 \text{ km s}^{-1} \text{ kpc}^{-1} \tag{5.20}$$

We integrated eq. (2.5) to get the Mass of the Galaxy at the Sun's position and superposed it to the Milky Way rotation curve calculated by Xin and Zheng 2013 in Figure 5.4. Local values from our model both for the velocity and its derivative are the following:

$$V(R_\odot) = 195.0 \text{ km s}^{-1} \tag{5.21}$$

$$\left(\frac{dV}{dR}\right)_{R_o} = -7.50 \text{ km s}^{-1} \text{ kpc}^{-1} \tag{5.22}$$

these values have an accuracy of $\sim 25\%$ on the velocity value given in (5.19) while the slope of the curve is significantly different from the one given in (5.20). This indicates that our model under-estimates of the total Galaxy mass. This problem could be resolved by assuming an higher value for the Oort surface density 2.4 that should increase the stellar mass budget. Another possible solution could be to add a gas component in the calculation of the density profile or to increase the object quantity in the low mass tail of our IMFs.

5.5 Local Standard of rest

The Local Standard of Rest, LSR, is a reference frame in which velocities of stars in the Solar neighbourhood can be calculated in order to link local measurements to the Galactocentric coordinate system. The use of such a fictitious reference frame is necessary since the Sun is itself moving around the Galaxy thus the velocities measured from Earth are relative to the Sun's motion. The LSR is defined in two different ways: the dynamical LSR is the point instantaneously centred on the Sun that moves in a circular orbit around the Galaxy centre while the kinematic LSR is the point with respect to the average velocity of stars is zero. The two points are nearly situated in the same spatial point, so for our purpose we will refer to the dynamical LSR definition.

To measure velocity in the LSR we need to introduce the LSR velocity, which from the dynamical
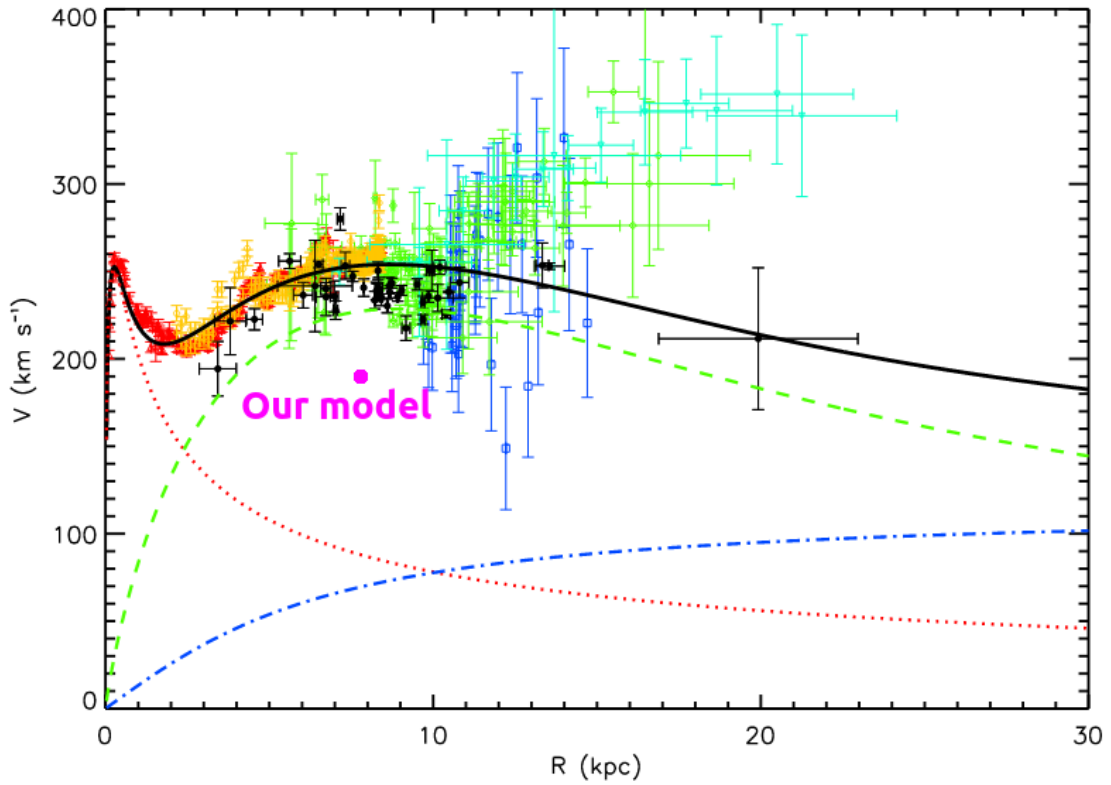
Figure 5.4: Rotation curve from Xin and Zheng 2013 calculated by the authors using maser astrometry. The result of the integration of our model at the Sun's position is superposed to the plot. The red dotted line represents the bulge contribution, dashed green line represents the disk contribution and dash-dotted line the dark matter halo. The points represent different methods of calculations of the rotation curve from different authors: red triangles are from HI- and CO-line tangent velocity method, yellow open circles represent HI tangent velocity method, green diamonds are relative to HII regions measurements, blue squares are C stars, and cyan reverse triangles come from the HI-disk thickness method. Black filled circles come from the authors analysis of masers in HMSFR (High-Mass Star-Forming Regions) data.
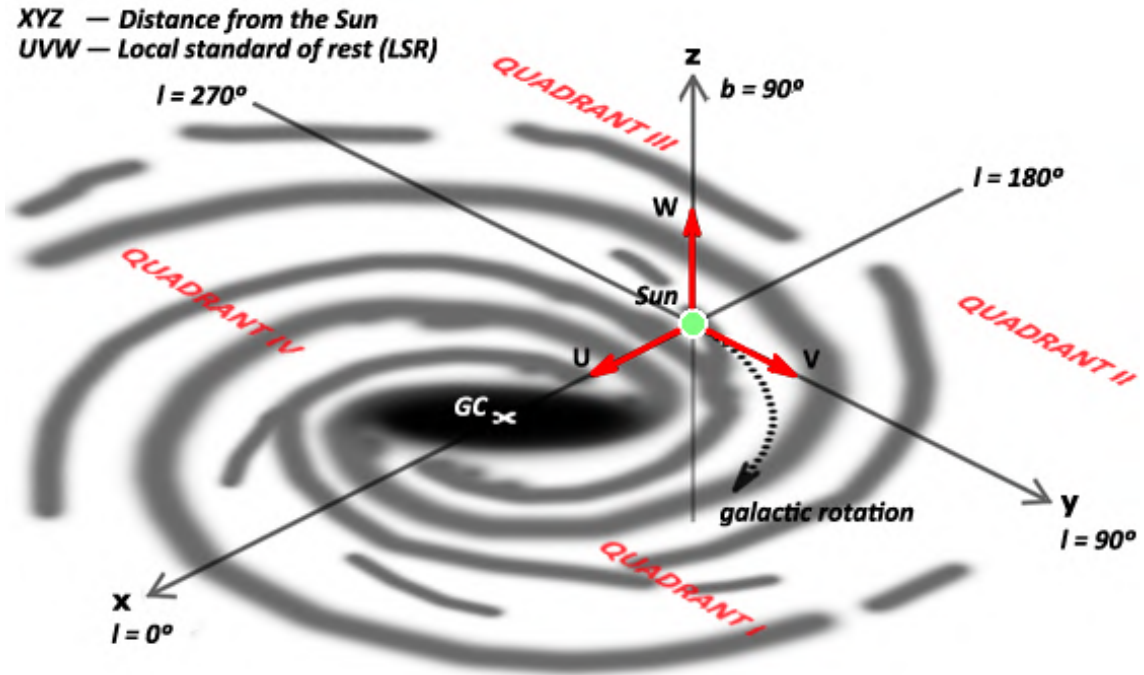
Figure 5.5: Local Standard of Rest reference frame with respect to Galactocentric coordinates. U points to Galaxy centre, V is in the rotation direction, and W is directed perpendicularly to the plane. Credits: https://www.handprint.com/ASTRO/galaxy.html

LSR definition will only have a component in the rotation direction:

$$U_{LSR} = 0 \tag{5.23}$$

$$V_{LSR} = V(R_\odot) \tag{5.24}$$

$$W_{LSR} = 0 \tag{5.25}$$

where $R_\odot$ is the Sun's position in Galactocentric coordinates and in this case is the radius of the circular motion. In this section, velocity components expressed in uppercase are relative to Galactocentric coordinates while if expressed in lowercase are relative to the LSR, as in Figure 5.5. A star having velocity (U, V, W) in Galactocentric coordinates will have a velocity relative to the LSR, (u, v, w) calculated as follows:

$$u = U - U_{LSR} = U \tag{5.26}$$

$$v = V - V_{LSR} \tag{5.27}$$

$$w = W - W_{LSR} = W \tag{5.28}$$

If the Solar peculiar motion is $(u_\odot, v_\odot, w_\odot)$ we can write the relative velocity for a star with respect to the Sun as follows:

$$\Delta u = u - u_\odot \tag{5.29}$$

$$\Delta v = v - v_\odot \tag{5.30}$$

$$\Delta w = w - w_\odot \tag{5.31}$$

To disentangle these relations we need to calculate the Solar peculiar motion by using observations. We make the assumption of symmetry with respect both to rotation axis and plane of the Galaxy and consider a group of stars in the Solar vicinity which can consist of different stellar types as MS stars, Cepheids, OB stars, and so on (an updated Table with the used stellar sample for most recent works can be found in Ding, Zhu, and Liu 2019).

Taking into account the relations 5.29, 5.30, and 5.31, we can calculate the average velocity of the group and get the value of the components of the Solar peculiar motion:

$$u_\odot = \langle u \rangle - \langle \Delta u \rangle = -\langle \Delta u \rangle \tag{5.32}$$

$$v_\odot = \langle v \rangle - \langle \Delta v \rangle \tag{5.33}$$

$$w_\odot = \langle w \rangle - \langle \Delta w \rangle = -\langle \Delta w \rangle \tag{5.34}$$

for the axisymmetric hypothesis the contributions of $\langle u \rangle$ and $\langle w \rangle$ are zero. Since $\langle \Delta u \rangle$, $\langle \Delta v \rangle$, $\langle \Delta w \rangle$ are given by observations, the only value to be calculated is $\langle v \rangle$ which would be null only if all stars would have a circular orbit. It can be possible to deduce a directly proportional relation between $\langle v \rangle$ and the radial velocity dispersion of stars σ_R^2 from statistical reflections on stellar dynamics, as follows:

$$v_\odot = -C\sigma_R^2 - \langle \Delta v \rangle \quad . \tag{5.35}$$

By plotting $\langle \Delta v \rangle$ versus σ_R^2 and extrapolating to $\sigma_R^2 = 0$ we get the value for the $v_\odot$ component. Some recent calculations for the Solar peculiar motion are shown in Table 5.1. The authors cited in the Table use a more complicated relation called Strömberg equation and discussed in Binney and Tremaine 2008:

$$\langle \Delta v \rangle - v_\odot \simeq \frac{\sigma_R^2}{2V_{LSR}} \left[\frac{\sigma_\phi^2}{\sigma_R^2} - 1 - \frac{\partial \ln v\sigma_R^2}{\partial \ln R} - \frac{R}{\sigma_R^2} \frac{\partial (\overline{V_R V_z})}{\partial z} \right] \tag{5.36}$$

where σ_R^2 and σ_ϕ^2 are the dispersion velocities, v is the density distribution of stars, R is the distance form the Galactic centre, and $\overline{V_R V_z}$ is the covariance. This equation however leads to the same approximation as (5.35) for stellar populations that have similar density distributions. Some authors, as Golubov et al. 2013 and later Ding, Zhu, and Liu 2019, have also used a modified Strömberg equation following the idea that stellar populations could not have all the same radial

gradient. Values in Table 5.1 show that the Sun has an orbit which differs from the circular one, it is thus moving toward the Galactic centre, faster than it would be on a circular orbit, and has a component of his motion directed upwards. Once we know the Solar peculiar motion we are able to determine the velocities for stars in the Solar neighbourhood with respect to the LSR, and in particular and their velocity dispersion.

For our forthcoming discussion we choose to take the solar velocity with respect to the LSR as the mean of the velocities given in Table 5.1:

$$u_\odot = 9.57\,\text{km s}^{-1}; \quad v_\odot = 6.96\,\text{km s}^{-1}; \quad w_\odot = 7.46\,\text{km s}^{-1} \tag{5.37}$$

The velocity vector will thus be:

$$\boldsymbol{v} = 14.0\,\text{km s}^{-1}. \tag{5.38}$$

This is the Sun's velocity vector in the LSR and its direction is towards the Solar apex which is a fictitious point that marks direction of the Sun's movement. Together with the Solar apex we can define the Solar antapex which is at the opposite point of the apex. In general, we can assume that the mean peculiar motion of the stars in the LSR has a vector direction that goes from apex to antapex, thus if we take the reference frame on the Sun we will measure the mean velocity (5.38) for stars in the surroundings and their apparent mean motion will be from apex to antapex.

Authors	$u_\odot\,[\text{km s}^{-1}]$	$v_\odot\,[\text{km s}^{-1}]$	$w_\odot\,[\text{km s}^{-1}]$
Dehnen and Binney 1998	10.00	5.25	7.17
Aumer and Binney 2009	9.96	5.25	7.07
Schönrich, Binney, and Dehnen 2010	11.10	12.24	7.25
Golubov et al. 2013	9.96*	3.06	7.07*
Bobylev and Bajkova 2018	8.16	11.19	8.55
Ding, Zhu, and Liu 2019	8.63	4.76	7.26

Table 5.1: In this table some of the principal estimates for the LSR are reported. An extended table of latest values can be found in Ding, Zhu, and Liu 2019.
*These values weren't calculated by authors but have been adopted from Aumer and Binney 2009.

Chapter 6

The Restricted Three-Body problem and its applications.

6.1   Introduction

In this Chapter is described the dynamical interaction between two objects making use of the restricted three body problem theory. In order to apply the solution of the restricted three body problem to our thesis topic we will then, at the end of the Chapter, discuss about the influence of the Galaxy over Solar System and stars in general. The results we will get from this Chapter will be employed in Chapter 7 to evaluate the consequences of interaction between stars and the Solar System.

We will start giving the theory of the restricted three body problem in Section 6.2 and in Section 6.3 we will show the Lagrangian equilibrium points which will be used to define the Hill sphere in the subsequent Section.

In Section 6.4 we will calculate the radius of the Hill sphere and give some values for Sun and stars of different mass.

In Section 6.5 we will give an alternative definition for the gravitational limit of the Sun, the Sphere of Influence, SOI. We will calculate the radius of the SOI for Sun and other stars and compare it to the Hill radius.

Finally, in Section 6.6 we will apply the results of Section 6.4, 6.5 to the local environment and make some consideration upon the possible limits of the Solar System.

6.2   Setting the context: the restricted three-body problem

The three-body problem is a classic dynamical problem and, as the two-body problem, is a special case of the n-body problem. Only the two-body problem has an exact solution while for the other situations numerical methods are required to obtain a solution.

The three-body problem wants to calculate the movement of three point-like masses under the mutual effect of newtonian gravity. If the motion of the masses is described in an inertial reference frame, their motion laws will be:

$$m_1\ddot{\boldsymbol{r}_1} = -Gm_1m_2\frac{\boldsymbol{r_1} - \boldsymbol{r_2}}{|\boldsymbol{r_1} - \boldsymbol{r_2}|^3} - Gm_1m_3\frac{\boldsymbol{r_1} - \boldsymbol{r_3}}{|\boldsymbol{r_1} - \boldsymbol{r_3}|^3} \tag{6.1}$$

$$m_2\ddot{\boldsymbol{r}_2} = -Gm_2m_1\frac{\boldsymbol{r_2} - \boldsymbol{r_1}}{|\boldsymbol{r_2} - \boldsymbol{r_1}|^3} - Gm_2m_3\frac{\boldsymbol{r_2} - \boldsymbol{r_3}}{|\boldsymbol{r_2} - \boldsymbol{r_3}|^3} \tag{6.2}$$

$$m_3\ddot{\boldsymbol{r}_3} = -Gm_3m_1\frac{\boldsymbol{r_3} - \boldsymbol{r_1}}{|\boldsymbol{r_3} - \boldsymbol{r_1}|^3} - Gm_3m_2\frac{\boldsymbol{r_3} - \boldsymbol{r_2}}{|\boldsymbol{r_3} - \boldsymbol{r_2}|^3} \tag{6.3}$$

the trajectories can be computed knowing initial position and velocity of the particles and integrating these three functions. The solution can be integrated numerically as we said earlier there isn't an analytical solution.

In the restricted three-body problem we can consider one of the three particles as a test particle thus having negligible mass. In calculations we can then take e.g. $m_3 \to o$ and use M and m instead of m_1, m_2 for simplicity. We then change the coordinate system and use a reference frame co-rotating with the system, in this way the problem is simplified but we need to take into account the presence of fictitious acceleration like the Coriolis and the centrifugal ones.

The co-rotating reference frame has its centre in the mass centre position of the system:

$$\boldsymbol{r} = \frac{M\boldsymbol{r_1} + m\boldsymbol{r_2}}{M + m} \quad . \tag{6.4}$$

Calling μ the reduced mass:

$$\mu = \frac{Mm}{M + m} \tag{6.5}$$

we can equate the centrifugal force of the system with the gravitational one:

$$\mu\frac{v^2}{R} = G\frac{Mm}{R^2} \tag{6.6}$$
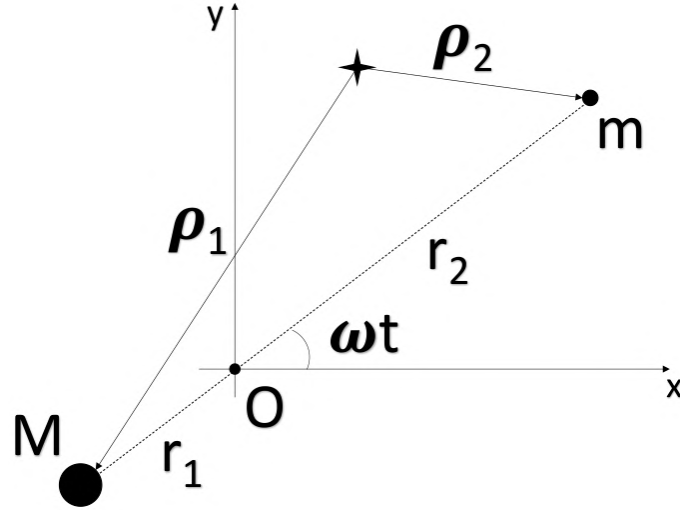
Figure 6.1: Co-rotational reference frame for the restricted three-body problem. Credits: Marco Monaci.

where v is the theoretical velocity of the mass μ and $R = r_1 + r_2$. Since the period for this orbit is $T = \frac{2\pi R}{v}$ we can calculate the angular velocity of the rotating system as follows:

$$\omega = \frac{2\pi}{T} = \sqrt{G\frac{M+m}{R^3}} \quad .\tag{6.7}$$

From the definition of centre of mass ans R we can define the parameter α by solving the following system:

$$\begin{cases} r_1 M = r_2 M \\ r_1 + r_2 = R \end{cases}\tag{6.8}$$

$$\alpha = \frac{m}{M+m}\tag{6.9}$$

Adding the two fictitious accelerations discussed previously, centrifugal and Coriolis accelerations, needed for a non inertial reference frame, we get:

$$\boldsymbol{a} + 2\boldsymbol{\omega} \times \boldsymbol{v} + \boldsymbol{\omega} \times (\boldsymbol{\omega} \times \boldsymbol{r}) = -\frac{M}{r_1^3}\boldsymbol{r_1} - \frac{m}{r_2^3}\boldsymbol{r_2}\tag{6.10}$$

where $\boldsymbol{r}$ is the position, $\boldsymbol{v}$ is the velocity vector, $\boldsymbol{a}$ is the acceleration vector, $\boldsymbol{\omega} \times \boldsymbol{v}$ is the Coriolis acceleration, and $\boldsymbol{\omega} \times (\boldsymbol{\omega} \times \boldsymbol{r})$ is the centrifugal acceleration.

We then can write the motion equations for the reduced three-body problem in the three spatial

directions basing on equation (6.10):

$$
\begin{cases}
\ddot{x} = -\frac{GM(x+\alpha R)}{\rho_1^3} - \frac{Gm(x-(1-\alpha))R}{\rho_2^3} + \omega^2 x + 2\omega\dot{y} \\
\ddot{y} = -\frac{GMy}{\rho_1^3} - \frac{Gmy}{\rho_2^3} + \omega^2 y - 2\omega\dot{x} \\
\ddot{z} = -\frac{GMz}{\rho_1^3} - \frac{Gmz}{\rho_2^3}
\end{cases}
\tag{6.11}
$$

The solution for these equations can't be calculated analytically as mentioned before but we can find an integral, E_J called Jacobi integral:

$$
E_J = \frac{1}{2}v^2 + \Phi_{eff}(\boldsymbol{r})
\tag{6.12}
$$

where $\Phi_{eff}(\boldsymbol{r})$ is the effective potential given by the gravitational potential and the centrifugal repulsive one:

$$
\Phi_{eff}(\boldsymbol{r}) = \Phi(\boldsymbol{r}) + \frac{1}{2} \mid \boldsymbol{\omega} \times \boldsymbol{r} \mid^2 =
\tag{6.13}
$$

$$
= -\frac{GM}{\mid \boldsymbol{r_1} \mid} - \frac{Gm}{\mid \boldsymbol{r_2} \mid} - \frac{\omega^2}{2}(x^2 + y^2)
\tag{6.14}
$$

If we take $v = 0$ in equation (6.12) we can find the zero-velocity curve for a given object with Jacobi integral $E_J = \Phi_{eff}(\boldsymbol{r})$. Even since this is not an analytical solution for the problem, it helps in determining the zones allowed for the motion of the point-like mass because velocity cannot be $v < 0$, then the object will never be able to cross the zero-velocity curve. An example of equipotential curves for $\Phi_{eff}(\boldsymbol{r})$ is shown in Figure 6.2. A body with Jacobi integral equal to the value of the effective potential of one of the curves in Figure won't thus be able to cross the curve during its motion.

6.3 Lagrangian points.

The effective potential (6.13) can be used to calculate particular points in which a test particle can be in equilibrium. If we resolve:

$$
\nabla \Phi_{eff}(\boldsymbol{r}) = 0
\tag{6.15}
$$

we would find five points of equilibrium called Lagrangian points which co-rotate with the system and are indicated with the capital letter L.

These points can be distinguished into point of stable and unstable equilibrium and can be also calculated making simple physical observations. A scheme for the position of Lagrangian points is shown in Figure 6.3.
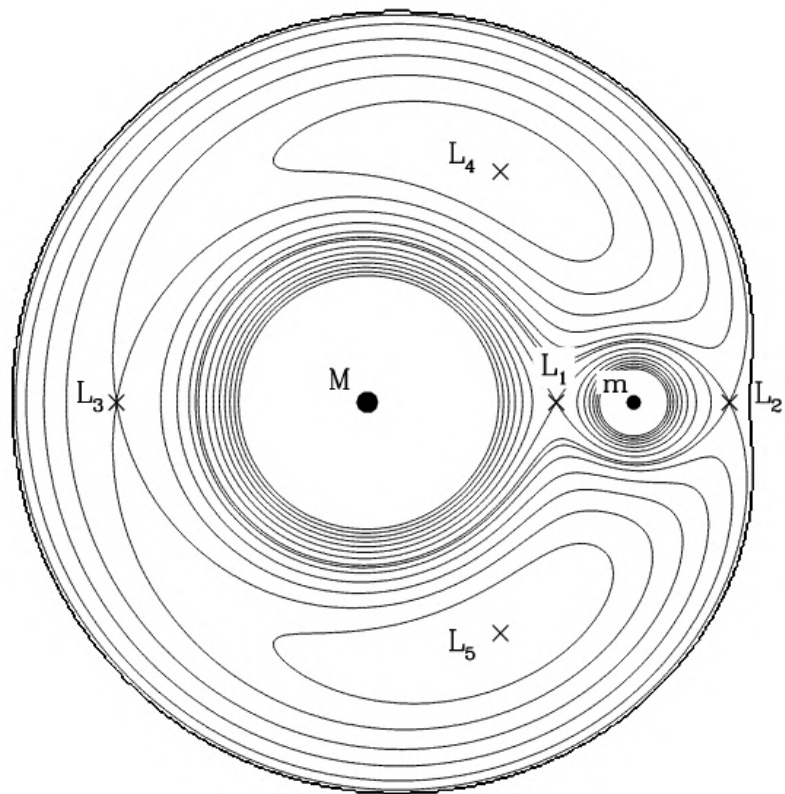
Figure 6.2: Zero-velocity curves calculated using the relation (6.12) plotted in Binney and Tremaine 2008.
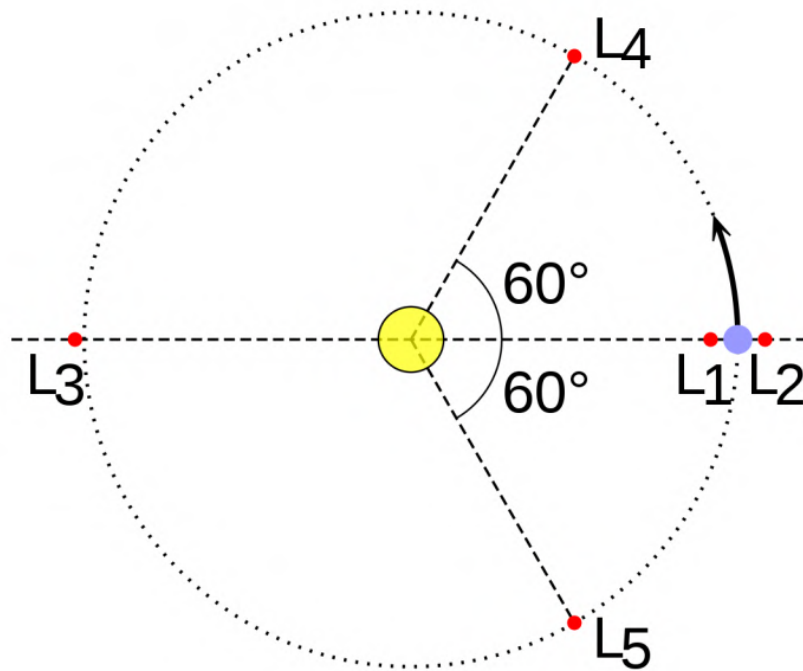
Figure 6.3: Representation of the position of Lagrangian points in a Sun-planet system. Credits: Media INAF

Lagrangian points can be calculated in every situation where two large bodies gravitationally interact such as the Sun and the Earth, the Sun and other planets, or the Earth and the Moon. In the Sun-Earth system the Lagrangian point L_2 hosts some important telescopes such as Gaia and the James Webb Space Telescope.

Collinear equilibrium points. The first three Lagrangian points are aligned with the main bodies and can be easily understood by equating the acting forces.

L_1 point is between the two bodies and is given by the equilibrium between the gravitational forces of the two masses. L_2 point is located outside the less massive body and L_3 point is outside the most massive body, each of them can be calculated equating the sum of gravitational forces to the centrifugal one.

L_1, L_2, and L_3 are all points of unstable equilibrium and we can see this if we resolve (6.15) and take $y = 0$. This solution will give only the collinear equilibrium points as shown in Figure 6.4.

Triangular equilibrium points. The last two Lagrangian points, L_4, L_5, can be found calculating the third vertex of the equilateral triangle formed by the centre of mass of the two main bodies
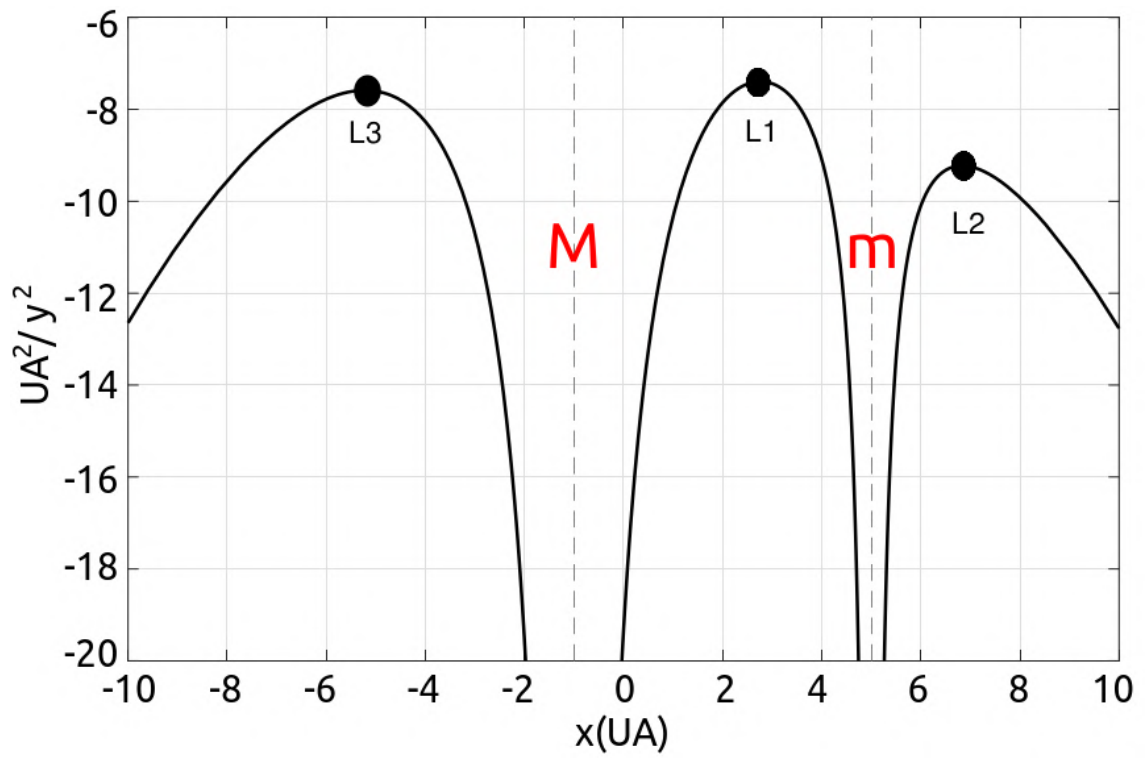
Figure 6.4: Plot of the effective potential in which the three unstable Lagrangian points are shown. The position of the bodies is marked in red with $M > m$ and a separation of 6 AU. Credits: Marco Monaci.

having by side the distance between the two centre of mass. Also these two points as L_1 represent the equilibrium between the two gravitational forces but in this case the equilibrium is stable.

6.4   Hill sphere.

The effective potential can be used also to compute the radius of the Hill sphere just by taking into consideration the situation shown in Figure 6.2. We can see that there are some orbits closed around the two masses and it's possible to calculate the radius of the farthest of these closed orbits because the point L_3 in Figure 6.2 is a saddle point. We then can write:

$$\left(\frac{\partial \Phi_{eff}}{\partial x}\right)_{r_2 - r_H} = 0 \tag{6.16}$$

where r_H is the radius of the farthest closed orbit from m and $r_2 - r_H$ is the position of the saddle point in the co-rotating reference frame. Solving this equation using the effective potential (6.13) leads to:

$$\left(\frac{\partial \Phi_{eff}}{\partial x}\right)_{r_2 - r_H} = G\left[\frac{M}{(R_0 - r_H)^2} - \frac{m}{r_H^2} - \frac{M+m}{R_0^3}\left(\frac{MR_0}{M+m} - r_H\right)\right] = 0 \tag{6.17}$$

in which R_0 is the distance between the masses M and m. Since this equation is solvable computationally, we can make the approximations $m \ll M$ and $r_H \ll R_0$ thus $(R_0 - r_H)^{-2}$ can be expanded:

$$0 = \frac{M}{R_0^2}\left(1 + \frac{2r_H}{R_0} + \dots\right) - \frac{m}{r_H^2} + \frac{M+m}{R_0^3}r_H \simeq \frac{3Mr_H}{R_0^3} - \frac{m}{r_H^2} \tag{6.18}$$

is then possible to obtain the Hill radius as:

$$r_H \approx R_0 \sqrt[3]{\frac{m}{3M}} = a \sqrt[3]{\frac{m}{3M}} \tag{6.19}$$

where R_0 is usually expressed as the semi-major axis of the orbit, a. Hill radius is also called Roche or Jacobi radius and is shown, not to scale, in Figure 6.6 where is represented for the Sun-Earth-Moon system. The Hill radius can be calculated both for objects of the Solar System with respect to the Sun and for the Sun with respect to the Galaxy.

In the work of Chebotarev 1965 the author calculates the Hill sphere of the Sun and what could happen when the Solar System encounters a comet at different distances and different motion (direct or retrograde with respect to the Sun's motion). Chebotarev finds that direct motion of a comet inside the Hill sphere of the Sun allows the comet to have a stable orbit while for retrograde motions stable orbits are reached only if the cometary orbit has a maximum radius of 10^5 AU. Using values for the mass of the Galaxy calculated from our density profile and the rotation curve

Mass $[\text{M}_\odot]$	r_H [pc]	r_H [au]
0.1	0.62	$1.3 \cdot 10^5$
1	1.4	$2.9 \cdot 10^5$
10	2.9	$6.0 \cdot 10^5$

Table 6.1: In this Table are shown representative values of Hill radius for different stellar objects ranging from brown dwarf to high mass stars.

discussed in Section 5.3 and 5.4 we get:

$$M_{gal}(R_\odot) = 7.52 \cdot 10^{10} \, \text{M}_\odot \qquad (6.20)$$

while the Sun distance from the centre of the Galaxy is (2.2). We thus can calculate the Hill radius for the Sun:

$$r_{H,\odot} \approx 8.20 \, \text{kpc} \sqrt[3]{\frac{1 \, \text{M}_\odot}{3 \cdot 7.52 \cdot 10^{10} \, \text{M}_\odot}} = 1.35 \, \text{pc} \sim 2.78 \cdot 10^5 \, \text{au} \qquad (6.21)$$

In general we can calculate this quantity for every star in the Solar neighbourhood and if we assume that all stars are nearly at the same distance from the Galactic centre, we can see from Table 6.1 that Hill radius changes only by a factor ~ 2 for mass magnitude. This can be shown considering two objects of masses m_1 and m_2 and same semi-major axis a. Their Hill radius with respect to the Galaxy will then be:

$$r_{H,1} \approx a \sqrt[3]{\frac{m_1}{3M}} \qquad (6.22)$$

$$r_{H,2} \approx a \sqrt[3]{\frac{m_2}{3M}} \qquad (6.23)$$

so if we calculate the ratio between the two Hill radius,

$$\frac{r_{H,1}}{r_{H,2}} = \frac{\sqrt[3]{m_1}}{\sqrt[3]{m_2}} \qquad (6.24)$$

thus if $m_1 = 10m_2$ we obtain $\frac{r_{H,1}}{r_{H,2}} = \sqrt[3]{10} \sim 2$. We can also define where the L_1 point is positioned on the semi-major axis a, independently of its value, by calculating a ratio between the two radius, $r_{H,1}$ and $r_{H,2}$ and using (6.24):

$$\begin{cases} r_{H,1} + r_{H,2} = a \\ \frac{r_{H,1}}{r_{H,2}} = \sqrt[3]{\frac{m_1}{m_2}} \end{cases} \qquad (6.25)$$

performing the calculations gives us the following relation:

$$\frac{r_{H,1}}{a} = \left[1 - \frac{r_{H,2}}{a} \right] \left(\frac{m_1}{m_2} \right)^{1/3} \quad , \qquad (6.26)$$
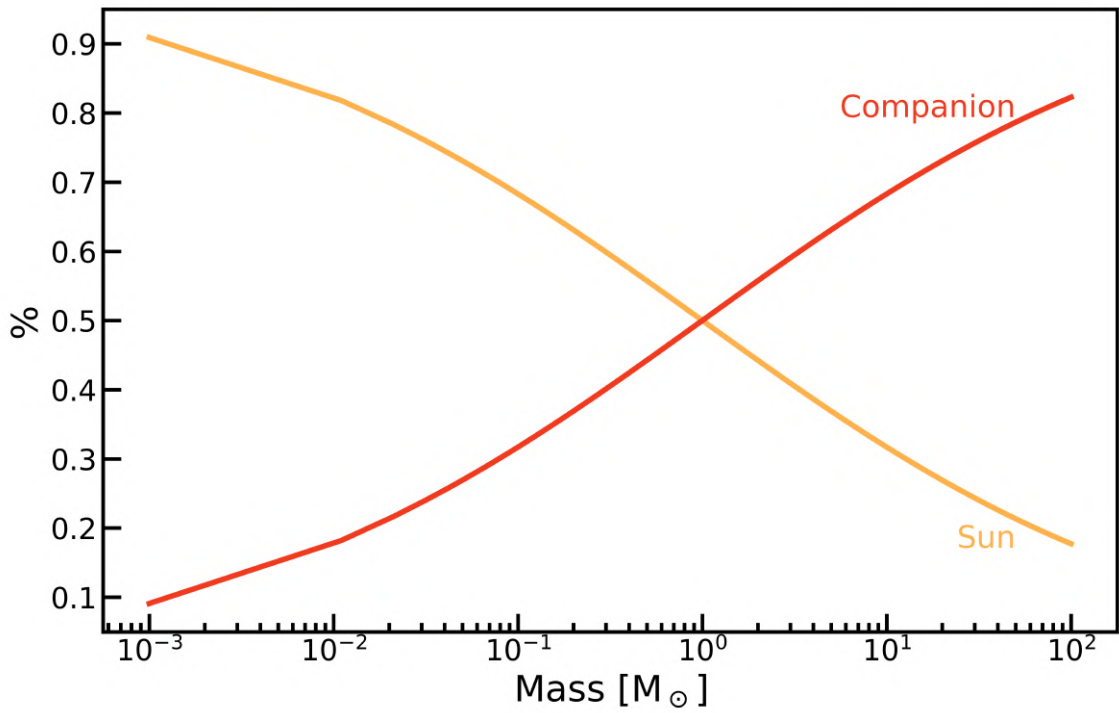
Figure 6.5: Hill radius proportions for a Solar-type star and a variable mass companion.

substituting now $P_1 = \frac{r_{H,1}}{a}$, $P_2 = \frac{r_{H,2}}{a}$, and $R_m = \left(\frac{m_1}{m_2}\right)^{1/3}$ we get the following two proportions which are only dependent on the masses m_1, m_2 of the objects and which set the position of L_1:

$$P_1 = \frac{1}{R_m^{-1/3} + 1} \tag{6.27}$$

$$P_2 = 1 - P_1 \tag{6.28}$$

In Figure 6.5 is shown this last relation using a Solar-type star as m_1 (thus having $m_1 = 1\,\mathrm{M_\odot}$) and with m_2 ranging from $0.01\,\mathrm{M_\odot}$ to $100\,\mathrm{M_\odot}$.
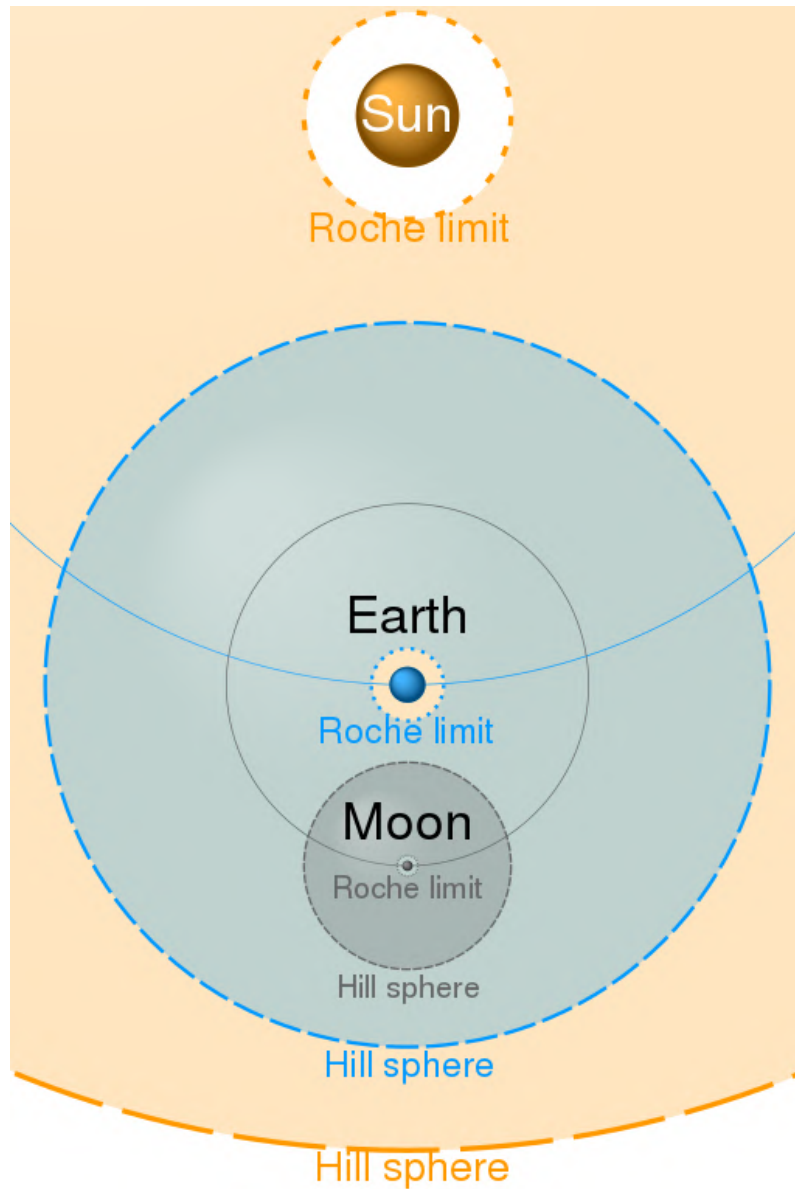
Figure 6.6: Example of Hill sphere for Sun-Earth system. Credits: Cmglee.
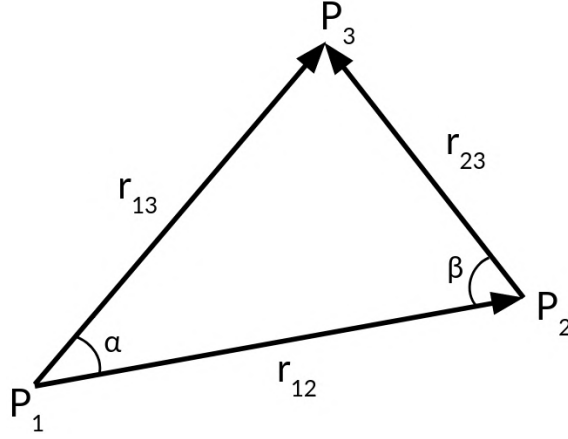
Figure 6.7: Sketch of bodies involved in the calculations of the SOI radius.

6.5 Sphere of influence

There is an alternative way to define the region in which the presence of a body is gravitationally dominant and the test object is attracted by it. The Hill radius can be seen as the point at which a third body would have the same orbital velocity both if it would be bounded the primary or the secondary body. This is related to the derivative of the effective potential but we can also study the forces that are exerted on the third body by both of the main bodies. This other point of view on a three-body dynamical situation leads to the definition of the Sphere of Influence, SOI. The radius of the SOI is calculated matching the forces exerted by the two main bodies. We will have thus two scale length definitions for the region in which we can consider a body as the dominant one and we will take into account both of them since, as we will see further on, the Oort cloud resides between the two spheres.

We can define the Sphere of Influence, SOI, of a body starting from Figure 6.7. As described in Kaplan 1976, if we take P_1 and P_2 as the main bodies and P_3 as the test mass, we can write the motion of P_3 with respect to P_1 and P_2:

$$\ddot{\boldsymbol{r}}_{13} + \frac{G(m_1 + m_3)}{r_{13}^3}\boldsymbol{r}_{13} = -Gm_2\left(\frac{\boldsymbol{r}_{23}}{r_{23}^3} + \frac{\boldsymbol{r}_{12}}{r_{12}^3}\right) \tag{6.29}$$

$$\ddot{\boldsymbol{r}}_{23} + \frac{G(m_2 + m_3)}{r_{23}^3}\boldsymbol{r}_{23} = -Gm_1\left(\frac{\boldsymbol{r}_{12}}{r_{12}^3} - \frac{\boldsymbol{r}_{13}}{r_{13}^3}\right) \tag{6.30}$$

in these equations on the left hand side is shown the gravitational contribute of the body of whom the motion is respect to and on the right hand side there is the contribute of disturbance from the third object. Taking now the disturbing force F_d and the central force F_c we can see from the ratio

of these two which one will prevail on the other:

$$\frac{F_{d,2}}{F_{c,1}} = \frac{Gm_2\left[\left(\frac{\boldsymbol{r}_{23}}{r_{23}^3} + \frac{\boldsymbol{r}_{12}}{r_{12}^3}\right) \cdot \left(\frac{\boldsymbol{r}_{23}}{r_{23}^3} + \frac{\boldsymbol{r}_{12}}{r_{12}^3}\right)\right]^{1/2}}{G(m_1 + m_3)/r_{13}^2} \tag{6.31}$$

$$\frac{F_{d,1}}{F_{c,2}} = \frac{Gm_1\left[\left(\frac{\boldsymbol{r}_{13}}{r_{13}^3} + \frac{\boldsymbol{r}_{12}}{r_{12}^3}\right) \cdot \left(\frac{\boldsymbol{r}_{13}}{r_{13}^3} + \frac{\boldsymbol{r}_{12}}{r_{12}^3}\right)\right]^{1/2}}{G(m_2 + m_3)/r_{13}^2} \tag{6.32}$$

if we now search for equilibrium we can equate the ratios. Taking into account that usually in these kind of system one of the masses is prevalent and that the third is smaller than others we can write $m_1 \ll m_2$ and $r_{13} \ll r_{12}$ and by approximation we get the value for the radius of the sphere of influence:

$$r_{SOI,13} \approx r_{12}\left(\frac{m_1}{m_2}\right)^{2/5} = a\left(\frac{m}{M}\right)^{2/5} \quad , \tag{6.33}$$

in the last member of the expression the terms are changed to the semi-major axis, a, the mass m of the less massive object, and the mass M of the most massive one in order to compare the SOI radius with the Hill one, (6.19). We can thus calculate the same proportion as (6.27) for the SOI radius. This will tell us what percentage, P_1 and P_2, of a distance a between two bodies belongs to the first or the second:

$$P_1 = \frac{1}{R_m^{2/5} + 1} \tag{6.34}$$

$$P_2 = 1 - P_1 \tag{6.35}$$

where R_m is the mass ratio and $P_1 = \frac{r_{SOI,1}}{a}$, $P_2 = \frac{r_{SOI,2}}{a}$. This relation is shown in Figure 6.8. If we compare the two radii we can see there is a difference in the dependence from the mass ratio, indeed Hill radius has a $1/3$ dependence from the mass ratio while SOI radius has a $2/5$ dependence as we can see in Figure 6.9 where the two radius are plotted calculating the radii for a stellar object with variable mass at the Sun's position (2.2).

We compared Hill and SOI radii for some classic cases as the planets of the Solar System with respect to the Sun in Table 6.2 were we can see that Hill radius is higher than the SOI one. This can be explained by considering that Hill radius is calculated looking for the point in which the two gravitational forces are in equilibrium thus is not taken for granted that a a mass near this point won't be affected by the gravitational force of both the objects. On the other side is the SOI radius that take into account this feature and calculates the zone in which a body can be considered the only attracting mass and thus the centre of coordinates.

Since anyway the value of the two radii are different but comparable, we will use the Hill radius in our forthcoming calculations.
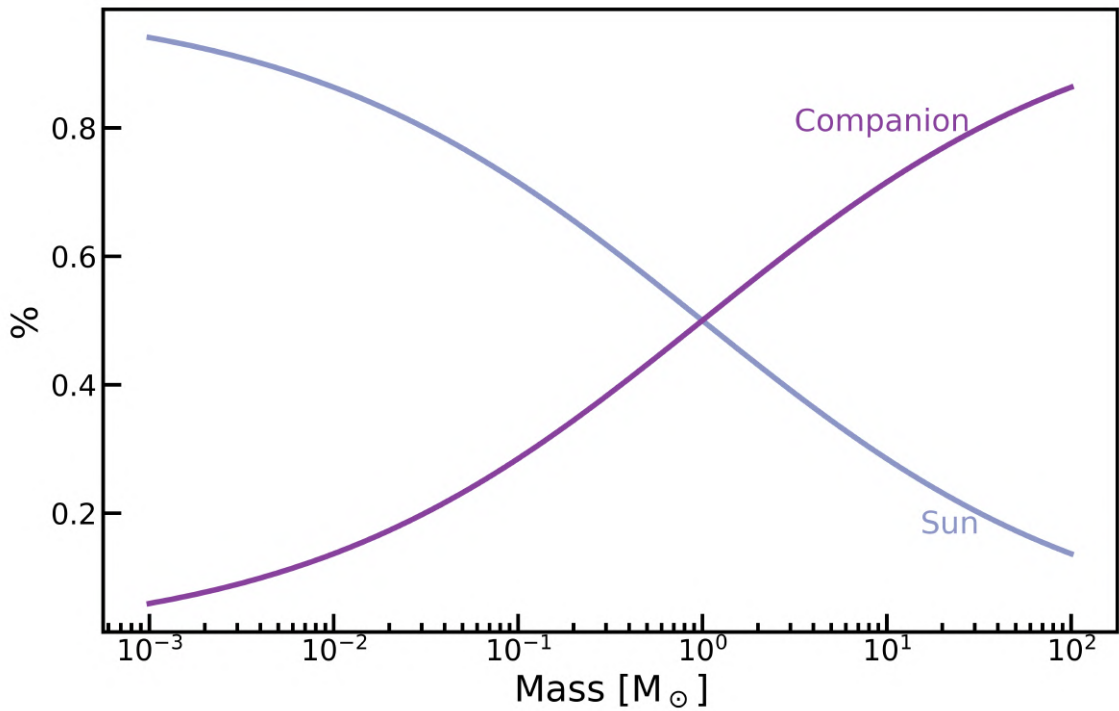
Figure 6.8: This plot represents the proportions of SOI radii for a Sun like star and a variable mass companion.

6.6 Galaxy influence over the Solar System: implications for the Oort cloud.

It is possible to characterize the gravitational influence of the Galaxy with respect to the Solar System following the relations given by Sect. 6.4, 6.5. The results are shown in Table 6.3 where the column Galaxy Mass represents the mass enclosed at a Solar distance (2.2) calculated using the Galaxy rotation curve 5.4. From the Table we can see a significant difference between the Hill radius and the SOI one. We can calculate these quantities also for different stars as shown in Figure 6.9. The first plot represents the Hill and SOI radii for stars of different mass all at the same radial distance, taken as Solar. In this case the distance and the Galaxy mass are fixed and only the star mass varies as $m^{1/3}$ for the Hill radius and as $m^{2/5}$ for the SOI radius. The Hill radius function is then raised by the multiplicative factor $1/\sqrt[3]{3}$.

Planet	Mass [$M_\odot$]	Hill Radius [AU]	SOI Radius [AU]
Mercury	$1.67 \cdot 10^{-7}$	$1.47 \cdot 10^{-3}$	$7.82 \cdot 10^{-4}$
Venus	$2.46 \cdot 10^{-6}$	$6.75 \cdot 10^{-3}$	$4.11 \cdot 10^{-3}$
Earth	$3.02 \cdot 10^{-6}$	$1.00 \cdot 10^{-2}$	$6.20 \cdot 10^{-3}$
Mars	$3.24 \cdot 10^{-7}$	$7.24 \cdot 10^{-3}$	$3.86 \cdot 10^{-3}$
Jupiter	$9.59 \cdot 10^{-4}$	0.355	0.322
Saturn	$2.87 \cdot 10^{-4}$	0.436	0.364
Uranus	$4.38 \cdot 10^{-5}$	0.469	0.347
Neptune	$5.17 \cdot 10^{-5}$	0.776	0.576

Table 6.2: In this Table are compared values for Hill and SOI radii for planets of the Solar System with respect to the Sun and for the Sun with respect to the Galaxy.

Sun Mass [$M_\odot$]	Galaxy Mass [$M_\odot$]	Hill Radius [pc] ([au])	SOI Radius [pc] ([au])
1.00	$7.52 \cdot 10^{10}$	1.35 $(2.78 \cdot 10^5)$	0.367 $(7.51 \cdot 10^4)$

Table 6.3: Comparison between the Sun's Hill radius and SOI radius with respect to the Galaxy. The Galaxy mass used comes from the integration of our density profile 2.5 made in Sections 5.3 and 5.4.

6.6.1 The problem of the Solar System limit

The limit of the Solar System is not still accurately known as has never been observed a clear-cut edge of it. We although could state that the gravitational influence of the Sun is delimited by the Hill radius or the SOI radius. The usual limit of the Solar System is generally referred as the Oort cloud which is a spherical cloud of comets but a different definition for this limit can be represented by the heliopause, which states the zone in which the solar wind plasma density becomes equivalent to the Interstellar Medium. We will evaluate both of them in our dissertation as the heliopause can be a good tracer for the innermost part of the Solar System which hosts planet orbits, and the Oort cloud, as we will describe in Chapter 7, could have a prominent role in the dynamical interactions with near stars.

Oort cloud Today, the Oort cloud is considered as the outermost component of the Solar System. This feature make possible for it to be easily involved into gravitational interactions between the Sun and other stars. The Oort cloud is composed by a large amount of small bodies which, when properly perturbed, we can observe from Earth as Long Period Comets, LPCs. Due to the high distance of the cloud from the Sun we still not observe the cloud itself but only the comets, thus deducing the presence of it by making observations upon gravitational effects of planets and objects outside the Solar System on the orbits of LPCs. The idea of a spherical distribution of bodies at a large distance from the Sun -but still under the effect of the Solar System gravitational influence- comes from the work of Oort which also stated that the comets have always belonged
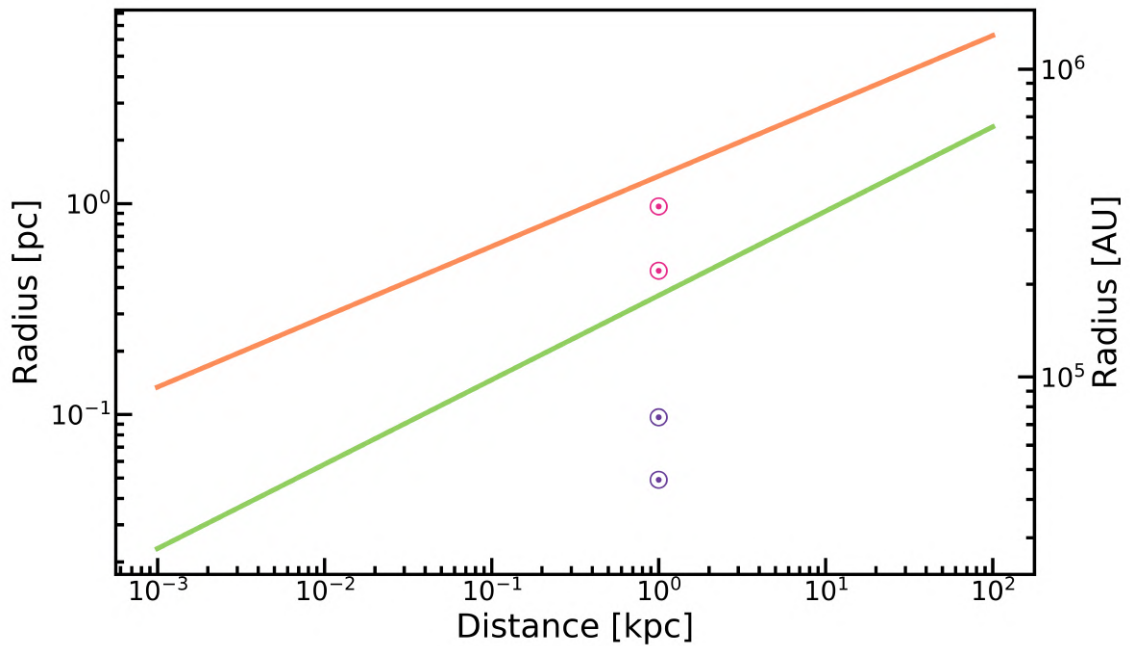
Figure 6.9: In this plot Hill and SOI radii are represented. Both the curves are calculated for a stellar object at the Sun's position with respect to the Galaxy.

to the Solar System. Oort's 1950 work was forerun by Öpik's (Öpik 1932) where the author studies the effects of a perturbing star upon comets with long period and states the limits of the Solar System to 10^6 au (which corresponds with almost 5 pc, way much outer Hill radius) but doesn't hypothesize the presence of a cloud of objects as later will do Oort.

Oort dealt with the problem of LPC in 1950 (Oort 1950) when he reviewed Öpik's work and extended it taking into account the gravitational effects of planets onto the comets. The problem which Oort aimed to solve was the possible evaporation of LPCs. Both the planets and passing stars are a possible gravitational disturbers of the orbit of a comet. Since the orbit of a comet is defined by a semi-major axis and a perihelion distance, the effects of planets and stars will change these values. If we only take into account the presence of planets, this will most affect the semi-major axis of the comet's orbit thus leaving the perihelion distance almost the same. This would lead to the increase of semi-major axis and to the comets that leaves the Solar System, causing a sort of evaporation. Also the presence of near stars could pull out comets from the Solar System but could have also a stabilizing effect on the orbits of LPCs: the perturbative effect of near stars tend to increase the perihelion distance more than the semi-major axis thus providing a stabilizing effect if balanced with the planets gravitational effect. Taking into account these two effects
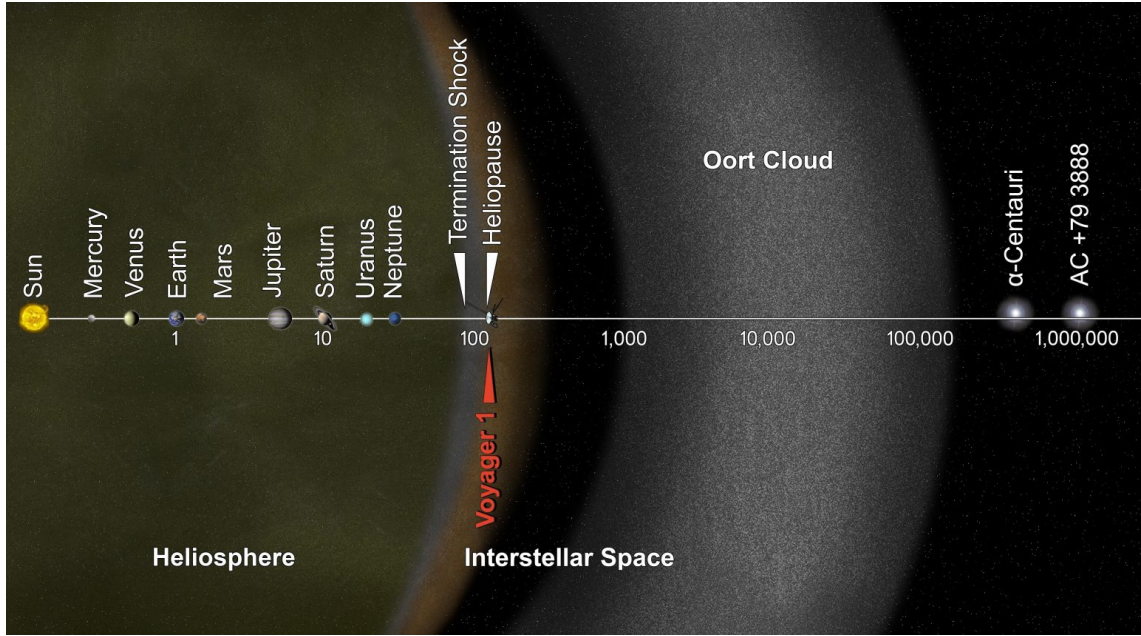
Figure 6.10: Outline of a slice of Solar System representing the position and distance of some components with respect to the Sun. The Oort cloud -which is still not observed- is believed to have the inner edge at a $1 - 2 \cdot 10^4$ au distance and the outer edge positioned at $1 - 2 \cdot 10^5$ au from the Sun. Credits: NASA Science-Solar System Exploration.

Oort calculated the inner and outer radius for the comets cloud:

$$r_{in} = \text{1-2} \cdot 10^4 \text{ au ;} \tag{6.36}$$

$$r_{out} = \text{1.5-2} \cdot 10^5 \text{ au ,} \tag{6.37}$$

the outer radius is uncertain because if we only take into account the stellar effect we can derive a radius of $2 \cdot 10^5$ AU. In these dimensions should reside a spherical cloud composed by comets which Oort calculated to be $N \sim 10^{11}$ whit a total mass less than Earth's mass.

More recent works, e.g. the one of Duncan et al. 2008, are focused on the origin of the Oort cloud and give updated values for the number of comets which should be $N \sim 10^{11}$ and for the mass of the outer Oort cloud that should be int the range $M_{cloud} \in [\sim 1, 60]$ $M_{\oplus}$. Some of the limits usually used for the typical inner and outer radius of the Oort cloud are shown in Figure 6.9. From these plots the Oort cloud should reside inside the Hill sphere with inner radius inside the SOI. We do not expect that the Oort cloud extends outer the Hill sphere because Sun's gravity couldn't keep bound these objects and from the plots we can see that most of the cloud is around the SOI. This feature may suggest a sort of evaporation of the outer zones of the Oort cloud due to gravitational perturbations. In Figure 6.10 is represented a schematic view of the position of the Oort cloud in the Solar System.

Heliopause   The heliopause is the limit of the heliosphere and can considered, as for the Oort cloud, a boundary for the Solar System. The heliosphere is a bubble-shaped region which is filled by plasma coming from the Solar wind. When the wind reaches high distances from the Sun it weakens and the heliopause sets the limit of the efficiency of the Solar wind. Outside this limit the heliosphere interacts with the interstellar medium and causes a bow-shock. The spacecrafts Voyager 1 and Voyager 2, along with other missions like IBEX[1], measured the position of the heliopause and found that it has an asymmetric shape, as in Stone et al. 2008, with a radius of 83.7 au in the southern hemisphere and $\sim$ 73 au in the northern one. In Chapter 7 we will use the mean of these two values to do our calculation upon a possible deep perturbation onto the Solar System.

---

1. Interstellar Boundary EXplorer

Chapter 7

Results

7.1 Connecting the wires.

In this Chapter we will show the outcomes of this thesis work. We have modelled local Galaxy taking into account local parameters, as the local stellar density, in Chapter 2 and in Chapter 3 we used the results of Chapter 2 along with stellar evolution concepts to obtain representative models for the mass distribution of near stars, the PDMF.

We then characterized the motion of these stars assuming a mean velocity given by the LSR, as explained in Chapter 5, and finally we investigated the possibility of a dynamical interaction between the Sun and the Galaxy or other stars in Chapter 6.

This Chapter will be thus make use of the estimated quantities and relations coming from previous Chapters to picture the current situation of Solar System neighbourhood. We will integrate the PDMF to obtain scale distances and timescales for both the steady and unsteady configuration of stars near the Sun and we will highlight the role of massive stars as sources of high energy radiation hitting the Solar System and the role of low mass stars and objects which can perturb our Solar System and conversely be perturbed by the Sun.

In Section 7.2 we will integrate the PDMF to evaluate the mean distance of different star mass classes.

In Section 7.3 we will show the effects of the presence of high mass stars and the stellar perturbation by low mass bodies.

In Section 7.4 we then will investigate the effect of the Sun on other stars and highlight the possibility of perturbation of alien Oort clouds and exoplanets.
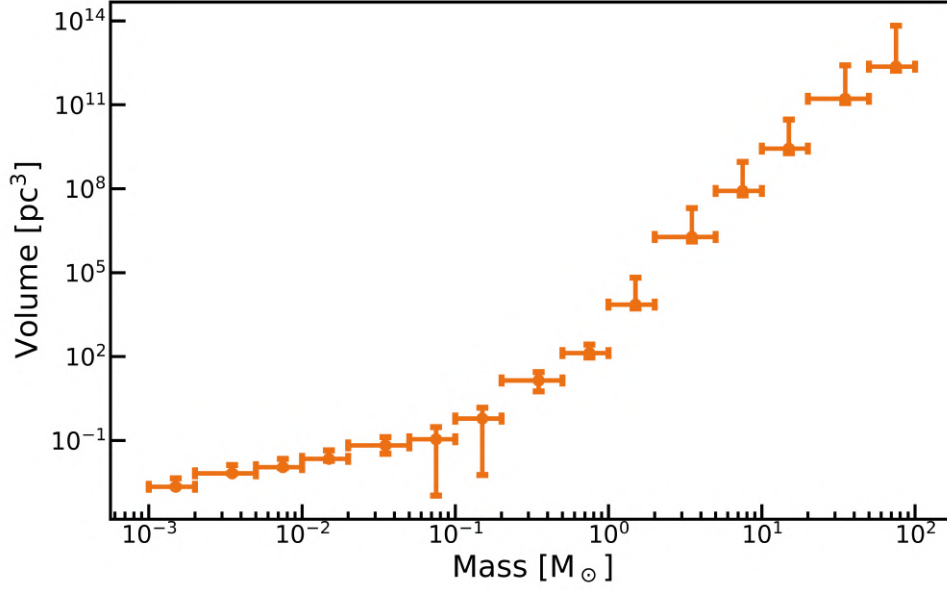
Figure 7.1: The volume given by 7.1 for the PDMF model in use and its upper and lower boundary based on the other models considered.

7.2 Stellar mean distance in the Solar neighbourhood

The PDMF, $\Phi(M)$, can be used to establish the mean spherical volume centred on the Sun in which we should find at least one stars of mass M. We choose as reference model the PDMF calculated using the Salpeter IMF and constant SFR and indicated as boundaries the PDMF models with highest and lowest values.

The volume will thus be given by:

$$V(M)dM = \frac{1}{\Phi(M)} \quad .$$

(7.1)

To get the volume value we integrated this equation into roughly equispaced logarithmic bins of some $\Delta \log M = 0.3$ wide from $1 \cdot 10^{-3}$ $M_\odot$ to 10^2 $M_\odot$. In this way we get the relations shown in Figure 7.1 where the volumes are shown relatively to the stellar mass. Each point has an horizontal bar that represents the mass range and a vertical bar that represents the upper and lower boundary. From this relation we can get the mean distance, $\langle l \rangle (M)$, at which we expect to find at least one star within each bin:

$$\langle l \rangle (M) = \sqrt[3]{\frac{3V(M)}{4\pi}}$$

(7.2)

this relation is integrated in the mentioned bin ranges and shown in Figure 7.2 where the mean distance is plotted against the mass.
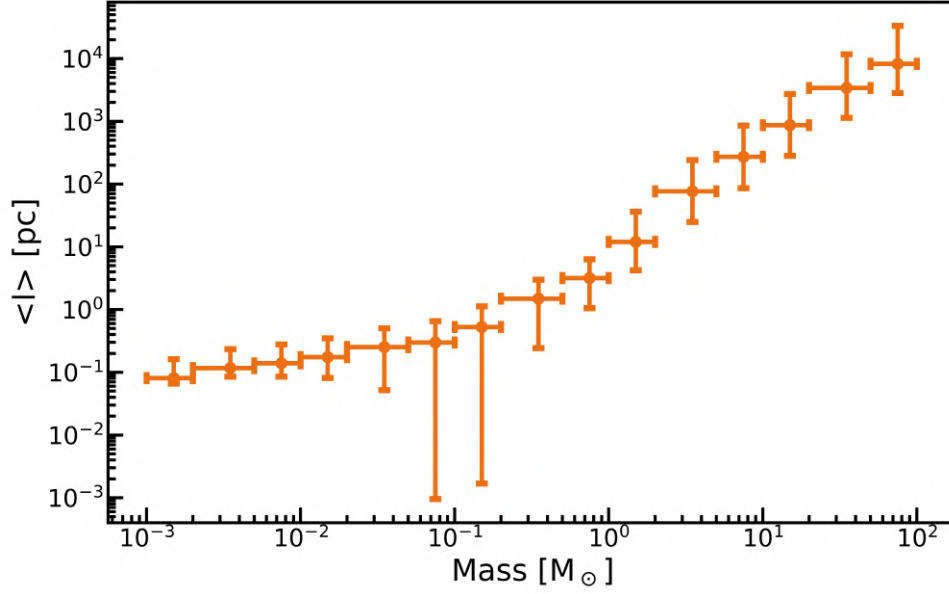
Figure 7.2: Characteristic distance $\langle l \rangle (M)$ from (7.2) for the considered PDMF model and its boundaries.

7.3 Stellar interactions with the Sun.

We now report some calculations that show us relevant information on the behaviour of high mass stars and low mass stars in the Sun vicinity.

7.3.1 A criterion for dynamical perturbation onto the Solar System

It is also possible, knowing the mean distance $\langle l \rangle (M)$, to calculate the boundaries for dynamical interactions between the Sun and the stars in the Solar neighbourhood. The effects of dynamical interaction will involve mainly low mass objects as we will show in this paragraph. In Section 6.4 we calculated what fraction P_1 of the distance between the Sun and other stars belongs to the Hill radius of the Sun, $r_{H,\odot}$. We can apply this feature to the mean distance value (7.2) obtaining the Hill radius value both for the Sun and other stars:

$$r_{H,\odot} = P_1 \langle l \rangle (M) \qquad ; \qquad (7.3)$$

$$r_{H,*} = \langle l \rangle (M)[1 - P_1] \qquad . \qquad (7.4)$$

For the dynamical interaction to happen, it is necessary to take into account also the dynamical effect of the Galaxy on the Solar System. If we compare the Hill radius of the Sun with respect

to the Galaxy, $r_{G,\odot}$, (which also can represent the Oort cloud limit as discussed in Section 6.6.1) with the Hill radius of the Sun with respect to a near star, $r_{H,\odot}$, the condition for the Sun-star dynamical interaction to happen is the following:

$$r_{H,\odot} < r_{G,\odot} \quad . \tag{7.5}$$

If this condition is satisfied, the Hill sphere of the interacting star, with radius $r_{H,*}$, overlaps the Hill sphere generated by the influence of the Galaxy over the Sun, of radius $r_{G,\odot}$, and since this latter can be assumed to represent the outer radius of the Oort cloud, this particular situation lets the interacting star perturb or even strip objects located in between the two radii. This situation is depicted in the first panel of Figure 7.3.

7.3.2   The impact of type II Supernovae on the Solar System

We can evaluate the time spent by a star of mass M to cross the mean volume described in Sect. 7.2. If we take our reference frame as co-moving with the Sun, the velocity (5.38) will represent the mean velocity of stars in the Solar neighbourhood while the Sun is at rest:

$$\tau_{cross}(M) = \frac{2\langle l \rangle (M)}{v} \tag{7.6}$$

The results are shown in Figure 7.4 in which the crossing timescale is plotted against the mass. We then superposed to this timescale the stellar lifetime, $\tau_{MS}(M)$, calculated in Section 3.3 from the work of Buzzoni 2002. In Table 7.1 are summarized some useful quantities.
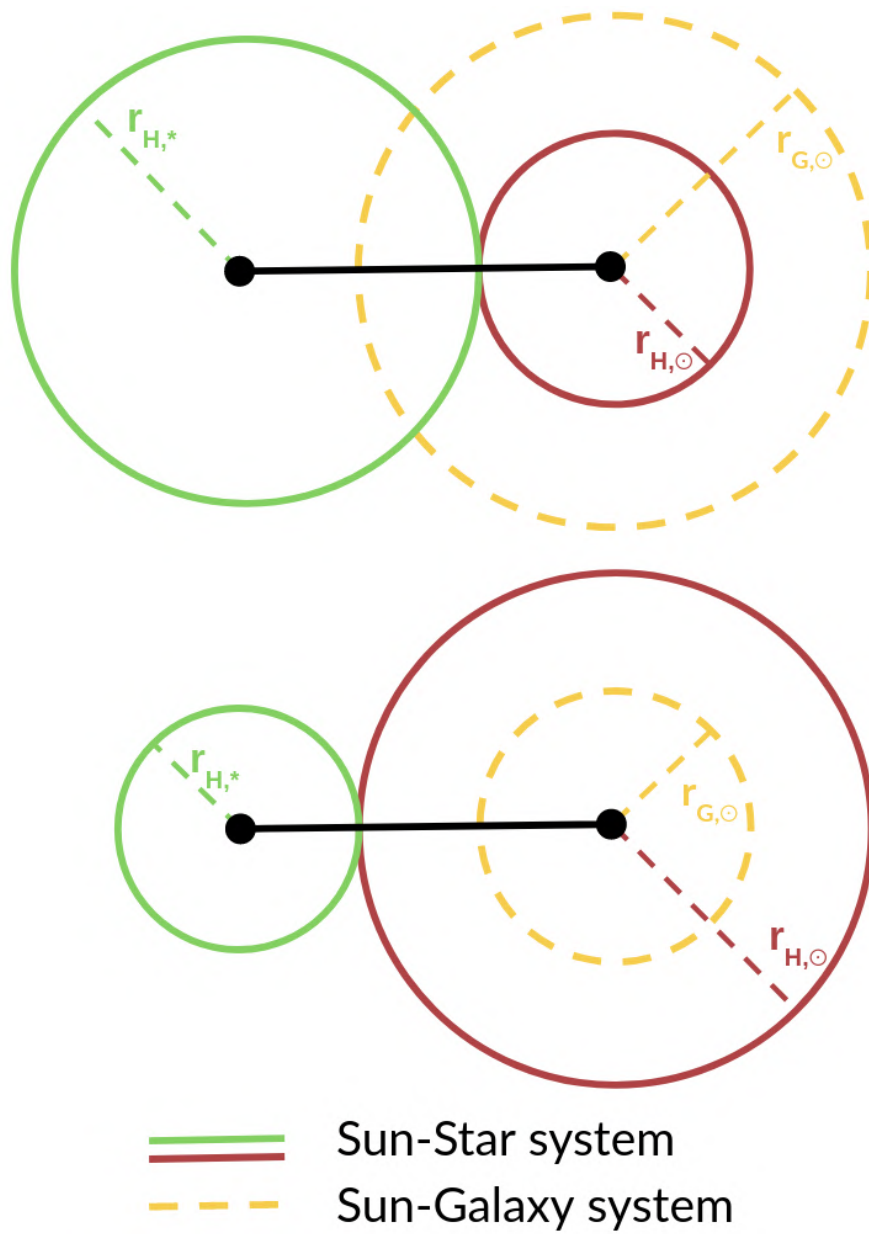
Figure 7.3: Sketch of the possible dynamical interaction situations, based on the companion mass.
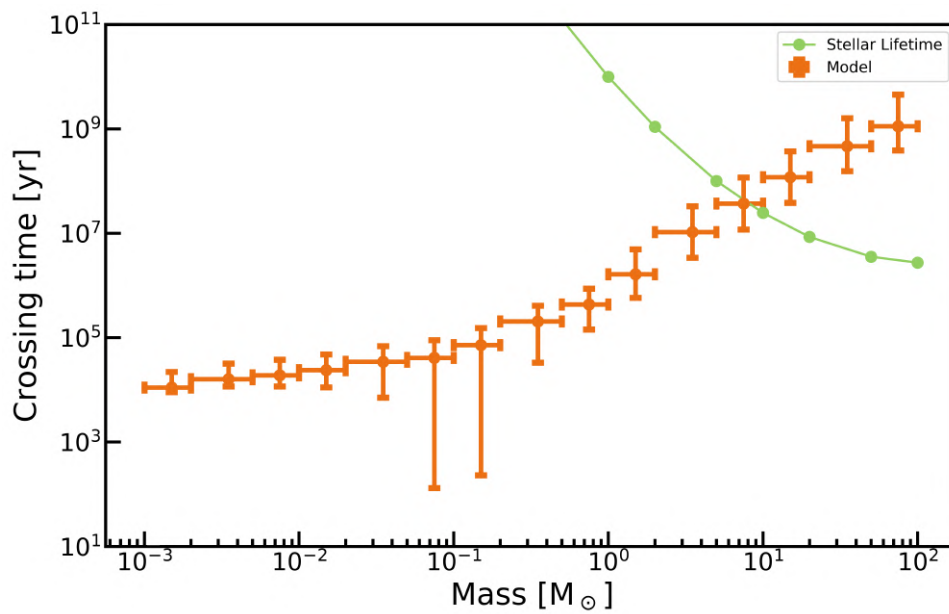
Figure 7.4: This Figure shows the expected timescale needed for the star to cross the distance represented in Figure 7.2 compared with the stellar lifetime.

Mass range	$\Phi(M)$ [pc^{-3}]	τ_{cross} [yr]	τ_{MS} [yr]	$\tau_{cross} < \tau_{MS}$	SNII
>50	$4.1 \cdot 10^{-12}$	$5.3 \cdot 10^{8}$	$[3.5 \cdot 10^{6} \text{-} 2.7 \cdot 10^{6}]$	yes	yes
[20-50]	$5.9 \cdot 10^{-11}$	$2.3 \cdot 10^{8}$	$[8.5 \cdot 10^{6} \text{-} 3.5 \cdot 10^{6}]$	yes	yes
[10-20]	$3.5 \cdot 10^{-9}$	$5.6 \cdot 10^{7}$	$[2.5 \cdot 10^{7} \text{-} 8.5 \cdot 10^{6}]$	yes	yes
[5-10]	$1.1 \cdot 10^{-7}$	$1.8 \cdot 10^{7}$	$[1.0 \cdot 10^{8} \text{-} 2.5 \cdot 10^{7}]$	no	yes(>7 M$_\odot$)
[2-5]	$5.1 \cdot 10^{-6}$	$4.9 \cdot 10^{6}$	$[1.1 \cdot 10^{9} \text{-} 1.0 \cdot 10^{8}]$	no	no
[0.5-1]	$7.1 \cdot 10^{-2}$	$2.0 \cdot 10^{5}$	$[1.3 \cdot 10^{11} \text{-} 9.9 \cdot 10^{9}]$	no	no
[0.2-0.5]	0.69	$9.6 \cdot 10^{4}$	$[6.2 \cdot 10^{12} \text{-} 1.3 \cdot 10^{11}]$	no	no
[0.1-0.2]	16	$3.4 \cdot 10^{4}$	$[1.8 \cdot 10^{14} \text{-} 6.2 \cdot 10^{12}]$	no	no
[0.05-0.1]	86	$1.9 \cdot 10^{4}$		no	no
[0.02-0.05]	140	$1.6 \cdot 10^{4}$		no	no
[0.01-0.02]	440	$1.1 \cdot 10^{4}$		no	no
[0.005-0.01]	870	$8.9 \cdot 10^{3}$		no	no
[0.002-0.005]	$1.4 \cdot 10^{3}$	$7.5 \cdot 10^{3}$		no	no
[0.001-0.002]	$4.3 \cdot 10^{3}$	$5.2 \cdot 10^{3}$		no	no

Table 7.1: For each mass bin is reported the PDMF value, the crossing timescale and the stellar lifetime calculated using the model from Buzzoni 2002

	Mass $[\mathrm{M}_\odot]$	τ_{cross} [yr]
Upper boundary	9.0	$3.0 \cdot 10^7$
Model	12	$1.8 \cdot 10^7$
Lower boundary	14	$1.4 \cdot 10^7$

Table 7.2: In this Table is shown the limit mass at which $\tau_{cross}(M) = \tau_{MS}(M)$ for the main Model and its boundary values.

Mass $[\mathrm{M}_\odot]$	$\langle l \rangle$ [pc]	Flux $[\mathrm{erg\,s^{-1}\,pc^{-2}}]$
9.0	208	$1.8 \cdot 10^{29-30}$
12	141	$4.0 \cdot 10^{29-30}$
14	116	$5.9 \cdot 10^{29-30}$

Table 7.3: In this Table are reported the mean distance and X-ray flux for stars having $\tau_{cross} = \tau_{MS}$

The intersection between the two curves suggests the possibility of a SNII explosion in the Solar vicinity since the massive star would explode as a SNII while still travelling the volume and could possibly hit the Solar System with high energy radiation. We thus wanted to determine the mass corresponding to:

$$\tau_{cross}(M) = \tau_{MS}(M) \qquad (7.7)$$

to do this we integrated the relation (7.6) in the range $[7 - 22]\,\mathrm{M}_\odot$ using bin of $\Delta M = 1\,\mathrm{M}_\odot$ which is shown in Figure 7.5. The results in Table 7.2 show a limit mass between $9\,\mathrm{M}_\odot$ and 14 $\mathrm{M}_\odot$. Comparing these results with typical scale distances from 7.2 we get the results shown in Table 7.3 in which for a fixed velocity of the star (5.38), we can calculate the crossing timescale and the X-ray flux, knowing the SNII X-ray luminosity $\sim 10^{35-36}$ erg$\cdot$s^{-1} from Weaver et al. 1977.

7.3.3 Effect of low mass stars onto the Solar System Oort cloud.

In Figure 7.6, and 7.7 are represented the Hill radii both for the Sun and an interacting star. In Figure 7.6 are represented, overplotted to the Hill radius of the Sun, the Hill and SOI radius for the interaction between the Sun and the Galaxy. Indeed all the calculations we will make using the Hill radius can be done also using the SOI radius as both of them are acceptable for the definition of a dynamical boundary for a star in general as explained in Section 6.4, and the calculation method would be the same for both. If we would use the SOI radius for our calculations, firstly, the interaction between two objects would be deeper into the star or Sun system (for instance the Solar System Oort cloud is thought to begin at about the position of SOI Sun radius) and,

86
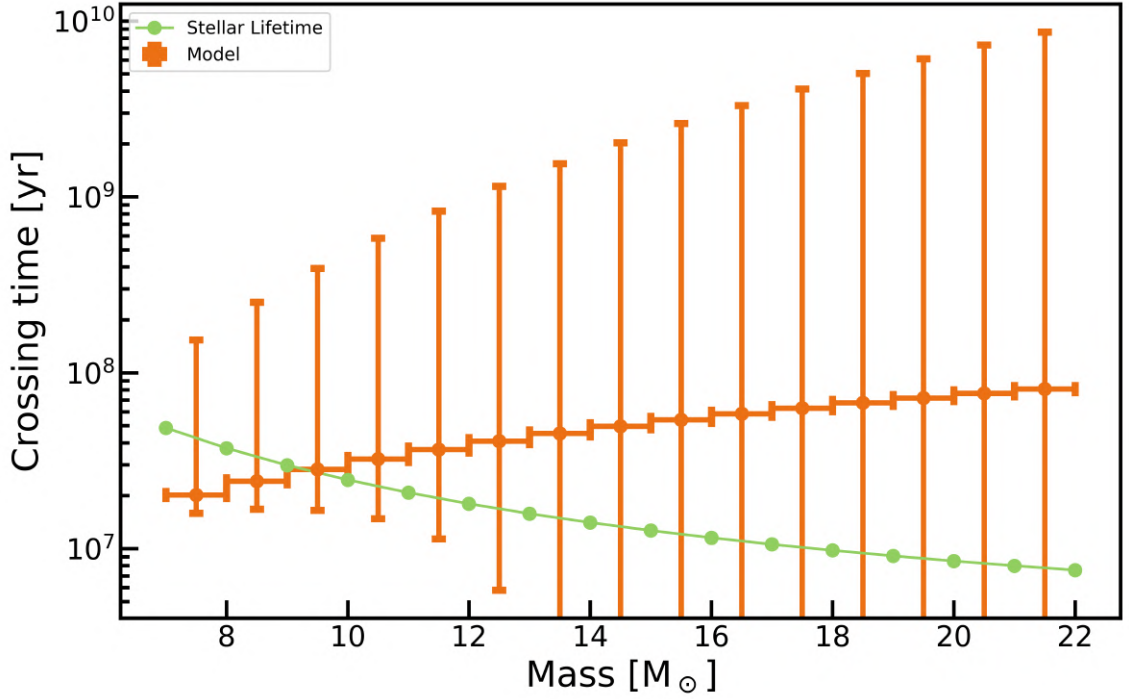
Figure 7.5: In this plot the (7.6) is integrated in 1 $M_\odot$ bins and is superposed with the stellar lifetime value.

	$M_{l,\odot}$ [$M_\odot$]	$r_{H,*}$ [pc]	$r_{G,\odot}$ [pc]	$\tau_{D,\odot}$ [yr]
Upper boundary	0.5	0.71	1.2	$2.4\cdot10^5$
Model	0.5	1.3	1.2	$3.5\cdot10^5$
Lower boundary	1.1	2.5	1.2	$3.9\cdot10^5$

Table 7.4: Values for the upper limit of the mass which can continually perturb the Solar System Oort cloud.

secondly, the frequency of interactions would decrease and the interactions would last less than the ones computed with Hill radii, as the SOI radii associated are smaller.

Going on with our dissertation we will continue using the Hill radius. We can thus define a limit mass, $M_{l,\odot}$, for which the Sun has an Hill radius lower than the Oort cloud radius, we'll thus have $r_{H,\odot}(M_{l,\odot}) = r_{G,\odot}$ and $r_{H,\odot}(< M_{l,\odot}) < r_{G,\odot}$. Values for $M_{l,\odot}$ are shown in Table 7.4 along with the dimension of the Hill radius and the timescale for the dynamical interaction, $\tau_{D,\odot}$. The scheme of the problem is shown in Figure 7.3 where the first panel represents objects having $r_{H,\odot} < r_{G,\odot}$ and the second panel represents objects having $r_{H,\odot} > r_{G,\odot}$.

We are now in a static situation at which each mass in located at a mean distance $\langle l \rangle(M)$ as discussed in the previous Section. The presence of a limit mass $M_{l,\odot}$ means in this case that the Solar System is currently under gravitational perturbation by objects of mass $M \leq M_{l,\odot}$. We
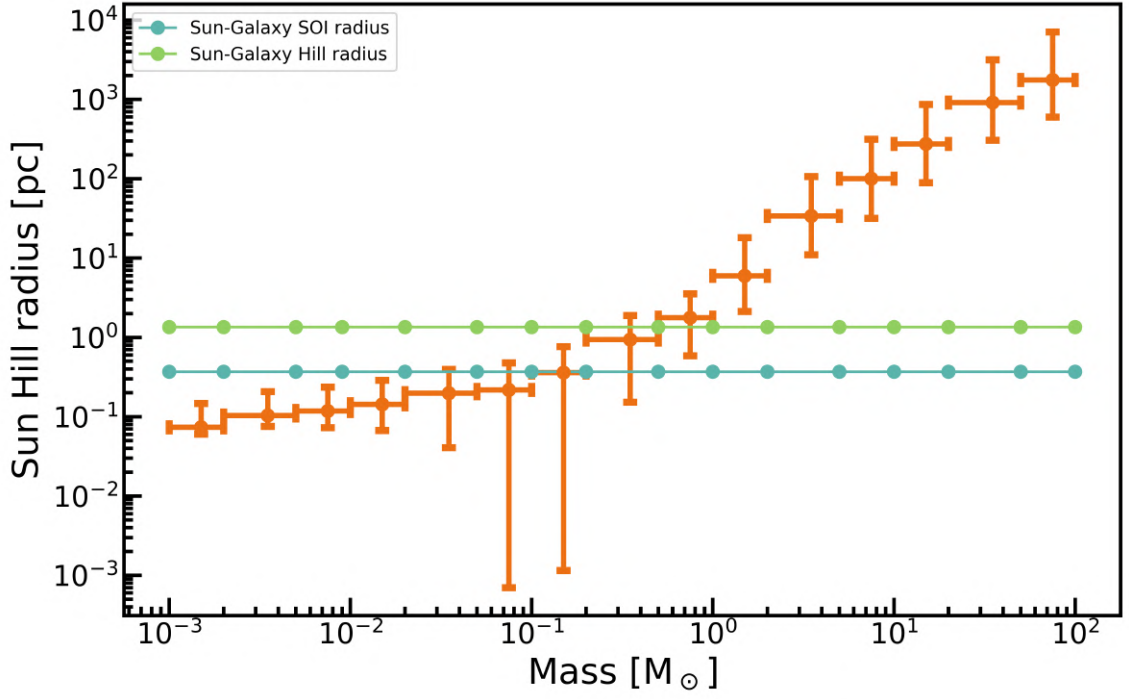
Figure 7.6: The plot shows the comparison between the Hill radius of the Sun with respect near stars and the Hill radius between the Sun and the Galaxy calculated using the main model for PDMF and showing the upper and lower boundary.

can evaluate the timescale, $\tau_{D,\odot}$ of this interaction considering the stars moving at the velocity v (5.38). This interaction has begun at $r_{G,\odot}$ and will last until the star Hill sphere will fully cross the Sun-Galaxy Hill sphere, so the total distance, d_* the star has to travel is:

$$d_* = r_{H,*} + r_{G,\odot} \tag{7.8}$$

and the timescale will be:

$$\tau_{D,\odot} = \frac{2d_*}{v} \quad . \tag{7.9}$$

This timescale is suitable also in the case $M > M_{l,\odot}$ with the difference that in this case the interaction will begin only after the star has travelled a distance:

$$d_T = \langle l \rangle (M) - (r_{G,\odot} + r_{H,*}) \quad . \tag{7.10}$$

88
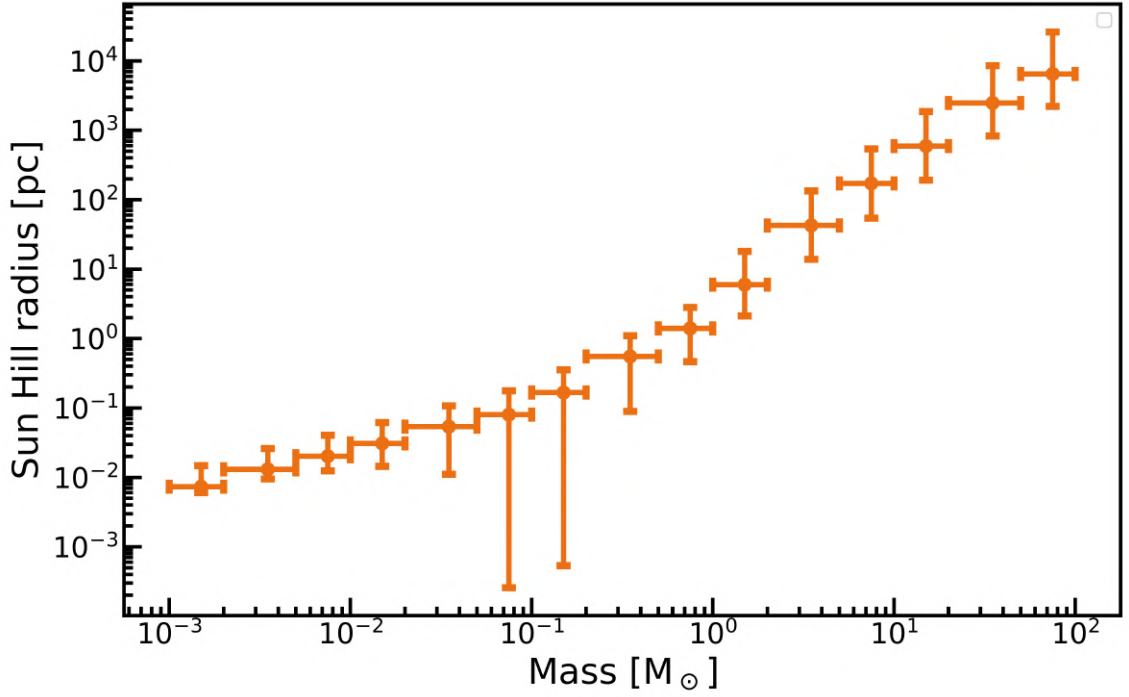
Figure 7.7: Hill radius of a star with respect to the Sun calculated using main model PDMF. Vertical bars represent upper and lower boundary.

7.4 Sun action onto near stars.

Assuming that other stars have systems of orbiting objects similar to the Solar System, the Sun could thus perturb alien Oort clouds as well as other stars perturb ours. In the previous Section we showed that mainly low mass stars perturb the Oort cloud but the calculation could be made also to establish if the Sun has some perturbative effect onto near stars. Indeed, the situation is not exactly symmetric to what previously discussed in Subsection 7.3.1 as in this case we must deal with the Hill radius of the star with respect to the Galaxy, $r_{G,*}$, which changes with the star mass. We thus want to know whether a star of mass M, which is at a distance $\langle l \rangle > (M)$ (7.2) from the Sun, can feel the gravitational presence of the Sun. The Hill radius of the star with respect to the Sun will then be, making use of (6.25):

$$r_{H,*} = P_1 \langle l \rangle > (M) \tag{7.11}$$

while the Sun's Hill radius will be:

$$r_{H,\odot} = \langle l \rangle > (M)[1 - P_1] \quad . \tag{7.12}$$

	$M_{l,*}$ [$M_\odot$]	$r_{G,*}$ [pc]	$r_{H,\odot}$ [pc]	$\tau_{D,*}$ [yr]
Upper boundary	0.45	0.72	1.1	$3.2 \cdot 10^5$
Model	0.45	0.72	1.0	$3.2 \cdot 10^5$
Lower boundary	0.85	0.90	0.98	$3.0 \cdot 10^5$

Table 7.5: In this Table is shown the limit mass $M_{l,*}$ under which the star feels the gravitational effect of the Sun along with its Hill radius value and the dynamical timescale.

For the interaction to be efficient, the Hill radius of the star $r_{H,*}$ has to be lower than the Hill radius of the star with respect to the Galaxy $r_{G,*}$ which has been calculated in Section 6.4 and shown in 6.9:

$$r_{H,*} < r_{G,*} \tag{7.13}$$

when this happens, the interaction between the Sun and the star becomes effective and the Sun is able to interact and possibly perturb or strip objects that lie in $r_{H,*} < r < r_{G,*}$. The relation between the Star-Galaxy Hill radius and the stellar one are shown in Figure 7.8 while the values $r_{H,*}$ and $r_{H,\odot}$ are the same as in Figures 7.6, and 7.7. From these plots we can evaluate which is the mass limit $M_{l,*}$ at which the Solar gravitational perturbation is effective. Results are shown in Table 7.5. In this Table are reported the three values for the main model and its upper and lower boundary. Along with the limit mass is shown the Hill radius for the star and the timescale, $\tau_{D,*}$ for the dynamical interaction to happen:

$$\tau_{D,*} = \frac{2\left(r_{G,*} + r_{H,\odot}\right)}{v} \tag{7.14}$$

where v is the velocity (5.38). This timescale is shown in Figure 7.9. Comparing the results with ones from the previous Section, 7.4, we can see that this timescale is similar to (7.9) with the difference that in (7.14) both $r_{G,*}$ and $r_{H,\odot}$ are changing with the mass of the star while in (7.9) $r_{H,*}$ is the one changing while $r_{G,\odot}$ is fixed. The difference between the two situations is in the interaction distance which depends on different variables in the two cases and thus leads to two different values for M_l.

7.5 Assessing our model results

This thesis work highlighted some interesting aspects on the interactions in the Solar neighbourhood. The main results we got point out two different kinds of interactions, one which is a sort of indirect interaction in the case of SNII and the other one which is dynamical and includes low
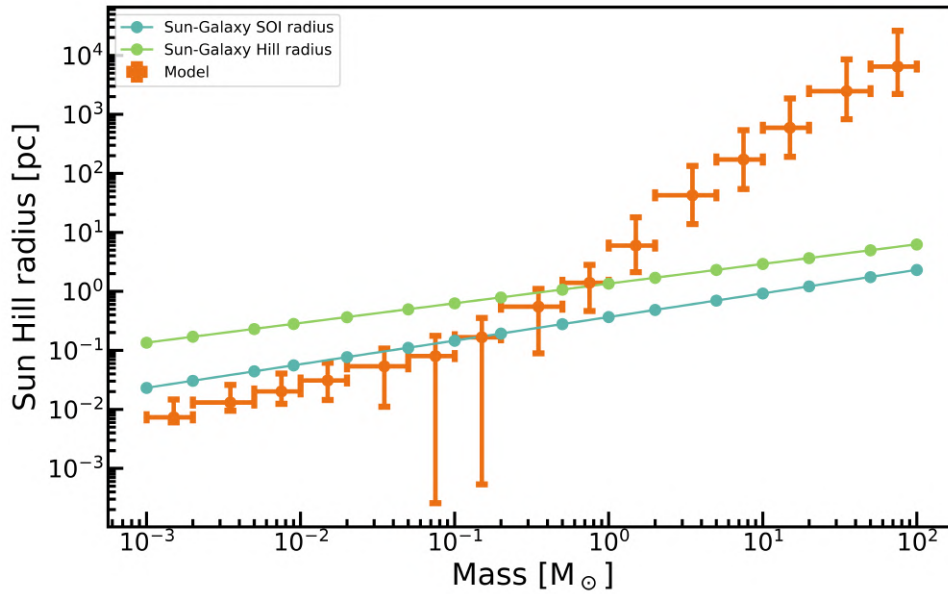
Figure 7.8: Hill radius of a star with respect to the Galaxy (i.e. the alien Oort cloud) calculated for the chosen PDMF model (orange dots). Green dots represent the Hill radius of the star calculated with respect to the Galaxy while blue dots represent the SOI radius calculated with respect to the Galaxy.
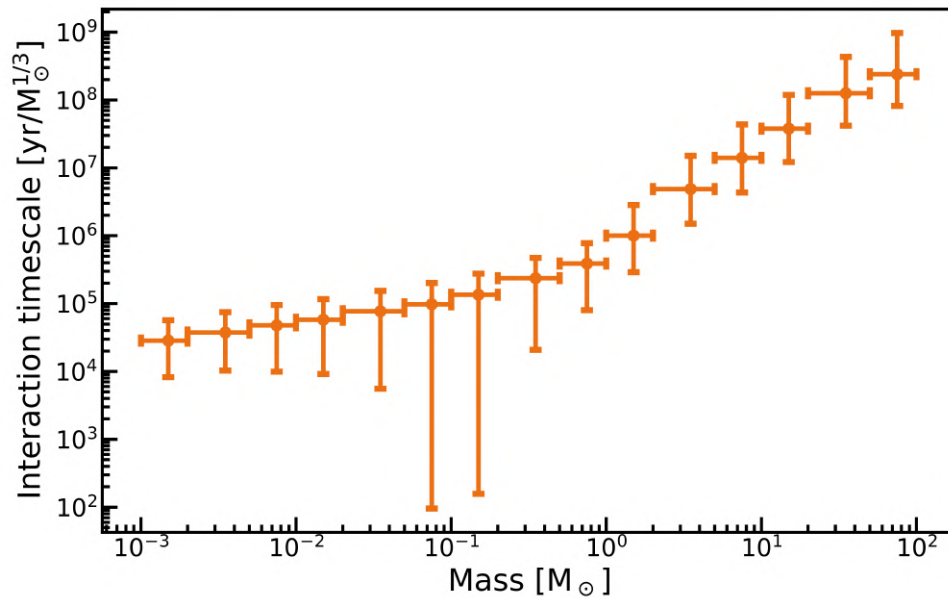
Figure 7.9: In this plots is shown the timescale (7.14) for the model of PDMF taken into account along with timescale value for the upper and lower boundary models.

mass stars.

The PDMF gives us a scale number of high mass stars which is significantly lower than the number of Sun-like objects or lower mass objects and the theory of the LSR sets a mean velocity for stars in the Solar neighbourhood that we chose as 5.38. Furthermore, our calculations in Section 7.2 and Section 7.3 show that high mass stars should reside sufficiently far from the Sun to not have recurring dynamical interactions with it but, considering that high mass stars have a lifetime very short with respect to low mass stars, we found that stars having mass $M \gtrsim 9.0\,\mathrm{M_\odot}$ could probably explode as SNII in the Solar proximity investing the Solar System with the estimated minimum flux we calculated in Table 7.3.

Another aspect that arises from our results is that the Sun with its Solar System is not wandering alone along the Galaxy, instead there seems to be a constant dynamical interplay between our Solar System and, mainly, low mass objects in its proximity. This is possible since, according to our models and calculations, there is a large amount of low mass objects, thus having a much higher object density with respect to high mass stars which make it easier to find low mass objects near the Sun. In Section 7.3 our results show that $M_{l,\odot}$ can be treated as an upper limit for stars that are currently able to perturb our Solar System. To know how deep into the Solar System this kind of interactions are we must compare the dimension of the perturbing star Hill radius, $r_{G,*}$ with the Sun-Galaxy Hill radius, $r_{G,\odot}$, and the mutual distance between the star and the Sun, $\langle l \rangle$. The length of the perturbed zone will then be given by:

$$ r = r_{H,*} + r_{G,\odot} - \langle l \rangle \quad , \tag{7.15} $$

in this case the full perturbed zone belongs to the Solar System and is thought to be for most companion stars a portion of the Oort cloud. In this section we also calculated the duration of this interaction which is variable with the star mass, and thus, Hill radius.

We made the same but opposite calculation to see what kind of stars are perturbed by our Sun in Section 7.4 and our results gave the upper limit mass $M_{l,*}$, lower than the previous case. If we now put together this two results we can actually see that stars of mass $M < M_{l,*}$ both can perturb the Sun and be perturbed by it. In Figure 7.10 is depicted the $M_{l,*} = 0.45\,\mathrm{M_\odot}$ star in its static interaction with the Sun. In this particular case we do not mind anymore of the two Hill radii values as the two Hill radii of star and Sun with respect to the Galaxy become relevant and, most importantly, cross each other generating a sort of merging zone between the Solar System Oort cloud and the alien Oort cloud of the star in which there could be an exchange of objects between the two. This situation closely resembles the Roche lobe filling of a binary system, although in our case mimicked on a statistical basis.

Finally, we can further investigate the effects of stars onto the Solar System (and vice versa) by
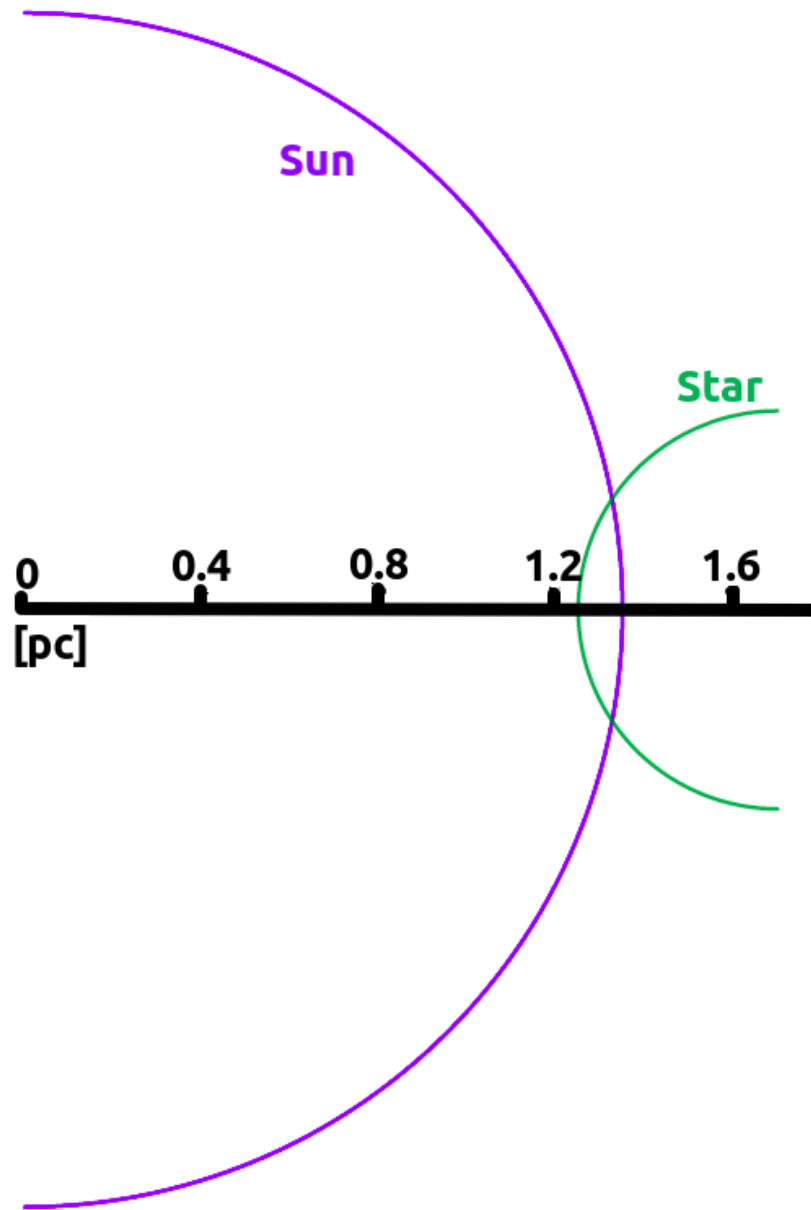
Figure 7.10: Sketch of the interaction between a star of $M_{l,*} = 0.45\,\mathrm{M}_\odot$ and the Sun.
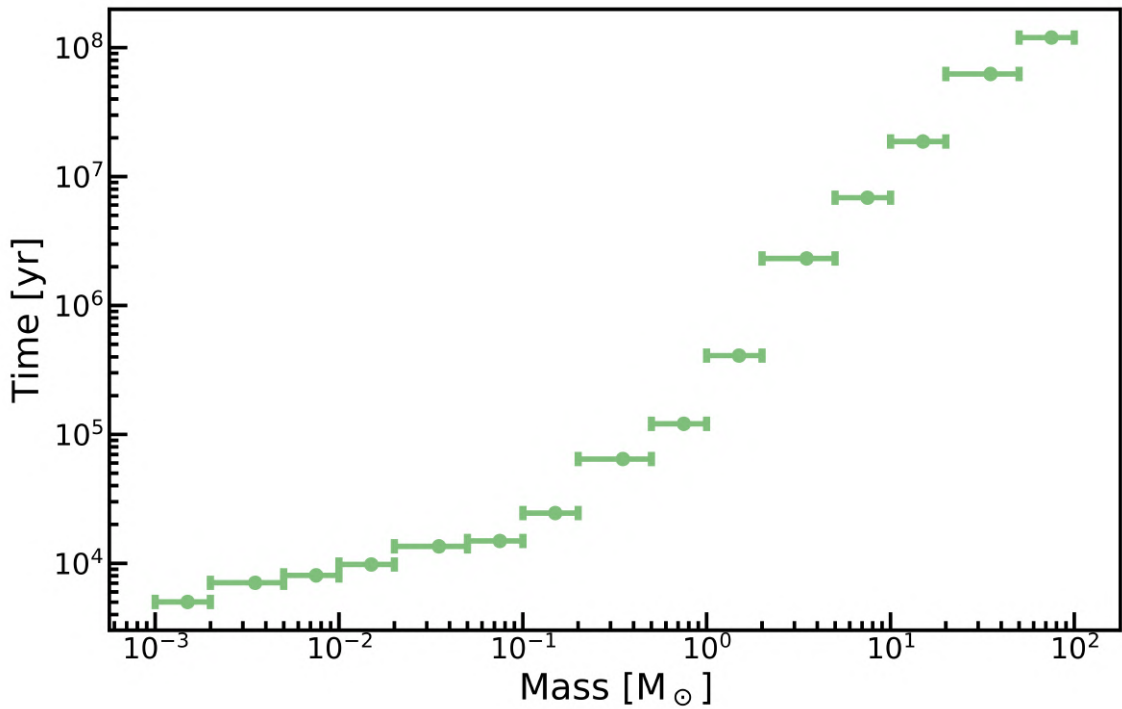
Figure 7.11: Expected time between deep perturbations onto planet orbits caused by a passing star. For low mass objects can apparently perturb the Solar System once every 10^3 yr.

asking us if it is possible that some star could perturb deep enough to make some effects onto the planets orbit. From our calculations there is no current effect onto planets but there could have been some in the past or it can happen in the future. We used for our calculation the radius of the heliopause which is slightly higher than the radii of planets orbits but can still well represent them. We found that this type of perturbation could more probably be made by low mass stars once every few 10^3 yr and that should last about 10^4 yr assuming this type of stars. We plotted time, frequency and duration of the interactions as shown in Figures 7.11, 7.12, and 7.13 which depict the dependence from the star mass.
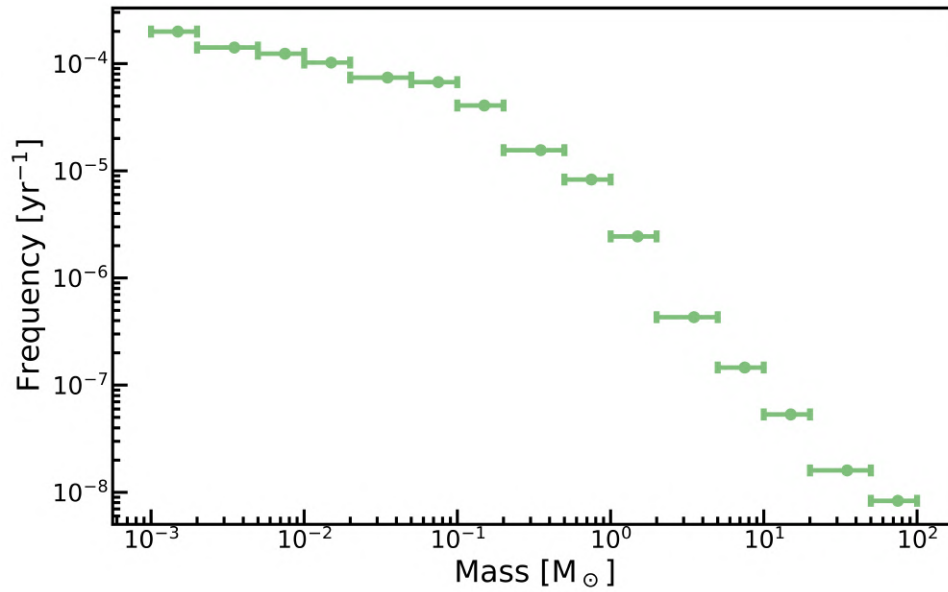
Figure 7.12: Frequency of possible planet orbits perturbation on the Solar System calculated using the velocity (5.38) and the difference between the Hill radius of the star with respect to the Sun and the position of the heliopause.
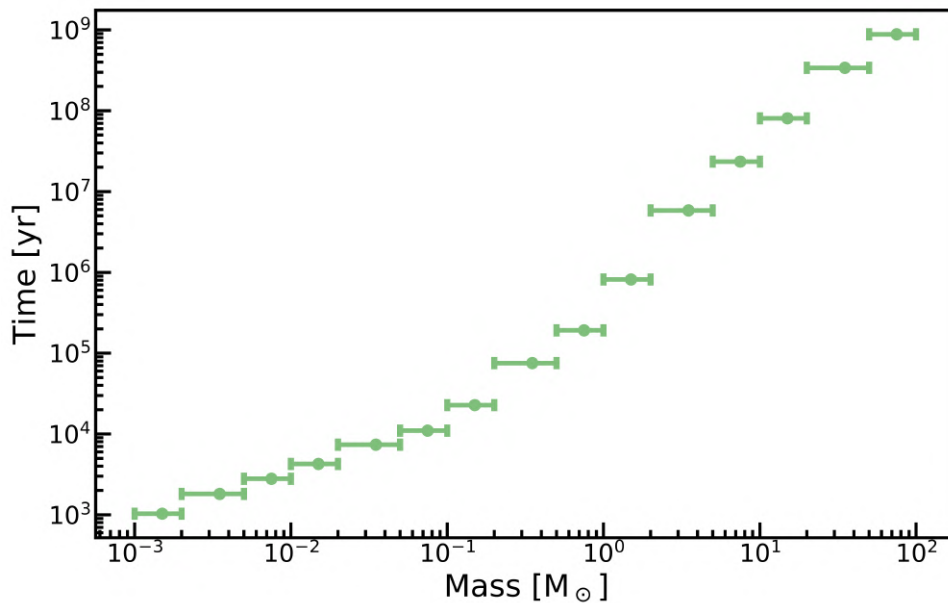
Figure 7.13: Duration of a planet orbit perturbation caused by a passing star, calculated as the sum of the Hill radius of the star with respect to the Sun and the heliopause radius by the velocity 5.38.

NB_OBJ	Object Name	Object Type	Distance [pc]	Mass [M$_\odot$]	$r_{G,*}$ [pc]	$r_{H,*}$ [pc]	$r_{H,\odot}$ [pc]	Spectral Type
1	Proxima Cen	LM	1.30	0.123	0.590	0.870	0.432	M5.5
3	alf Cen A	Star	1.35	1.00	1.19	0.673	0.673	G2
4	alf Cen B	Star	1.35	0.860	1.13	0.690	0.656	K1
5	Barnard's Star	LM	1.83	0.270	0.767	1.11	0.718	M3.5
6	Luhman 16 A	BD	1.99	0.070	0.489	1.41	0.582	L7.5
7	Luhman 16 B	BD	1.99	0.070	0.489	1.41	0.582	T0.5
8	WISEA J085510.74-071442.5	BD	2.28	0.070	0.489	1.61	0.665	>Y4
9	Wolf 359	LM	2.41	0.102	0.554	1.64	0.767	M6
10	HD 95735	LM	2.55	0.470	0.923	1.43	1.11	M1.5
12	alf CMa A	Star	2.64	2.05	1.51	1.16	1.48	A1
14	G 272-61 A	LM	2.72	0.162	0.647	1.76	0.959	M5
15	G 272-61 B	LM	2.67	0.102	0.554	1.82	0.852	M6
16	Ross 154	LM	2.98	0.270	0.767	1.81	1.17	M3.5

Table 7.6: In this Table are shown the first 14 objects from the catalogue given by Reylé, C. et al. 2021 ordered by distance from the Sun. All the objects reside within 3 pc from the Sun and for each object is reported its name, object type, distance, mass, object-Galaxy Hill radius $r_{G,*}$, object-Sun Hill radius $r_{H,*}$, Sun-object Hill radius $r_{H,\odot}$, and spectral type.

One last observation can be done on the data we used in Chapter 4. In Table 7.6 we took from data given by Reylé, C. et al. 2021 the first 14 objects (stars, low mass stars or brown dwarfs) which lie within 3 pc from the Sun. In the Table is reported along with the identification information also the parallax and the distance in pc, its mass and the three possible Hill radius calculations. Comparing these values with the Hill radius of the Sun with respect to the Galaxy we find confirmation of our results in five objects of this sample. The objects are the first four of the list (Proxima Centauri, α Centauri A, α Centauri B, and Barnard's Star) and the star α Canis Majoris A, commonly known as Sirius A. This last object is an exception as our models predicts that this kind of objects should reside most probably at a mean distance of $\sim$ 50 pc, indeed its Hill radius with respect to the Galaxy will be higher than the other stars having nearly the same distance, thus this star will be able to both perturb the Solar System Oort cloud and be perturbed by the Sun. As Sirius A also α Centauri A and α Centauri B are more near than the expectations of our model. This feature makes thus possible the interaction between these stars and the Sun. Proxima Centauri and Barnard's Star are instead in good agreement with our calculations having a mass under the limit mass we found in Section 7.4. In Figure 7.14 is represented the described interactions between the Solar System Oort cloud and Oort clouds of the stars in its surroundings according to data in Table while in Figure 7.15 are plotted along with the Sun Oort cloud, the Hill radius of the stars calculated with respect to the Sun. While the first plot shows that only 5 objects are currently merging their Oort clouds with the Solar System one, this latter plot shows that the Oort cloud is also under the perturbative effect of almost all the stars within 3 pc. We thus made the plot in Figure 7.16 to understand the effect of the Sun onto near stars of the sample. Orange dots represent the Star-Sun Hill radius and green triangles represent the position of the alien Oort cloud, i.e. the Star-Galaxy Hill radius. From this plot we can see that stars having mass higher than 5 $M_\odot$ are currently perturbed by the Sun. We then plotted also the situation of Figure 7.15 in Figure 7.17 in which the purple dots represent the Hill radius of the Sun with respect to the star and the triangles mark the position of the Solar System Oort cloud. As suggested by Figure 7.15 the Solar System Oort cloud is currently under the perturbation of all the stars of Table 7.6 except α Canis Majoris A.
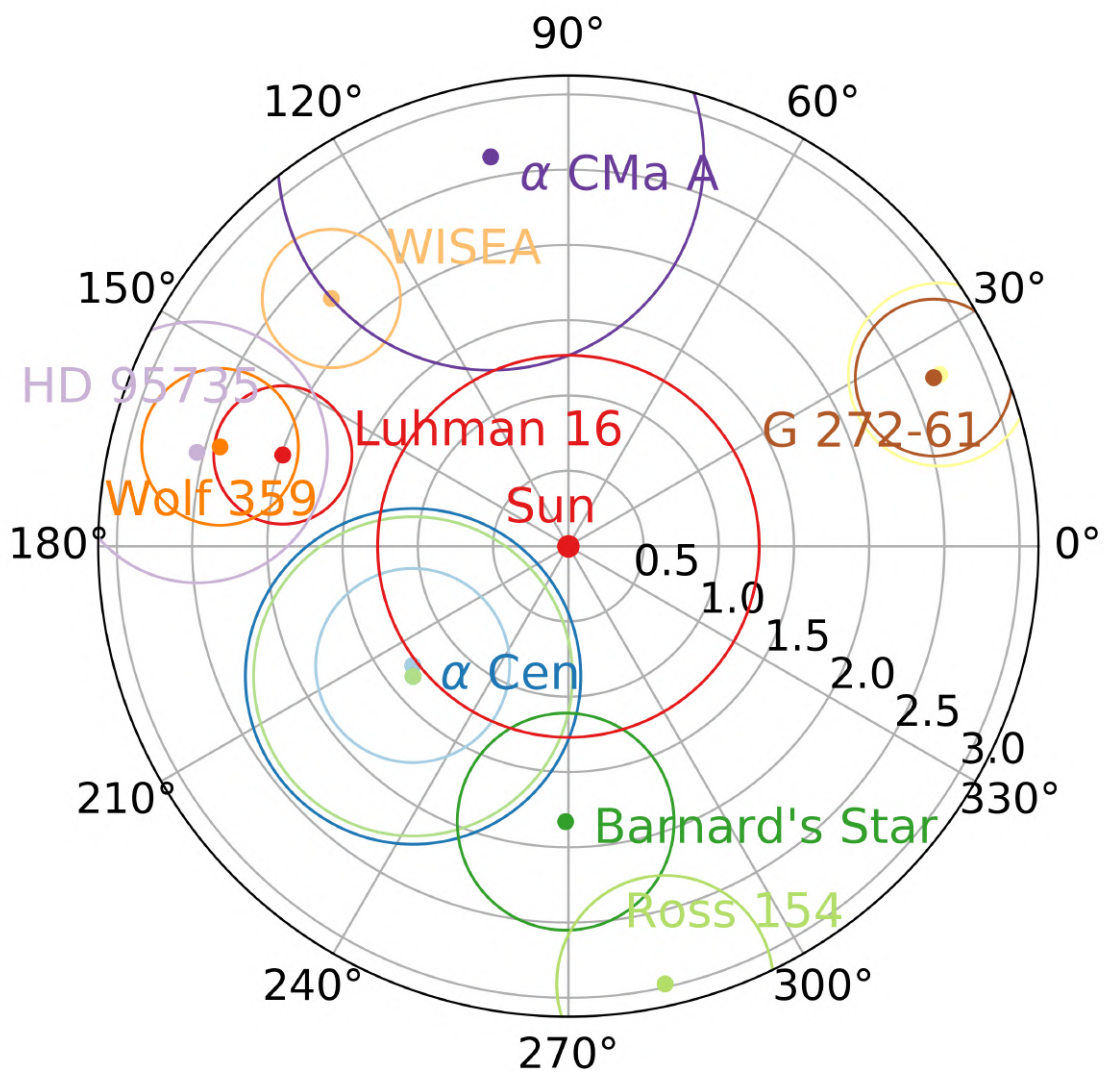
Figure 7.14: Plot of the stars within 3 pc from the Sun in RA and distance from the Solar System coordinates. The position of the Sun is plotted along with the position of its Oort cloud ($r_{G,\odot}$). The other stars position are taken from the catalogue given by Reylé, C. et al. 2021 and for each star is plotted the calculated alien Oort cloud ($r_{G,*}$). This plot highlights the five current mergings between the Solar System Oort cloud and alien Oort clouds.
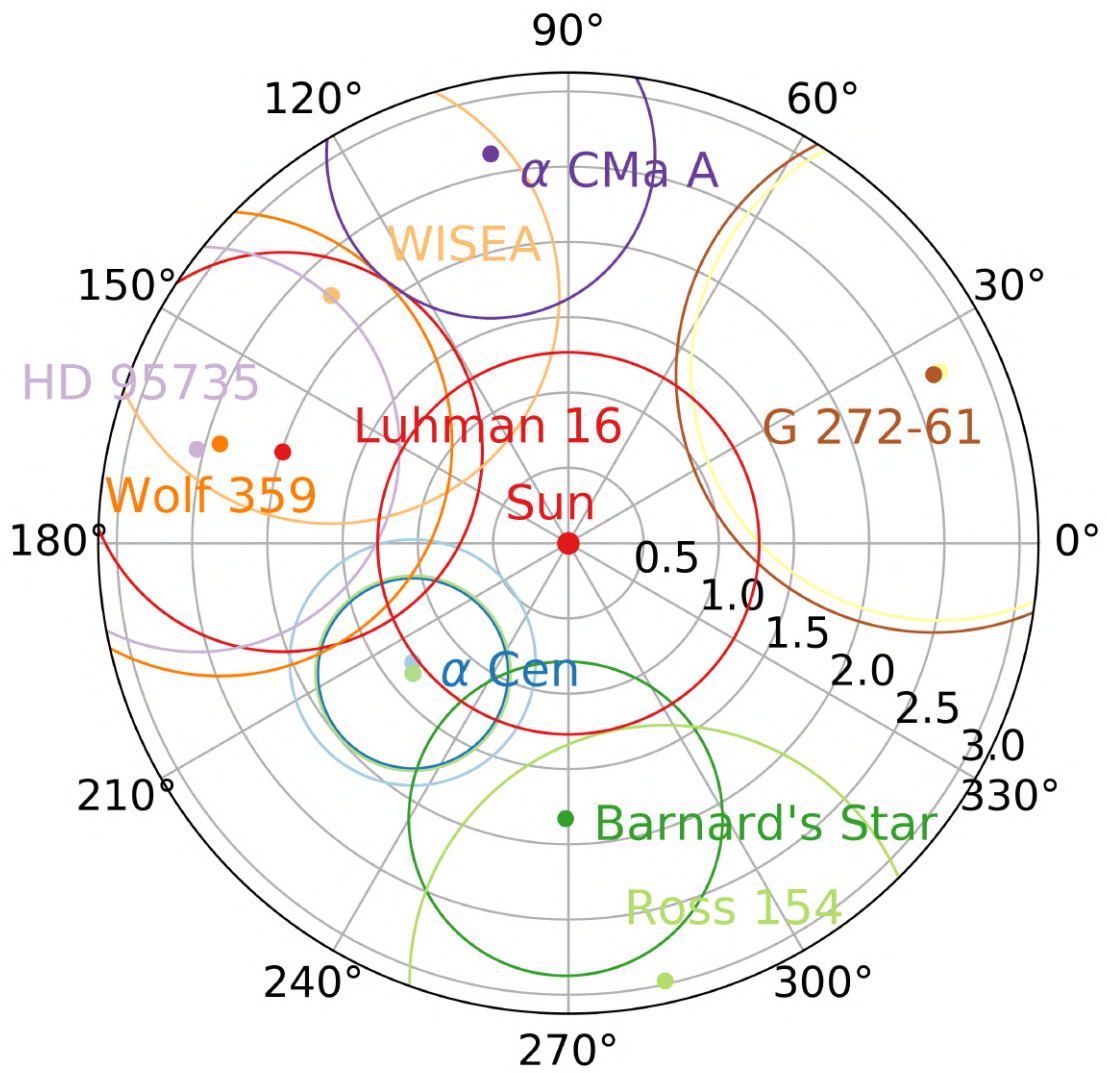
Figure 7.15: Position of the *13* objects listed in Table *7.6* with respect to the Sun. As Figure *7.14* the coordinates as RA and distance from the Sun. For the Sun is plotted the Solar System Oort cloud while for the stars is plotted the star Hill radius with respect to the Sun. This plot evidences that almost all the reported stars are currently interacting with the Solar System Oort cloud.
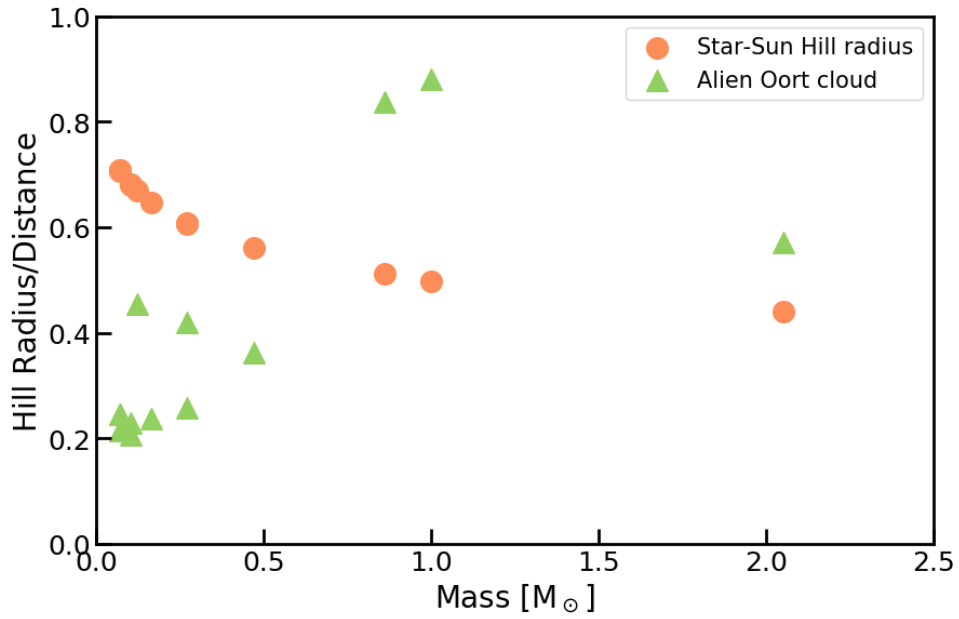
Figure 7.16: Star-Sun Hill radius is plotted along with its alien Oort cloud for each star of Table 7.6. All the quantities are expressed as a fraction of the distance between the star and the Sun. There is evidence of interaction for stars having mass $M > 0.5\,\mathrm{M}_\odot$.
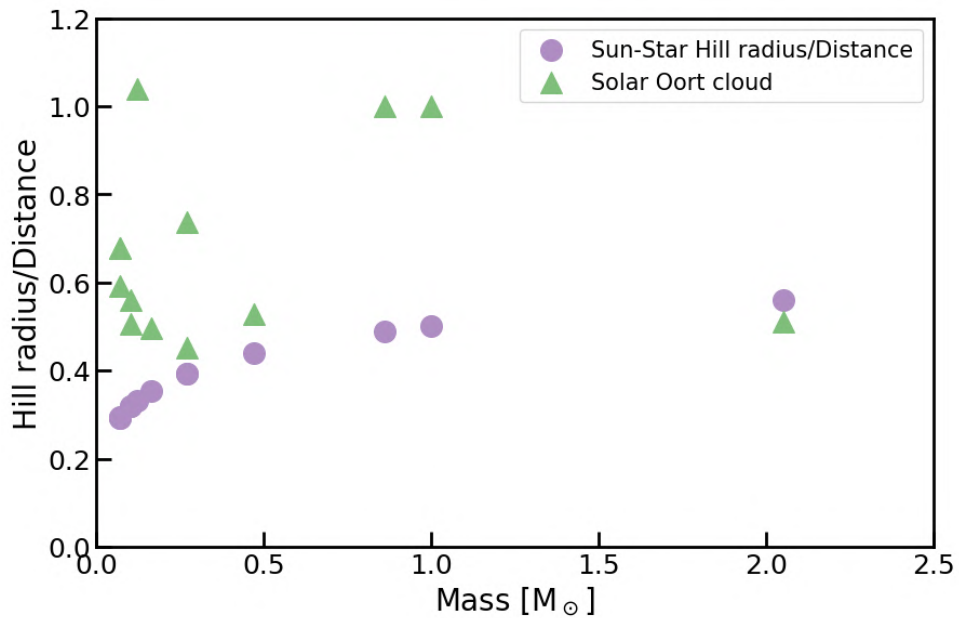
Figure 7.17: The Solar System Oort cloud (green triangles) is shown against the Sun-Star Hill radius (violet points). We can assert that the Solar System Oort cloud is under perturbation by a star if the Sun-star Hill radius has a lower value with respect to the Solar System Oort cloud radius (i.e. the Sun-Galaxy Hill radius).

Chapter 8

Conclusions and future perspectives

This thesis work started from the simple yet deep question:

"How the interaction between the Sun and other stars in its surroundings
would affect the Solar System?"

Trying to give an adequate answer we modelled the Milky Way in order to be able to know how is populated, in terms of star density and distribution, the local neighbourhood. The results of this modelling along with local kinematics and three-body dynamics allowed us to obtain the results we shown in the previous Chapter.

In Chapter 2 we modelled the Milky Way stellar profile starting from an observable quantity which is the Oort density discussed in Section 2.3. We then adopted a stellar density function from Jurić et al. 2008 which describes the Galaxy thin disk, thick disk, and halo. The stellar density function has been thus normalized to the chosen Oort density in order to model local Galaxy to be representative of the actual local environment. To have the correct mass distribution along star classes we introduced three IMF candidates in Section 2.5 with a study on the low mass end of the Salpeter IMF (Subsection 2.5.1) in Subsection 2.5.4 which highlighted the diverging behaviour of it and led us to make an analogy with the Solar System and choose to keep the function constant for masses $M < 0.1\,\mathrm{M}_\odot$. The last Section 2.6 presents four different types of SFR functions which have been used to characterize the current local distribution and amount of stars. To do this, we normalized the SFR function to the local mean density.

In Chapter 3 we discussed of some fundamentals of stellar evolution and in Section 3.3 implemented a stellar lifetime function adopted from Buzzoni 2002 which has been used to compute the PDMF in the subsequent Section 3.4. The PDMF models have been thus normalized to the local mean density to be consistent with observations and in subsequent Sections we made some calculations upon the remnants mass and numbers.

The Chapter 4 has been then dedicated to the comparison between the predicted number of objects from our models and the latest Gaia EDR3 data.

In Chapter 5 we described the local kinematics with a description of the Milky Way rotation curve in Section 5.3 in keplerian approximation and the Oort constants in the subsequent Section 5.4.

In this Section we also computed and presented the rotation curve obtained from the mass integration of our density profile. The last step of this Chapter has been the definition of the LSR and a comparison between some reported values. We thus chose to mean over these values to obtain a reference velocity to employ in the results calculation.

In Chapter 6 we studied the reduced three-body problem and defined the Hill and SOI radii. In section 6.6 we thus gave some reference values and made a discussion over the Solar System edge definition.

Lastly our results have been discussed in Chapter 7. We found a possible near-Sun source of high energy radiation in high mass stars flybys, finding that a passing star having a mass higher than $9\,M_\odot$ could have exploded as a SNII and invested the Solar System with the X-ray flux reported in Table 7.3. This result could be further investigated for example to know if this flux could be potentially harmful (or even deadly to some species) or if it could have some responsibility in the developing of life on Earth basing on the quantity of radiation absorbed by a body.

We found that our Solar System is currently under perturbation by near low mass stars of $M < 0.5$ $M_\odot$. The presence of these kind of bodies could perturb the orbit of a comet that resides in the Oort cloud and turn it into a LPC as described in Subsection 6.6.1, otherwise, the comet could be stripped by the perturbing star. We also found that also our Sun is perturbing near low mass stars having $M < 0.45\,M_\odot$. Since stars having this mass are expected to perturb the Oort cloud too, our results suggest that there could exist a merging zone between our Oort cloud and alien Oort clouds, in which comets of both the clouds can be mixed. Finally, we found that there is a possibility that planets could be affected by the presence of a star for a relatively short period of time. This aspect could be investigated to calculate how much this kind of interaction is relevant for the Solar System structure stability.

An interesting possible future investigation could aim at making the calculations reported in this thesis in a denser environment as could be spiral arms. In this case we expect higher values for the PDMF since it is normalized to the local surface density, and, since star formation in spiral galaxies resides in spiral arms, a changing in its high mass end shape with an increase in the number of high mass stars. This feature should lead to close encounters to be more frequent reflecting maybe in more frequent comet showers, deeper interactions, or object stripping.

Appendix A

Gaia Data.

In Table A.1 the nearest 10 pc objects detected by Gaia satellite are reported as used in Reylé, C. et al. 2021. For each object is specified its category (Star, Low Mass star, Brown Dwarf, or Planet), its spectral type, possible exoplanet associated, and its Simbad name. Objects order is by distance.

NB_OBJ	DISTANCE [pc]	OBJ_CAT	SP_TYPE	EXO_COUNT	SIMBAD_NAME
1	1.30	LM	M5.5	1	alf Cen C
2	1.30	Planet			
3	1.34	Star	G2		alf Cen A
4	1.34	Star	K1		alf Cen B
5	1.82	LM	M3.5		Barnard's Star
6	1.99	BD	L7.5		Luhman 16A
7	1.99	BD	T0.5		Luhman 16B
8	2.27	BD	>Y4		WISEA J085510.74-071442.5
9	2.40	LM	M6		Wolf 359
10	2.54	LM	M1.5e	1	HD 95735
11	2.54	Planet			
12	2.63	Star	A1		alf CMa A
13	2.67	WD	DA1.9		alf CMa B
14	2.67	LM	M5		G 272-61A
15	2.71	LM	M6		G 272-61B
16	2.97	LM	M3.5e		Ross 154
17	3.15	LM	M5		Ross 248
18	3.21	Star	K2	1	eps Eri
19	3.21	Planet			
20	3.28	LM	M2	2	HD 217987
21	3.28	Planet			
22	3.28	Planet			
23	3.37	LM	M4	1	Ross 128
24	3.37	Planet			
25	3.40	LM	M5		GJ 866 A
26	3.40	LM?			GJ 866 B
27	3.40	LM?			GJ 866 C
28	3.49	Star	K5		61 Cyg A
29	3.49	Star	K7		61 Cyg B

NB_OBJ	DISTANCE [pc]	OBJ_CAT	SP_TYPE	EXO_COUNT	SIMBAD_NAME
30	3.51	Star	F5		alf CMi A
31	3.51	WD	DQZ		alf CMi B
32	3.52	LM	M3		HD 173739
33	3.52	LM	M3.5		HD 173740
34	3.56	LM	M1	2	GJ 15 A
35	3.56	Planet			
36	3.56	Planet			
37	3.56	LM	M3.5e		GJ 15 B
38	3.58	LM	M6.5		G 51-15
39	3.63	Star	K5	1	GJ 845 A
40	3.63	Planet			
41	3.65	BD	T1		GJ 845 B
42	3.67	BD	T6		GJ 845 C
43	3.67	Star	G8.5		tau Cet
44	3.67	LM	M5.5	3	L 372-58
45	3.67	Planet			
46	3.69	Planet			
47	3.69	Planet			
48	3.71	LM	M4e	3	YZ Cet
49	3.71	Planet			
50	3.71	Planet			
51	3.71	Planet			
52	3.78	LM	M3.5	2	BD+05 1668
53	3.78	Planet			
54	3.78	Planet			
55	3.83	LM	M6	2	Teegarden's Star
56	3.83	Planet			
57	3.83	Planet			
58	3.93	LM	sdM1		Kapteyn's Star
59	3.96	LM	M1		AX Mic
60	4.00	LM	M3		HD 239960A
61	4.00	LM	M4		HD 239960B
62	4.00	LM	M8		SCR J1845-6357
63	4.00	BD	T6		SCR J1845-6357B
64	4.04	LM	M9		DENIS J104814.6-395606
65	4.11	LM	M4.5		Ross 614 A
66	4.11	LM	M5.5		Ross 614 B
67	4.11	BD	> T9		UGPS J072227.51-054031.2
68	4.30	LM	M3	3	BD-12 4523
69	4.30	Planet			
70	4.30	Planet			
71	4.30	Planet			
72	4.31	WD	DZ		Wolf 28
73	4.32	LM	M5.5		Wolf 424
74	4.34	LM	M7		Wolf 424
75	4.46	LM	M2		HD 225213
76	4.46	LM	M4.5	2	TZ Ari
77	4.46	Planet			
78	4.47	Planet			
79	4.54	LM	M3	1	BD+68 946
80	4.54	Planet			

NB_OBJ	DISTANCE [pc]	OBJ_CAT	SP_TYPE	EXO_COUNT	SIMBAD_NAME
81	4.55	LM	M2	1	CD-46 11540
82	4.55	Planet			
83	4.55	BD	Yopec		WISE J163940.83-684738.6
84	4.55	LM	M6.5		LP 731-58
85	4.63	WD	DQ		LAWD 37
86	4.66	LM	M5.5		GJ 1245 A
87	4.66	LM	M8		GJ 1245 C
88	4.67	LM	M5.5		GJ 1245 B
89	4.67	BD	T9		WISEP J174124.25+255319.5
90	4.67	LM	M4	4	BD-15 6290
91	4.67	Planet			
92	4.67	Planet			
93	4.69	Planet			
94	4.69	Planet			
95	4.83	LM	M5.5		L 143-23
96	4.84	LM	M5.5		G 158-27
97	4.86	BD	L9		DENIS J025503.3-470049
98	4.87	Star	K7.5e		HD 88230
99	4.90	LM	M1		BD+44 2051
100	4.90	LM	M5.5		BD+44 2051B
101	4.96	LM	M3		BD+20 2465
102	4.96	LM	M1.5	2	HD 204961
103	4.96	Planet			
104	4.96	Planet			
105	5.00	LM	M5	2	CD-44 11909
106	5.00	Planet			
107	5.00	Planet			
108	5.00	Star	K0.5		GJ 166 A
109	5.00	WD	DA2.9		GJ 166 B
110	5.01	LM	M4.5		GJ 166 C
111	5.05	LM	M4		EV Lac
112	5.09	LM	M7		G 9-38 A
113	5.10	LM	M7		G 9-38 B
114	5.11	Star	K0		70 Oph A
115	5.12	Star	K4		70 Oph B
116	5.15	Star	A7		alf Aql
117	5.15	BD	T6		2MASS J15065257+7027247
118	5.20	LM	M3.5e		G 99-49
119	5.21	BD	T6		2MASS J08173001-6155158
120	5.25	LM	M4e		G 254-29
121	5.32	LM	M6.5		WISEA J154045.67-510139.3
122	5.33	BD	T8		2MASS J09393548-2448279
123	5.37	LM	M4e	2	LP 656-38
124	5.37	Planet			
125	5.37	Planet			
126	5.43	LM	M1.5		HD 119850

NB_OBJ	DISTANCE [pc]	OBJ_CAT	SP_TYPE	EXO_COUNT	SIMBAD_NAME
127	5.51	LM	M4e		GJ 169.1 A
128	5.51	WD	DC		GJ 169.1 B
129	5.58	BD	T7.5		2MASS J11145133-2618235
130	5.58	LM	M3	1	HD 265866
131	5.58	Planet			
132	5.62	LM	M4		LP 816-60
133	5.66	BD	Y1		WISE J035000.32-565830.2
134	5.68	LM	M8.5		2MASSI J1835379+325954
135	5.70	LM	M1.5		HD 36395
136	5.70	BD	T8		2MASSI J0415195-093506
137	5.76	LM	M1	2	HD 42581
138	5.76	Planet			
139	5.76	Planet			
140	5.76	BD	T7pec		HD 42581B
141	5.77	Star	G9		sig Dra
142	5.79	LM	M4		Ross 47
143	5.88	Star	K4		GJ 570 A
144	5.88	LM	M1		GJ 570 B
145	5.90	LM?			GJ 570 C
146	5.90	BD	T7		GJ 570 D
147	5.90	LM	M4		L 205-128
148	5.91	LM	M4.5		L 347-14
149	5.91	LM	M1		BR Psc
150	5.91	LM	M3	1	GJ 752 A
151	5.91	Planet			
152	5.92	LM	M8		GJ 752 B
153	5.92	LM	M2.5		CD-40 9712
154	5.92	Star	F9		eta Cas A
155	5.92	Star	K7e		eta Cas B
156	5.94	Star	K2		36 Oph A
157	5.95	Star	K1		36 Oph B
158	5.95	Star	K5		36 Oph C
159	5.97	LM	M3		GJ 661
160	5.97	LM?			GJ 661
161	5.98	LM	M4e		YZ CMi
162	5.99	BD	Y0.5		WISE J154151.65-225024.9
163	6.00	LM	M4		G 158-50
164	6.00	LM	M4		G 158-50
165	6.01	Star	K2.5		GJ 783 A
166	6.01	LM	M3.5		GJ 783 B
167	6.04	Star	G8	2	e Eri
168	6.04	Planet			
169	6.04	Planet			
170	6.05	LM	M5e		GJ 268 A
171	6.05	LM	M5e		GJ 268 B
172	6.09	Star	G8		del Pav
173	6.11	BD	T2		SIMP J013656.5+093347.3

NB_OBJ	DISTANCE [pc]	OBJ_CAT	SP_TYPE	EXO_COUNT	SIMBAD_NAME
174	6.14	BD	T7		2MASSI J0937347+293142
175	6.16	LM	M0		HD 191849
176	6.18	BD	Y0		WISE J220905.73+271143.9
177	6.21	WD	DQ9P		EGGR 372
178	6.25	LM	M3.5		BD-11 3759
179	6.25	LM	M3.5e		BD+19 5116 A
180	6.26	LM	M4e		BD+19 5116 B
181	6.30	LM	M3	3	BD-07 4003
182	6.30	Planet			
183	6.30	Planet			
184	6.30	Planet			
185	6.32	BD	Y0(pec?	)	WISE J140518.39+553421.3
186	6.33	LM	M0		HD 79210
187	6.33	LM	M0	1	HD 79211
188	6.33	Planet			
189	6.35	LM	M6.5		LP 368-128
190	6.41	BD	T5.5		2MASS J15031961+2525196
191	6.42	LM	M9		LP 944-20
192	6.44	WD	DZ11		EGGR 45
193	6.46	LM	M4.5e		GL Vir
194	6.47	LM	M1.5	1	G 202-48
195	6.47	Planet			
196	6.49	LM	M3e		GJ 644 A
197	6.49	LM?			GJ 644 B
198	6.49	LM?			GJ 644 B
199	6.49	LM	M7		GJ 644 C
200	6.49	LM	M3.5		Wolf 629
201	6.50	LM	M4		L 100-115
202	6.54	Star	K3	4	HD 219134
203	6.54	Planet			
204	6.54	Planet			
205	6.54	Planet			
206	6.54	Planet			
207	6.55	BD	Y0.5		WISEA J082507.37+280548.2
208	6.60	BD	Y0		WISE J041022.71+150248.4
209	6.65	BD	T7.5		2MASS J05212615+1025328
210	6.66	LM	M4		L 471-42
211	6.74	LM	M2.5		Ross 104
212	6.74	Star	G7		ksi Boo A
213	6.75	Star	K5		ksi Boo B
214	6.76	LM	M4.5e		Ross 619
215	6.77	LM	M4e		G 41-14 A
216	6.77	LM?			G 41-14 B
217	6.77	LM?			G 41-14 C
218	6.77	LM	M3e		GJ 829 A
219	6.77	LM?			GJ 829 B

NB_OBJ	DISTANCE [pc]	OBJ_CAT	SP_TYPE	EXO_COUNT	SIMBAD_NAME
220	6.79	LM	M9.5		2MASS J07200325-0846499
221	6.79	BD	T5		2MASS J07200325-0846499
222	6.83	BD	T6		2MASS J19284155+2356016
223	6.84	BD	T8		WISEPA J025409.45+022359.1
224	6.86	LM	M3	1	BD-17 588A
225	6.86	Planet			
226	6.86	LM	M2.5		BD-17 588BC
227	6.86	LM?			BD-17 588BC
228	6.86	LM	M1.5e		HD 216899
229	6.89	BD	sdT8?		2MASS J07584037+3247245
230	6.96	LM	M4		Wolf 358
231	7.03	LM	M2		BD+01 2447
232	7.03	LM	M1e		HD 199305
233	7.04	LM	M4		UCAC4 642-113039
234	7.05	LM	M7e		LP 914-54
235	7.10	BD	Y0		WISE J205628.91+145953.2
236	7.10	LM	M4.5		L 230-188
237	7.12	BD	T8.5		WISE J004945.61+215120.0
238	7.17	LM	M5.5		G 157-77
239	7.22	Star	K3		GJ 105 A
240	7.22	LM	M4		GJ 105 B
241	7.22	LM	M7		GJ 105 C
242	7.22	BD	L6.5		2MASS J08354256-0819237
243	7.23	LM	M4.5e		L 788-34
244	7.24	Star	K3		HD 156384A
245	7.24	Star	K5		HD 156384B
246	7.24	LM	M1.5	2	HD 156384C
247	7.24	Planet			
248	7.24	Planet			
249	7.24	BD	L9		2MASS J06073908+2429574
250	7.37	BD	T8.5		WISEP J031325.96+780744.2
251	7.41	BD	L5.5		2MASSW J1507476-162738
252	7.43	Star	K2.5		HD 4628
253	7.47	Star	G2		bet Hyi
254	7.49	BD	T8		WISE J200050.19+362950.1
255	7.51	LM	M3.5		G 203-47
256	7.51	WD?			G 203-47
257	7.59	Star	A4		alf PsA
258	7.59	Star	K4		alf PsA B
259	7.60	LM	M4e		alf PsA C
260	7.61	Star	G5		GJ 53 A

NB_OBJ	DISTANCE [pc]	OBJ_CAT	SP_TYPE	EXO_COUNT	SIMBAD_NAME
261	7.62	LM	M4?		GJ 53 B
262	7.63	LM	M3		VX Ari
263	7.64	LM	M5		G 141-36
264	7.64	LM	M1e		BD+11 2576
265	7.65	BD	Y0		WISE J173835.53+273259.0
266	7.65	LM	M4.5		G 258-33
267	7.66	Star	K0		107 Psc
268	7.67	BD	Y1		WISEA J235402.79+024014.1
269	7.67	BD	Y1		WISE J081117.81-805141.3
270	7.67	LM	M3		L 499-56
271	7.67	Star	A0		alf Lyr
272	7.68	LM	M1.5		AN Sex
273	7.70	Star	K7		HD 157881
274	7.70	LM	M8		SIPS J1259-4336
275	7.71	LM	M5.5		LP 881-64
276	7.72	LM	M9.5		LP 881-64
277	7.73	LM	L0		LP 881-64
278	7.73	LM	M4e		G 192-13
279	7.73	LM	M0		HD 165222
280	7.73	LM	M5		G 109-35
281	7.73	LM	M5		G 227-22
282	7.75	BD	L7.5		WISEP J180026.60+013453.1
283	7.79	LM	M3e		GJ 623 A
284	7.80	LM?			GJ 623 B
285	7.84	LM	M2.5		CD-68 47
286	7.84	LM?			CD-68 47
287	7.88	BD	T9		WISE J000517.48+373720.5
288	7.88	BD	T8pec		2MASS J07290002-3954043
289	7.88	LM	M4e		G 154-44
290	7.91	LM	M4.5		SCR J0740-4257
291	7.97	LM	M4.5		GJ 831 A
292	7.98	LM?			GJ 831 B
293	7.98	Star	F6		pi.03 Ori
294	7.98	LM	M3		CD-44 3045 A
295	8.02	LM	M3		CD-44 3045 B
296	8.02	LM	M4.5		G 122-49
297	8.04	LM	M3		L 399-68
298	8.04	Star	F7		chi Dra A
299	8.05	Star	K0		chi Dra B
300	8.05	LM	M3.5e	1	Wolf 437
301	8.05	Planet			
302	8.07	BD	L7		2MASSW J2148162+400359
303	8.07	LM	M2.5		G 262-15
304	8.08	LM	M4.5e		G 13-22
305	8.08	LM	M3.5		L 674-15
306	8.08	WD	DA8P		EGGR 290

NB_OBJ	DISTANCE [pc]	OBJ_CAT	SP_TYPE	EXO_COUNT	SIMBAD_NAME
307	8.11	BD	T6.5		2MASS J00345157+0523050
308	8.11	LM	M2?		IRAS 21500+5903
309	8.12	WD	DAH		UCAC4 747-070768
310	8.15	LM	M1.5e	1	BD+18 3421
311	8.15	Planet			
312	8.16	WD	DA		LAWD 26
313	8.18	BD	T8.5		UGPS J052127.27+364048.6
314	8.18	Star	K2		GJ 66 A
315	8.19	Star	K2		GJ 66 B
316	8.21	LM	M2		L 173-19
317	8.23	Star	K7		HD 217357
318	8.23	LM	M3e		Ross 318
319	8.23	BD	T8		WISE J115013.85+630241.5
320	8.30	WD	DAP		LAWD 96
321	8.31	Star	G5		mu. Her A
322	8.31	LM	M4		mu. Her A
323	8.32	LM	M3.5		mu. Her B
324	8.33	LM?			mu. Her C
325	8.33	LM	M3.5e		GJ 747 A
326	8.34	LM?			GJ 747 B
327	8.34	WD	DA		Wolf 489
328	8.35	BD	T7		2MASS J03480772-6022270
329	8.35	LM	M4		G 227-29
330	8.36	LM	M4		G 130-4
331	8.36	LM	M8		SCR J1546-5534
332	8.37	BD	T6		SCR J1546-5534
333	8.39	LM	M0		HD 32450 A
334	8.39	LM?			HD 32450 B
335	8.41	LM	M5		SCR J1138-7721
336	8.41	Star	G0		bet CVn
337	8.46	LM	M4		Ross 64
338	8.47	LM	M3		CD-37 10765 A
339	8.49	LM	M5		CD-37 10765 B
340	8.49	WD	DA5.5		CD-32 5613
341	8.51	Star	G7	3	61 Vir
342	8.51	Planet			
343	8.53	Planet			
344	8.53	Planet			
345	8.53	WD	DZ13		EGGR 453
346	8.53	LM	M4.5e		Wolf 461
347	8.53	LM	M4.5		G 89-32 A
348	8.54	LM	M5		G 89-32 B
349	8.57	BD	>Y1?		
350	8.57	LM	M3		L 49-19
351	8.59	LM	M4.5e	1	CD Cet
352	8.59	Planet			
353	8.60	Star	F9.5		zet Tuc
354	8.60	LM	M5.5		NLTT 40406

NB_OBJ	DISTANCE [pc]	OBJ_CAT	SP_TYPE	EXO_COUNT	SIMBAD_NAME
355	8.60	BD	L9pec		2MASS J16471580+5632057
356	8.61	LM	M9		LP 666-9
357	8.62	LM	M4		G 19-7
358	8.65	LM	M5		AP Col
359	8.66	LM	M5		PM J11413-3624
360	8.68	Star	G0		chi01 Ori
361	8.69	LM?			chi01 Ori
362	8.69	LM	M4.5		LP 991-84
363	8.70	Star	F8.5		ksi UMa A
364	8.72	LM	M3		ksi UMa A
365	8.73	Star	G2		ksi UMa B
366	8.73	Star	K2-3		ksi UMa B
367	8.73	BD	T8.5		WISE J111838.70+312537.9
368	8.73	BD	L3.5		LSPM J0036+1821
369	8.73	Star	K3.5		HD 50281
370	8.73	LM	M2		HD 50281B
371	8.74	LM?			HD 50281B
372	8.74	LM	M1.5		MCC 135
373	8.74	BD	Y0?		
374	8.76	Star	G9		41 Ara A
375	8.77	LM?			41 Ara A
376	8.79	LM	M0		41 Ara B
377	8.79	LM	M4.5		GJ 791.2 A
378	8.81	LM?			GJ 791.2 B
379	8.81	Star	K2	2	HD 192310
380	8.81	Planet			
381	8.81	Planet			
382	8.81	LM	M3.5	2	BD-05 5715
383	8.81	Planet			
384	8.81	Planet			
385	8.81	LM	M2		GJ 745 A
386	8.82	LM	M2		GJ 745 B
387	8.82	LM	M3		L 32-8
388	8.83	LM	M2		L 32-9
389	8.83	Star	K3		HD 32147
390	8.83	LM	M3.5		G 111-47
391	8.84	LM	M2e		FK Aqr
392	8.85	LM	M3.5		FL Aqr
393	8.85	LM?			FK Aqr
394	8.85	BD?			FL Aqr
395	8.87	LM	M2		Ross 695
396	8.87	LM	M9		LEHPM 3396
397	8.88	LM?			SCR J0630-7643 A
398	8.88	LM?			SCR J0630-7643 B
399	8.88	BD	T8		2MASSI J0727182+171001
400	8.89	Star	F6.5		GJ 216 A
401	8.89	Star	K2.5		GJ 216 B
402	8.89	LM	M2		G 113-20
403	8.90	LM	M5e		G 193-27
404	8.93	LM?			G 193-27

NB_OBJ	DISTANCE [pc]	OBJ_CAT	SP_TYPE	EXO_COUNT	SIMBAD_NAME
405	9.02	LM	M1		SZ UMa
406	9.02	LM	M4.5		SZ UMa
407	9.07	LM	M2	3	CD-31 9113
408	9.07	Planet			
409	9.07	Planet			
410	9.07	Planet			
411	9.07	Star	K0		del Eri
412	9.07	LM	M2		HD 115953 A
413	9.08	LM?			HD 115953 A
414	9.09	LM?			HD 115953 B
415	9.09	LM	M5e		LP 469-206
416	9.09	WD	DQ9		EGGR 246
417	9.09	LM	M3.5e		V374 Peg
418	9.09	BD	L4.5		2MASS J06523073+4710348
419	9.10	LM	M5.5e		WT 460
420	9.11	LM	L1		WT 460
421	9.11	Star	G5		kap01 Cet
422	9.11	BD	T7.5		ULAS J141623.94+134836.3
423	9.11	BD	L6		2MASS J14162408+1348263
424	9.14	WD	DZA		LAWD 25
425	9.14	LM	M6.5e		GJ 283 B
426	9.15	BD	Y0		WISE J071322.55-291751.9
427	9.16	BD	L5.5		2MASS J03552337+1133437
428	9.16	BD	T9pec		WISEP J213456.73-713743.6
429	9.17	Star	K1		HD 103095
430	9.19	LM	M3.5		Ross 1015
431	9.19	Star	G0		bet Com
432	9.20	BD	L5.5		2MASS J17502484-0016151
433	9.20	BD?			2MASS J17502484-0016151
434	9.22	BD	T9pec		WISEP J232519.54-410534.9
435	9.23	LM	M3.5		L 737-9
436	9.23	LM?			L 737-9
437	9.23	LM	M3		LP 776-46
438	9.23	LM	M5.5		LP 469-67
439	9.25	Star	F9		gam Pav
440	9.27	LM	M4.5		G 112-50
441	9.27	Star	G2	1	HD 102365
442	9.28	Planet			
443	9.30	LM	M4		HD 102365B
444	9.31	BD	T9		WISE J121756.90+162640.8
445	9.31	BD	Y0		WISE J121756.90+162640.8

NB_OBJ	DISTANCE [pc]	OBJ_CAT	SP_TYPE	EXO_COUNT	SIMBAD_NAME
446	9.31	LM	M5.5		2MASS J00113182+5908400
447	9.31	LM	M3		BD-18 359
448	9.31	LM?			BD-18 359
449	9.31	BD	L5		2MASS J18212815+1414010
450	9.31	BD	L7		2MASSI J0340094-672405
451	9.34	LM	M3.5		Ross 837
452	9.35	BD	T8.5		WISEPA J045853.89+643452.9
453	9.35	BD	T9.5		WISEPA J045853.89+643452.9
454	9.37	LM	M2.5		CD-30 731
455	9.37	WD	DQ8		EGGR 41
456	9.38	BD	>Y1		
457	9.40	LM	M3.5e		GJ 748
458	9.40	LM?			GJ 748
459	9.40	LM	M1		CD-45 5378
460	9.40	LM	M2.5	3	L 678-39
461	9.41	Planet			
462	9.43	Planet			
463	9.43	Planet			
464	9.43	LM	M9e		1RXS J115928.5-524717
465	9.43	LM	M2		G 222-11
466	9.46	LM	M5.5		UCAC4 379-100760
467	9.46	LM	M2	1	HD 285968
468	9.47	Planet			
469	9.48	LM	M3e		CD-51 6859
470	9.48	LM	M5.5	2	G 234-45
471	9.49	Planet			
472	9.49	Planet			
473	9.49	LM?			BPS CS 22879-0089
474	9.49	LM?			BPS CS 22879-0089
475	9.50	LM	M4.5		L 35-12
476	9.50	LM	M5		G 192-15
477	9.52	LM	M4.5		G 144-25
478	9.52	LM	M2.5		BD+43 2796
479	9.53	LM	M4e		G 42-24
480	9.53	Star	K0		HD 100623
481	9.54	WD	DC		HD 100623B
482	9.55	LM	M5		Wolf 1069
483	9.55	Star	G8		61 UMa
484	9.57	LM	M5e		PM J20502-3424
485	9.57	LM	M3		CD-40 5404
486	9.60	BD	Y0		WISE J114156.71-332635.8
487	9.60	LM	M5		Wolf 227
488	9.61	BD?			Wolf 227
489	9.66	BD	L8		2MASS J14053729+8350248
490	9.66	LM	M5		G 161-7

NB_OBJ	DISTANCE [pc]	OBJ_CAT	SP_TYPE	EXO_COUNT	SIMBAD_NAME
491	9.66	LM	M5		G 161-7
492	9.67	LM	M3		CD-48 11837
493	9.67	LM?			CD-48 11837 B
494	9.67	BD	T9		CFBDS J005910-011401
495	9.68	LM	M3		L 768-119
496	9.68	BD?			L 768-119
497	9.69	LM	M4.5		AT Mic
498	9.69	LM	M4		AT Mic
499	9.71	LM	M0.5	1	AU Mic
500	9.71	Planet			
501	9.71	LM	M5		G 268-110
502	9.72	LM	M3.5e		G 48-20
503	9.72	WD	DA8.1		L 88-59
504	9.73	BD	T5.5		WISE J223617.59+510551.9
505	9.73	BD	T1.5		2MASS J20304235+0749358
506	9.73	LM	M5		G 119-36
507	9.74	LM?			G 119-36
508	9.74	BD	L8.5		2MASS J02572581-3105523
509	9.77	BD	T9		
510	9.77	LM	M6e		LP 655-48
511	9.77	LM	M2.5	1	Ross 905
512	9.80	Planet			
513	9.80	BD	L6		2MASSW J1515008+484742
514	9.84	Star	K5		HD 151288
515	9.85	BD	L8.5		CFBDS J213926+022023
516	9.85	BD	T3.5		CFBDS J213926+022023
517	9.85	LM	M1.5	1	BD+61 195
518	9.85	Planet			
519	9.86	LM	M5		BD+61 195 B
520	9.87	BD	T2.5		2MASS J07584037+3247245
521	9.89	LM	M2		GJ 22 A
522	9.89	LM	M3		GJ 22 B
523	9.89	LM	M4		GJ 22 C
524	9.89	Star	K1		12 Oph
525	9.89	LM?			UPM J0815-2344
526	9.90	LM?			UPM J0815-2344
527	9.90	LM	M5		G 203-42
528	9.91	LM	M0		HD 232979
529	9.92	LM	M3.5		G 160-28
530	9.92	LM	M5e		GJ 1230 A
531	9.93	LM	M4.5e		GJ 1230 B
532	9.93	LM?			GJ 1230 C
533	9.94	LM	M1		BD+16 2708 A
534	9.94	LM	M8.5		BD+16 2708 B
535	9.94	BD	M9		BD+16 2708 B

NB_OBJ	DISTANCE [pc]	OBJ_CAT	SP_TYPE	EXO_COUNT	SIMBAD_NAME
536	9.94	LM	M5e		L 403-31
537	9.94	LM	M6.5		LP 98-79
538	9.96	BD	>= Y2		WISE J182831.08+265037.7
539	9.96	LM	M3.5e		G 36-24
540	9.97	LM	M0e		HD 260655
1001	9.98	BD	L6.5?		CWISE J061741.79+194512.8
1002	9.99	BD	T8?		CWISE J061741.79+194512.8
1003	10.0	BD	T9		ULAS J133553.45+113005.2
1004	10.0	LM	M3		Ross 440
1005	10.0	LM	M4		Ross 440
1006	10.0	BD	Y0		WISE J033605.05-014350.4
1007	10.0	BD	T2pec		
1008	10.0	BD	Y1		WISE J064723.23-623235.5
1009	10.1	BD	T8.5		
1010	10.1	BD	>Y1		WISEU J050305.68-564834.0
1011	10.1	BD	T9		WISE J161441.46+173935.5
1012	10.2	BD	T9		
1013	10.2	LM	M7		G 100-28
1014	10.2	LM			G 100-28
1015	10.2	BD	T9.5		WISE J094305.98+360723.5
1016	10.4	BD	T7		2MASS J12373919+6526148
1017	10.4	BD	>Y1?		CWISEP J144606.62-231717.8
1018	11.0	BD	>Y1		WISEA J083011.95+283716.0
1019	11.6	BD	>Y1?		

Table A.1: In this Table are listed the nearest objects to the Sun. These data were obtained by Reylé, C. et al. 2021 from the third Early Data Release (EDR3) and represent the objects observed by Gaia over 10 pc distance from Sun.

Bibliography

Aumer, Michael, and James J. Binney. 2009. "Kinematics and history of the solar neighbourhood revisited." *Monthly Notices of the Royal Astronomical Society* 397, no. 3 (August): 1286–1301. https://doi.org/10.1111/j.1365-2966.2009.15053.x. arXiv: 0905.2512 [astro-ph.GA].

Babcock, Horace W. 1939. "The rotation of the Andromeda Nebula." *Lick Observatory Bulletin* 498 (January): 41–51. https://doi.org/10.5479/ADS/bib/1939LicOB.19.41B.

Bahcall, J. N. 1984. "K giants and the total amount of matter near the sun." *The Astrophysical Journal* 287 (December): 926–944. https://doi.org/10.1086/162750.

Bailer-Jones, C. A. L. 2018. "The completeness-corrected rate of stellar encounters with the Sun from the first Gaia data release." *Astronomy & Astrophysics* 609 (January): A8. https://doi.org/10.1051/0004-6361/201731453. arXiv: 1708.08595 [astro-ph.SR].

Bailer-Jones, C. A. L., J. Rybizki, R. Andrae, and M. Fouesneau. 2018. "New stellar encounters discovered in the second Gaia data release." *Astronomy & Astrophysics* 616 (August): A37. https://doi.org/10.1051/0004-6361/201833456. arXiv: 1805.07581 [astro-ph.SR].

Bate, Matthew R., Ian A. Bonnell, and Volker Bromm. 2003. "The formation of a star cluster: predicting the properties of stars and brown dwarfs." *Monthly Notices of the Royal Astronomical Society* 339, no. 3 (March): 577–599. https://doi.org/10.1046/j.1365-8711.2003.06210.x. arXiv: astro-ph/0212380 [astro-ph].

Binney, James, and Scott Tremaine. 2008. *Galactic Dynamics: Second Edition.*

Bobylev, V. V., and A. T. Bajkova. 2020. "Kinematic Properties of Young Intermediate- and Low-Mass Stars from the Gaia DR2 Catalogue." *Astronomy Reports* 64, no. 12 (December): 1042–1049. https://doi.org/10.1134/S1063772920120033. arXiv: 2011.00274 [astro-ph.GA].

————. 2018. "Kinematics of the Galaxy from OB Stars with Data from the Gaia DR2 Catalogue." *Astronomy Letters* 44, no. 11 (November): 676–687. https://doi.org/10.1134/S1063773718110026. arXiv: 1809.10512 [astro-ph.GA].

Bovy, Jo, and Hans-Walter Rix. 2013. "A Direct Dynamical Measurement of the Milky Way's Disk Surface Density Profile, Disk Scale Length, and Dark Matter Profile at 4 kpc $<\sim$R$<\sim$9 kpc." *The Astrophysical Journal* 779, no. 2 (December): 115. https://doi.org/10.1088/0004-637X/779/2/115. arXiv: 1309.0809 [astro-ph.GA].

Buzzoni, Alberto. 2005. "Broad-band colours and overall photometric properties of template galaxy models from stellar population synthesis." *Monthly Notices of the Royal Astronomical Society* 361, no. 2 (August): 725–742. https://doi.org/10.1111/j.1365-2966.2005.09204.x. arXiv: astro-ph/0506001 [astro-ph].

————. 2002. "Ultraviolet Properties of Primeval Galaxies: Theoretical Models from Stellar Population Synthesis." *The Astronomical Journal* 123, no. 3 (March): 1188–1199. https://doi.org/10.1086/338896. arXiv: astro-ph/0202419 [astro-ph].

Chabrier, Gilles. 2003. "Galactic Stellar and Substellar Initial Mass Function." *The Publications of the Astronomical Society of the Pacific* 115, no. 809 (July): 763–795. https://doi.org/10.1086/376392. arXiv: astro-ph/0304382 [astro-ph].

————. 2001. "The Galactic Disk Mass Budget. I. Stellar Mass Function and Density." *The Astrophysical Journal* 554, no. 2 (June): 1274–1281. https://doi.org/10.1086/321401. arXiv: astro-ph/0107018 [astro-ph].

————. 2002. "The Galactic Disk Mass Budget. II. Brown Dwarf Mass Function and Density." *The Astrophysical Journal* 567, no. 1 (March): 304–313. https://doi.org/10.1086/324716. arXiv: astro-ph/0110024 [astro-ph].

Chebotarev, G. A. 1965. "On the Dynamical Limites of the Solar System." *Soviet Astronomy* 8 (April): 787.

Chen, Bing, et al. 2001. "Stellar Population Studies with the SDSS. I. The Vertical Distribution of Stars in the Milky Way." *The Astrophysical Journal* 553, no. 1 (May): 184–197. https://doi.org/10.1086/320647.

Dehnen, Walter, and James J. Binney. 1998. "Local stellar kinematics from HIPPARCOS data." *Monthly Notices of the Royal Astronomical Society* 298, no. 2 (August): 387–394. https://doi.org/10.1046/j.1365-8711.1998.01600.x. arXiv: astro-ph/9710077 [astro-ph].

Ding, Ping-Jie, Zi Zhu, and Jia-Cheng Liu. 2019. "Local standard of rest based on Gaia DR2 catalog." *Research in Astronomy and Astrophysics* 19, no. 5 (May): 068. https://doi.org/10.1088/1674-4527/19/5/68.

Duncan, M. J., R. Brasser, L. Dones, and H. F. Levison. 2008. "The Role of the Galaxy in the Dynamical Evolution of Transneptunian Objects." In *The Solar System Beyond Neptune,* edited by M. A. Barucci, H. Boehnhardt, D. P. Cruikshank, A. Morbidelli, and Renee Dotson, 315.

Flynn, Chris, Johan Holmberg, Laura Portinari, Burkhard Fuchs, and Hartmut Jahreiß. 2006. "On the mass-to-light ratio of the local Galactic disc and the optical luminosity of the Galaxy." *Monthly Notices of the Royal Astronomical Society* 372, no. 3 (November): 1149–1160. https://doi.org/10.1111/j.1365-2966.2006.10911.x. arXiv: astro-ph/0608193 [astro-ph].

Fundamental Astronomy. 2007. January.

Gaia Collaboration et al. 2016. "The Gaia mission." *Astronomy & Astrophysics* 595 (November): A1. https://doi.org/10.1051/0004-6361/201629272. arXiv: 1609.04153 [astro-ph.IM].

Golubov, O., et al. 2013. "The asymmetric drift, the local standard of rest, and implications from RAVE data." *Astronomy & Astrophysics* 557 (September): A92. https://doi.org/10.1051/0004-6361/201321559. arXiv: 1307.6073 [astro-ph.GA].

Hou, L. G. 2021. "The Spiral Structure in the Solar Neighborhood." *Frontiers in Astronomy and Space Sciences* 8:103. ISSN: 2296-987X. https://doi.org/10.3389/fspas.2021.671670. https://www.frontiersin.org/article/10.3389/fspas.2021.671670.

Jurić, Mario, et al. 2008. "The Milky Way Tomography with SDSS. I. Stellar Number Density Distribution." *The Astrophysical Journal* 673, no. 2 (February): 864–914. https://doi.org/10.1086/523619. arXiv: astro-ph/0510520 [astro-ph].

Kaplan, M. H. 1976. *Modern spacecraft dynamics and control.*

Kubryk, M., N. Prantzos, and E. Athanassoula. 2015. "Evolution of the Milky Way with radial motions of stars and gas. I. The solar neighbourhood and the thin and thick disks." *Astronomy and Astrophysics* 580 (August): A126. https://doi.org/10.1051/0004-6361/201424171. arXiv: 1412.0585 [astro-ph.GA].

Lin, C. C., and Frank H. Shu. 1964. "On the Spiral Structure of Disk Galaxies." *Astrophysical Journal* 140 (August): 646. https://doi.org/10.1086/147955.

Lindblad, Bertil. 1925. "Star-streaming and the structure of the stellar system." *Arkiv for Matematik, Astronomi och Fysik* 21 (January): 1–8.

———. 1926. "Star-streaming and the structure of the stellar system (Second paper)." *Arkiv for Matematik, Astronomi och Fysik* 7 (February): 1–6.

Lucas, P. W., and P. F. Roche. 2000. "A population of very young brown dwarfs and free-floating planets in Orion." *Monthly Notices of the Royal Astronomical Society* 314, no. 4 (June): 858–864. https://doi.org/10.1046/j.1365-8711.2000.03515.x. arXiv: astro-ph/0003061 [astro-ph].

Luhman, Kevin L. 2012. "The Formation and Early Evolution of Low-Mass Stars and Brown Dwarfs." *Annual Review of Astronomy and Astrophysics* 50 (September): 65–106. https://doi.org/10.1146/annurev-astro-081811-125528. arXiv: 1208.5800 [astro-ph.GA].

McKee, Christopher F., Antonio Parravano, and David J. Hollenbach. 2015. "Stars, Gas, and Dark Matter in the Solar Neighborhood." *The Astrophysical Journal* 814, no. 1 (November): 13. https://doi.org/10.1088/0004-637X/814/1/13. arXiv: 1509.05334 [astro-ph.GA].

McMillan, Paul J. 2011. "Mass models of the Milky Way." *Monthly Notices of the Royal Astronomical Society* 414, no. 3 (July): 2446–2457. https://doi.org/10.1111/j.1365-2966.2011.18564.x. arXiv: 1102.4340 [astro-ph.GA].

McMillan, Paul J. 2016. "The mass distribution and gravitational potential of the Milky Way." *Monthly Notices of the Royal Astronomical Society* 465, no. 1 (October): 76–94. https://doi.org/10.1093/mnras/stw2759. eprint: https://academic.oup.com/mnras/article-pdf/465/1/76/8593676/stw2759.pdf. https://doi.org/10.1093/mnras/stw2759.

Miller, G. E., and J. M. Scalo. 1979. "The Initial Mass Function and Stellar Birthrate in the Solar Neighborhood." *Astrophysical Journal Supplement Series* 41 (November): 513. https://doi.org/10.1086/190629.

Oort, J. H. 1927a. "Observational evidence confirming Lindblad's hypothesis of a rotation of the galactic system." *Bulletin of the Astronomical Institutes of the Netherlands* 3 (April): 275.

———. 1927b. "Observational evidence confirming Lindblad's hypothesis of a rotation of the galactic system." *Bulletin of the Astronomical Institutes of the Netherlands* 3 (April): 275.

———. 1932. "The force exerted by the stellar system in the direction perpendicular to the galactic plane and some related problems." *Bulletin of the Astronomical Institutes of the Netherlands* 6 (August): 249.

———. 1950. "The structure of the cloud of comets surrounding the Solar System and a hypothesis concerning its origin." *Bulletin of the Astronomical Institutes of the Netherlands* 11 (January): 91–110.

Oort, J. H., F. J. Kerr, and G. Westerhout. 1958. "The galactic system as a spiral nebula (Council Note)." *Monthly Notices of the Royal Astronomical Society* 118 (January): 379. https://doi.org/10.1093/mnras/118.4.379.

Öpik, E. 1932. "Note on Stellar Perturbations of Nearly Parabolic Orbits." *Proceedings of the American Academy of Arts and Sciences* 67 (6): 169–183. ISSN: 01999818. http://www.jstor.org/stable/20022899.

Pardi, Maria Chiara, and Federico Ferrini. 1994. "Evolution of Spiral Galaxies. II. The Star Formation History in the Solar Neighborhood." *Astrophysical Journal* 421 (February): 491. https://doi.org/10.1086/173666.

Pease, Francis G. 1916. "The Rotation and Radial Velocity of the Spiral Nebula N. G. C. 4594." *Proceedings of the National Academy of Science* 2, no. 9 (September): 517–521. https://doi.org/10.1073/pnas.2.9.517.

Pecaut, Mark J., and Eric E. Mamajek. 2013. "Intrinsic Colors, Temperatures, and Bolometric Corrections of Pre-main-sequence Stars." *The Astrophysical Journal Supplement Series* 208, no. 1 (September): 9. https://doi.org/10.1088/0067-0049/208/1/9. arXiv: 1307.2657 [astro-ph.SR].

Reylé, C. et al. 2021. "The 10 parsec sample in the Gaia era." *A&A* 650:A201. https://doi.org/10.1051/0004-6361/202140985. https://doi.org/10.1051/0004-6361/202140985.

Robin, A. C., C. Reylé, S. Derrière, and S. Picaud. 2003. "A synthetic view on structure and evolution of the Milky Way." *Astronomy and Astrophysics* 409 (October): 523–540. https://doi.org/10.1051/0004-6361:20031117.

Rubin, V. C., Jr. Ford W. K., and N. Thonnard. 1980. "Rotational properties of 21 SC galaxies with a large range of luminosities and radii, from NGC 4605 (R=4kpc) to UGC 2885 (R=122kpc)." *Astrophysical Journal* 238 (June): 471–487. https://doi.org/10.1086/158003.

Salpeter, Edwin E. 1955. "The Luminosity Function and Stellar Evolution." *The Astrophysical Journal* 121 (January): 161. https://doi.org/10.1086/145971.

Sandage, Allan. 1987. "The Disk and Halo Densities at the Plane from Star Counts in the Galactic Poles." *Astronomical Journal* 93 (March): 610. https://doi.org/10.1086/114342.

Schechter, P. 1976. "An analytic expression for the luminosity function for galaxies." *Astrophysical Journal* 203 (January): 297–306. https://doi.org/10.1086/154079.

Schmidt, Maarten. 1959. "The Rate of Star Formation." *The Astrophysical Journal* 129 (March): 243. https://doi.org/10.1086/146614.

Schneider, Peter. 2015. *Extragalactic Astronomy and Cosmology: An Introduction.* https://doi.org/10.1007/978-3-642-54083-7.

Schönrich, Ralph, James Binney, and Walter Dehnen. 2010. "Local kinematics and the local standard of rest." *Monthly Notices of the Royal Astronomical Society* 403, no. 4 (April): 1829–1833. https://doi.org/10.1111/j.1365-2966.2010.16253.x. arXiv: 0912.3693 [astro-ph.GA].

Stone, E. C., et al. 2008. "The structure of the cloud of comets surrounding the Solar System and a hypothesis concerning its origin." *Nature* 454 (July): 71–74. https://doi.org/10.1038/nature07022.

van Maanen, A. 1916. "Preliminary evidence of internal motion in the spiral nebula Messier 101." *Astrophysical Journal* 44 (November): 210–228. https://doi.org/10.1086/142287.

Weaver, R., R. McCray, J. Castor, P. Shapiro, and R. Moore. 1977. "Interstellar bubbles. II. Structure and evolution." *Astrophysical Journal* 218 (December): 377–395. https://doi.org/10.1086/155692.

Xin, Xiao-Sheng, and Xing-Wu Zheng. 2013. "A revised rotation curve of the Milky Way with maser astrometry." *Research in Astronomy and Astrophysics* 13, no. 7 (July): 849-861. https://doi.org/10.1088/1674-4527/13/7/009.